



University
of Glasgow

Tandoi, Giuseppe (2011) *Monolithic high power mode locked GaAs/AlGaAs quantum well lasers*. PhD thesis

<http://theses.gla.ac.uk/2721/>

Copyright and moral rights for this thesis are retained by the author

A copy can be downloaded for personal non-commercial research or study, without prior permission or charge

This thesis cannot be reproduced or quoted extensively from without first obtaining permission in writing from the Author

The content must not be changed in any way or sold commercially in any format or medium without the formal permission of the Author

When referring to this work, full bibliographic details including the author, title, awarding institution and date of the thesis must be given.



Monolithic High Power Mode Locked GaAs/AlGaAs Quantum Well Lasers

by

Giuseppe Tandoi

A thesis submitted in partial fulfillment for the
degree of Doctor of Philosophy

in the
Faculty of Engineering
School of Engineering

June 2011

Declaration of Authorship

I, Giuseppe Tandoi, declare that this thesis titled, ‘Monolithic high power mode locked GaAs/AlGaAs quantum well lasers’ and the work presented in it are my own. I confirm that:

- This work was done wholly or mainly while in candidature for a research degree at this University.
- Where any part of this thesis has previously been submitted for a degree or any other qualification at this University or any other institution, this has been clearly stated.
- Where I have consulted the published work of others, this is always clearly attributed.
- Where I have quoted from the work of others, the source is always given. With the exception of such quotations, this thesis is entirely my own work.
- I have acknowledged all main sources of help.
- Where the thesis is based on work done by myself jointly with others, I have made clear exactly what was done by others and what I have contributed myself.

Signed: Giuseppe Tandoi

Date: 14 / June / 2011

“Considerate la vostra semenza, fatti non foste a viver come bruti, ma per seguir virtute e canoscenza.”

Dante Alighieri

UNIVERSITY OF GLASGOW

Abstract

Faculty of Engineering

School of Engineering

Doctor of Philosophy

by Giuseppe Tandoi

In this thesis, approaches for increasing the output power in monolithically integrated semiconductor mode locked (ML) lasers were investigated. The wavelength range considered is the range of operation of low temperature grown GaAs photomixers, devices commonly used for THz generation. In particular, two GaAs/AlGaAs quantum well laser epistuctures (operating at 830 nm and 795 nm) were considered, both with reduced optical confinement and elongated vertical optical mode size. In this work, such laser epistuctures, commonly used by high power semiconductor laser manufacturers, were successfully employed, for the first time, for producing passively ML devices. Improved average powers (up to 48 mW) under ML operation were demonstrated, around ten times higher than values previously reported in monolithic GaAs/AlGaAs ML lasers. In continuous wave operation, the output power was limited by the catastrophic damage of the laser facets at around 50 mW. For this reason, facet passivation techniques were investigated, allowing for powers up to 124 mW to be achieved. In ML regime, the output power was instead limited by the catastrophic damage of the reverse biased section of the laser. This failure mechanism was investigated and explained considering thermal effects on the reverse biased section. Such effects limited the output power to around 27 mW in 830 nm devices, which was then improved by 70% in 795 nm devices with a 70% larger optical mode area. The larger mode size, combined to a small duty-cycle laser geometry, enabled a record peak power of 9.8 W to be achieved at 6.83 GHz. This particular repetition rate was specifically designed for coherent population trapping experiments in ^{87}Rb vapors. Sub-picosecond transform limited pulses were achieved in both the laser materials considered, with a minimum duration of 0.43 ps at 126 GHz. With the values of peak power achieved, the developed devices may also be directly used for two-photon microscopy applications.

Publications

Peer reviewed publications directly related to this thesis work

1. **G. Tandoi**, K. Seunarine, C. N. Ironside, J. H. Marsh, A. C. Bryce, "Sub-picosecond 9.8W Peak Power Passively Mode Locked Quantum Well GaAs/AlGaAs Laser", paper submitted to the IEEE Photonics 2011 Conference (IPC11) - Photonics Society Annual Meeting, Arlington, Virginia USA, Oct. 2011.
2. **G. Tandoi**, K. Seunarine, C.N. Ironside, C.A. Bryce, S.D. McDougall, W. Meredith, A. N. Luiten, "Passively Mode-Locked Semiconductor Laser for Coherent Population Trapping in ^{87}Rb ", Conference on Lasers and Electro-Optics (CLEO) Europe, Munich, Germany, May 2011.
3. **G. Tandoi**, C. N. Ironside, A. C. Bryce, "Reconfigurable Repetition Rate in Colliding-Pulse Mode Locked Lasers with Non-Absorbing Mirrors", Conference on Lasers and Electro-Optics (CLEO) Europe, Munich, Germany, May 2011.
4. **G. Tandoi**, C. N. Ironside, A. C. Bryce, "Non-Absorbing Mirrors for Quantum Well Colliding Pulse Mode-Locked Lasers", IEEE Photonics Technology Letters, Aug. 2010.
5. **G. Tandoi**, S. McMaster, C. N. Ironside, A. C. Bryce, "Non-Absorbing Mirrors in Mode-Locked Lasers", Annual Photonics Society Meeting, Denver, Colorado USA, Nov. 2010.
6. **G. Tandoi**, C. N. Ironside, A. C. Bryce, S. D. McDougall, "GaAs/AlGaAs Colliding Pulse Mode-Locked Lasers with Non-Absorbing Mirrors", Conference on Lasers and Electro-Optics (CLEO), San Jose, California USA, May 2010.
7. **G. Tandoi**, C. N. Ironside, A. C. Bryce, S. D. McDougall, "High Power GaAs/AlGaAs Mode-Locked lasers", High Power Diode Lasers & Systems Meeting - Photonex09 - Stoneleigh Park, Coventry, UK, Oct. 2009.

8. **G. Tandoi**, C.N. Ironside and A.C. Bryce, "Multisection measurements of gain and loss for a MQW GaAs/AlGaAs High Power Laser material", Semiconductor and Integrated Optoelectronics (SIOE), Cardiff, UK, Apr. 2009.

Non-peer reviewed publications directly related to this thesis work

1. **G. Tandoi**, C. N. Ironside, A. C. Bryce, "High Power GaAs/AlGaAs Colliding Pulse Mode-Locked Lasers", IEEE Photonics Society Scottish Chapter meeting: Miniature Lasers and Nonlinear Optics, University of St Andrews, Scotland UK, Sep. 2010.
2. K. Seunarine, **G. Tandoi**, C. N. Ironside, A. C. Bryce, S. D. McDougall, W. Meredith, A. Luiten, "Non-cryogenic integrated optical magnetometers", MEG UK Meeting, University of Glasgow, Scotland UK, 29-30 Jan. 2011.
3. **G. Tandoi**, C.N. Ironside and A.C. Bryce, "Investigation of short wavelength GaAs/AlGaAs high power high frequency monolithically integrated Mode-Locked lasers", Engineering Postgraduate Conference Competition (1st prize award) - Glasgow - 23/24 June 2009.

Peer reviewed publications not directly related to this thesis work

1. K. Seunarine, B. Romeira, G., H. Cantu, M.J. Steer, **G. Tandoi**, C.N. Ironside, J.M.L. Figueiredo, D.J. Paul, A. Luiten. "Compact RF modulated laser diodes for atomic spectroscopy", submitted to the International Quantum Electronics Conference / Conference on Lasers and Electro-Optics (IQEC/CLEO), Pacific Rim, Sydney 28 Aug-1 Sep 2011.
2. T.J. Slight, **G. Tandoi**, D.G. Revin, A. McKee, S.Y. Zhang, W. Meredith, J.W. Cockburn, C.N. Ironside, " $\lambda \approx 3.35\mu\text{m}$ Distributed Feedback Quantum Cascade Lasers with High Aspect Ratio Lateral Grating", IEEE Photonics Technology Letters, Apr. 2011.
3. T.J. Slight, **G. Tandoi**, C.N. Ironside, A. McKee, C. Langton, I. Eddie, D.G. Revin, M.J. Steer, S.Y. Zhang, J.W. Cockburn, V.M.N. Passaro, F. De Leonardis; "Short Wavelength Distributed Feedback Quantum Cascade Laser", Conference on Lasers and Electro-Optics (CLEO), Baltimore, Maryland USA, Jun. 2009.

Books

1. V.M.N. Passaro, **G. Tandoi**, F. De Leonardis, M. Lagioia, R. Loiacono, F. Magno and R. Pagano, "Modeling of Photonic Devices", Novapublishers, 2009.

Acknowledgements

I would like to thank all those whose support, involvement, interest and advice made the completion of this work possible. In particular, I would like to express my gratitude to my supervisors Prof Charlie Ironside and Prof Catrina Bryce for their insightful guidance and advices and for encouraging me during my research work. I'm also particularly grateful to Prof Ironside for giving me the great opportunity of a Postdoc position in collaboration with the National Physical Laboratory.

I am very grateful to all the individuals who have helped me from the very start, especially Dr Antonio Samarelli and Dr Steven McMaster, who were precious sources of information, advice and support. In particular, they shared with me their knowledge on the fabrication of optoelectronic devices, from the basics to their tricks. I also thank Antonio for his fundamental help in taking professional SEM pictures of my devices and Steven for his contribution to the work on QWI and to the device characterization. However, besides their guidance in my work, I thank them for being very good friends and dinner-mates. In the fabrication, the advices of Dr Lianping Hou were also crucial, who always believed in me and was always supportive....thanks Lianping! My special thanks also go to Piotr Stolartz for his patience and availability in sorting all the problems with LABVIEW and to Dr Corrie Farmer for his advices on wet etching processes. Thanks to Dr Kris Seunarine for his contribution in the fabrication of the 793nm lasers. I also thank Dr Marc Sorel, Dr Julien Javaloyes and Dr Barry Holmes for the useful discussions and all the other colleagues and friends that supported my work or who were nice friends around, Giangiacomo, Carla, Philippe, Oberdan, Moss, Gabor, Chidi, Devna, Jehan, Michael, Bruno, Shahid, Usman, Marco, Vincenzo, Stefano, Piero and Masoud!...thanks guys!....if I forgot someone it's just because the Opto group is huge!!

No acknowledgement would be complete without noting the significant contribution from the technical support staff of the Department of Electronics and Electrical Engineering, who continuously endeavoured to keep the cleanrooms, beamwriter and dry-etching facilities operational and running smoothly. In particular, my special thanks go to Bill Ward, Douglas Lang, Marc Dragsnes, Ronnie Roger and Tom Reilly.

On a personal note, I would like to express my deep appreciation, from the bottom of my heart, to my parents and my sister, who supported me away from home and to Francesca for being always by my side. In simple words, I could not have done anything of this PhD experience without them. Grazie!

Contents

Declaration of Authorship	i
Abstract	iii
Publications	iv
Acknowledgements	vi
Abbreviations	x
1 Introduction	1
1.1 Optical pulses from semiconductor mode locked lasers	2
1.2 Repetition rate-related applications of semiconductor laser pulses	2
1.3 Mode locked lasers for THz generation in low temperature grown GaAs photomixers	3
1.4 Aims of the work	4
1.5 Other potential applications of high peak power ultra-short pulses from GaAs/AlGaAs lasers	5
1.6 Thesis outline	6
2 Background theory and design approaches	7
2.1 Semiconductor lasers	7
2.1.1 Threshold condition	10
2.1.2 Confinement of photons and carriers: progress towards present- day lasers	12
2.2 GaAs/AlGaAs material	12
2.2.1 Ridge waveguide design	15
2.2.2 Quantum confined energy levels	16
2.2.3 Many-body effects	18
2.3 High power operation issues in semiconductor lasers	20
2.4 Mode locking concept	21
2.4.1 Mode locking approaches	22
2.4.2 Conditions for ultrashort pulse generation	23
2.4.3 State of art performance of monolithic semiconductor passively mode locked lasers	26

2.4.4	Approaches for increasing the pulse repetition rate	28
2.5	Summary of design approaches	29
3	Fabrication of passively mode locked GaAs/AlGaAs lasers	31
3.1	Fabrication of ridge waveguide lasers with multiple contacts and non-absorbing mirrors	31
3.2	Patterning using electron beam lithography	33
3.3	Deposition of silica films	36
3.4	Reactive ion etching	37
3.5	Wet etching of GaAs/AlGaAs	40
3.6	Quantum well intermixing for non-absorbing mirrors	41
3.6.1	Quantum well intermixing techniques	42
3.6.2	Fabrication of non-absorbing mirrors	43
3.6.3	Optimization of the sputtering and rapid thermal annealing processes	44
3.6.4	Lateral grading of the quantum well intermixing process	48
3.6.5	Intermixing process reliability and repeatability	51
3.6.6	Issues and improvements of the SID layer lift-off	53
3.7	Definition of device contacts	55
3.8	Chapter summary	58
4	Material properties and approaches for the characterization of mode locked lasers	59
4.1	Oxide stripe lasers	59
4.2	Ridge waveguide lasers	61
4.3	Gain and absorption measurements	63
4.4	Ridge waveguide lasers with non-absorbing mirrors	69
4.5	Ridge waveguide lasers with protective coatings for facet passivation	71
4.6	Approaches for the characterization of mode locked lasers	73
4.6.1	Autocorrelation measurements	76
4.6.2	Autocorrelation set-up	80
4.6.3	Two photon absorption detectors	82
4.7	Chapter summary	87
5	Mode locked lasers results	89
5.1	Mode locked lasers with non-absorbing mirrors	89
5.1.1	Effect of non-absorbing mirrors on mode locking operation	92
5.1.2	Mode locking operation limiting factors	94
5.2	Sub-picosecond colliding pulse mode locking at 126 GHz	99
5.3	Improved mode locked output power in a higher d/Γ laser material	104
5.3.1	Semiconductor passive mode locked lasers for coherent population trapping in ^{87}Rb vapor cells	105
5.3.2	Design, fabrication and test of 795 nm passive mode locked lasers with pulse repetition rate of 6.8 GHz	108
5.4	Chapter summary	111
6	Summary and conclusions	113
6.1	Future work	116

A	Refractive index calculation for $\text{Al}_x\text{Ga}_{1-x}\text{As}$ compounds	118
B	Confined states in GaAs/$\text{Al}_x\text{Ga}_{1-x}\text{As}$ quantum wells	119
C	Summary of fabrication steps	123
	Bibliography	126

Abbreviations

ACPM	A symmetric C olliding P ulse M ode-locking
BSS	B eam S tep S ize
CCM	C ompound C avity M ode-locking
COMD	C atastrophic O ptical M irror D amage
CPM	C olliding P ulse M ode-locking
CPT	C oherent P opulation T rapping
CW	C ontinuous W ave
DBR	D istributed B ragg R eflector
DC	D irect C urrent
DH	D ouble H eterostructure
DWDM	D ense W avelength D omain M ultiplexing
EBL	E lectron B eam L ithography
EDFA	E rbium D oped F iber A mplifiers
EPSRC	E ngineering P hysical S ciences C ouncil
FP	F abry P erot
FRL	F ar- F ield R eduction L ayer
FWHM	F ull W idth H alf M aximum
GRIN-SCH	G Raded I Ndex S eparate C onfinement H eterostructure
HF	H ydro F luoric
HML	H armonic M ode L ocking
HSQ	H ydrogen S ilses Q uinoxane
IFVD	I mpurity F ree V acancy D isordering
IID	I mpurity I nduced D isordering
IPA	I so P ropyl A lcohol
JWNC	J ames W att N anofabrication C enter
LI	L ight C urrent
LID	L ight I nduced D isordering
LTG	L ow T emperature G rown
MCPM	M ultiple C olliding P ulse M ode-locking
MW	M icro W ave

MFC	Mass Flow Controller
MFS	Minimum Feature Size
MIBK	Methyl Iso Butyl Ketone
ML	Mode Locked
MLLD	Mode Locked Laser Diode
MOCVD	Metal Organic Chemical Vapour Deposition
NAM	Non Absorbing Mirror
OSA	Optical Spectrum Analyzer
OSL	Oxide Stripe Lasers
OTDM	Optical Time Division Multiplexing
PAID	Photo Absorption Induced Disordering
PECVD	Plasma Enhanced Chemical Vapour Deposition
PL	Photo Luminescence
PMMA	Poly Methyl Metha Acrylate
PVD	Physical Enhanced Chemical Vapour Deposition
QCSE	Quantum Confinement Stark Effect
QD	Quantum Dots
QW	Quantum Well
QWI	Quantum Well Intermixing
RF	Radio Frequency
RIE	Reactive Ion Etching
RTA	Rapid Thermal Annealing
RWL	Ridge Waveguide Lasers
SA	Saturable Absorber
SCH	Separate Confinement Heterostructure
SESAM	SEmiconductor Saturable Absorber Mirror
SHC	Second Harmonic Cristal
SID	Sputtering Induced Disordering
SPM	Self Phase Modulation
SS	Spot Size
TBP	Time Bandwidth Product
TE	Transverse Electric
TEC	Thermo Electric Cooler
TLM	Transfer Length Method
TM	Transverse Magnetic
TPA	Two Photon Absorption
VI	Voltage Current
VRU	Variable Resolution Unit
WDM	Wavelength Domain Multiplexing

To Francesca and my Family

Chapter 1

Introduction

This PhD work is part of the Engineering and Physical Sciences Research Council (EPSRC) project named 'High power, high frequency mode locked semiconductor lasers' [1]. The aim of the EPSRC project was the production of semiconductor mode locked (ML) lasers emitting ultrashort pulses at high repetition rates (from few tens of GHz up to the sub-THz/THz range) and with high average output powers (ranging from several tens to few hundreds of mW).

In the EPSRC project, the emission wavelengths under investigation were 1550 nm (in InGaAsP/InP and AlGaAsP/InP quantum well material systems) and in the range of 700–850 nm (in AlGaAs/GaAs and InGaAsP/GaAs quantum well material systems). The first wavelength range is of particular importance for future high-speed optical time division multiplexed (OTDM) communication systems in optical fibers, with repetition rates of 40 GHz and 160 GHz [2]. As will be better explained in this chapter, among other direct uses of microwave-modulated optical signals in the 700-850 nm range, THz generation can be achieved with laser sources operating at very high pulse repetition rates, with several industrial, medical, military and security applications of great importance [3–8].

Within the broader contest of the EPSRC project, the purpose addressed by this thesis is the production of mode locked laser diodes (MLLD) operating in the 700–850 nm wavelength range and the investigation of approaches for improving both their output power and repetition rate. This chapter will thus explain the need for a high power and high frequency semiconductor ML laser and will generally introduce and justify the approaches chosen for our purposes.

1.1 Optical pulses from semiconductor mode locked lasers

The general aim of the work reported in this thesis is the development of compact monolithic semiconductor sources of optical pulses. Optical pulses can be generated in semiconductor lasers in a number of ways, for example by modulating the intracavity losses (Q-switching) or by switching the carrier concentration (gain switching) of the laser [2]. However, the shortest pulses and highest repetition rates are achieved in the mode locking approach [2]. This approach will be described in detail in the next chapter, while here only the main characteristics of the output of a ML laser are considered. The output of a ML laser consists in a comb of equidistant phase-locked spectral modes, whose superposition corresponds to a train of pulses in the optical domain, as illustrated in Figure 1.1.

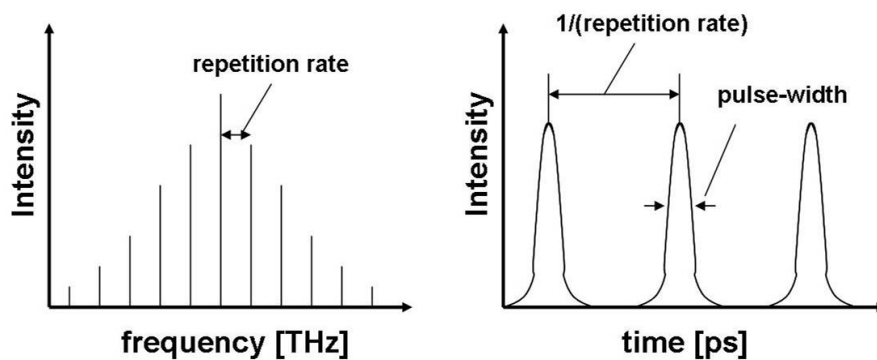


FIGURE 1.1: Typical optical spectrum (left) and corresponding time-domain intensity modulation (right) of the output of a ML laser.

As shown in Figure 1.1, among the several distinctive characteristics of such ML optical signals, the main ones are central wavelength, pulse repetition rate, optical power and pulse-width [9]. These signal features are used here to broadly classify the applications of semiconductor laser pulses.

1.2 Repetition rate-related applications of semiconductor laser pulses

Semiconductor laser pulses at high repetition rates (1-100 GHz) may be used directly in the optical domain in telecommunications applications. Although the spectral efficiency of ML lasers limits their use as sources of pulses in optical fibre telecommunications, these can be used for clock generation and recovery for OTDM in digital fibre telecommunications [10–13], as multichannel sources in wavelength domain multiplexing (WDM) and dense wavelength domain multiplexing (DWDM) systems [14, 15] and for

all-optical timing jitter reduction and frequency synchronization [16–23]. Other uses include local oscillator sources for heterodyne [24] and superheterodyne receivers, used on satellites and radiotelescopes for atmospheric sensing and spectroscopy, fibre-radio networks sources [25–28] and frequency rulers for spectroscopy [29]. Although in most of the aforementioned applications, particularly the ones based on optical fibers, semiconductor lasers operating at 1550 nm are preferred, GaAs/AlGaAs lasers operating in the 700–850 nm range may also be used.

1.3 Mode locked lasers for THz generation in low temperature grown GaAs photomixers

Higher repetition rates (sub-THz/THz range) are instead of interest for the generation of THz signals, with many important applications such as imaging, communications and spectroscopy [3–8]. Several different approaches have been proposed for generating THz waves, based on both electronic and optoelectronic technologies [3–8]. The highest powers are usually achieved with optical methods, based on the down-conversion of sub-THz/THz-modulated optical signals or on the extraction of the difference-frequency between two or more phase-locked monochromatic continuous-wave (CW) optical signals [30]. For both approaches, several methods have been proposed for the extraction of the microwave (MW) or THz component, including, for example, direct detection or photomixing [30]. A common implementation of such optical methods is based on the photomixing in a low temperature grown (LTG) GaAs sample patterned with interdigitated contacts [31, 32], as illustrated in Figure 1.2. The two phase-matched THz-offset optical beams required in the photomixing scheme need to have photon energies higher than the LTG GaAs bandgap energy (1.424 eV - 870 nm), i.e. need to operate in the 700–850 nm range [31, 32].

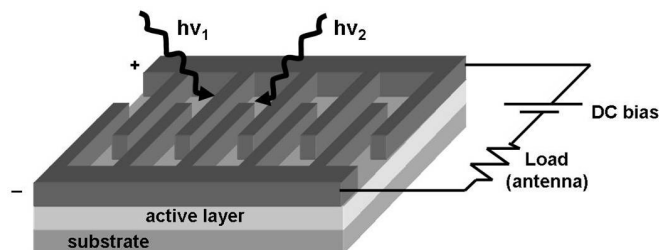


FIGURE 1.2: Schematic of photomixer design and operation [30].

Classical photomixing approaches make use of pairs of continuous wave (CW) GaAs/AlGaAs distributed Bragg reflector (DBR) diode lasers or Ti:Sapphire lasers (or two modes of a single laser), with a required average optical power in the 10–100 mW range [33–38].

A simpler implementation is based on the use of ML lasers, whose output takes the form of a comb of narrow-linewidth equidistant modes, as illustrated in Figure 1.1. In this case the optimal number of locked modes would be three (three is also the minimum number of modes required for mode locking), for maximum efficiency. One proposed approach makes use of ML lasers emitting at THz pulse repetition rates [30]. Alternatively, short laser pulses (100 fs and below) can be used. High peak powers (of around 1 kW) are needed in order to have sufficient power in the THz components [39]. In this case, the emission of THz radiation in the biased LT-GaAs antenna is excited by inducing a rapid change of the carrier density via femtosecond laser pumping [39]. Here, passively ML Ti:Sapphire lasers are the preferred sources as they cover the 700-850 nm range with peak powers of 1-10 kW (10-100 fs wide pulses at 80 MHz repetition rates and with 0.1-1 W average powers) [40].

Passively ML lasers in the GaAs/AlGaAs system also cover the 700-850 nm range, with repetition rates from few GHz to several hundreds of GHz [41–44]. However, the average ML output power in GaAs/AlGaAs MLLDs is typically well below 10 mW and the emitted pulses are not shorter than 2 ps [41–44], severely limiting their use in such applications (while in other material systems and wavelengths better performance are achieved - see Section 2.4.3). Therefore, this research is aimed to understand and possibly overcome such output power limitations.

1.4 Aims of the work

The aim of this work is the development of ML lasers in the GaAs/AlGaAs material system as compact and cheap sources of high peak power optical pulses for THz generation in LTG GaAs photomixers. In particular, the following objectives have been pursued:

- evaluation of the output power limits in GaAs/AlGaAs ML lasers;
- investigation of the mechanisms responsible for such power limitations;
- investigation of novel approaches for increasing their average and peak output power;

In Chapter 2, the approaches considered for our purposes will be described in detail, while here, only a general introduction to them is given. The overall idea behind this study is the combination of the ML operation of laser diodes with methods typically used for improving the output power in semiconductor lasers. To this end, two wafer structures designed by Intense Ltd for high power applications were considered, operating

at 830 and 793 nm. As will be explained in the next chapter, the main characteristics of such structures are the enlarged vertical mode profile and consequent reduced optical confinement, which allow for improved single mode operation, increase in cavity length and reduction in vertical far-field. Under CW operation, the output power of the 830 nm laser material considered was limited by the catastrophic optical damage of the facets. For this reason, two techniques of facet passivation were investigated: non-absorbing mirrors and protective coatings. However, under ML operation, the output power was limited by the catastrophic damage of the reverse biased section of the device and such mechanism was also investigated. Improved performance were achieved with a 793 nm wafer structure with increased vertical mode size and reduced optical confinement, compared to the 830 nm one. With this structure, a record peak power of 9.8 W was successfully demonstrated, with 0.71 ps wide pulses, in a 5.6 mm long device. This peak power is, to the best of our knowledge, higher than any other value previously reported for monolithic passively mode locked semiconductor lasers - see Section 2.4.3 for a review of state-of-art performance of MLLDs. This device was specifically designed to operate at a repetition rate of 6.83 GHz and 795 nm. As will be explained in Chapter 5, these specific operating wavelength and repetition rate are of interest for a particular application that was considered in this work, coherent population trapping in ^{87}Rb vapor cells. Shorter cavity lengths (0.6 mm), combined with repetition rate multiplication techniques, were also employed for achieving higher repetition rates (126 GHz), of interest for the generation of microwave and millimetrewave signals, as sources of pulses in high speed short-haul communications and in radio-over-fibre high-speed data communication systems [42, 45].

1.5 Other potential applications of high peak power ultra-short pulses from GaAs/AlGaAs lasers

Laser pulses with high peak power (of the order of 1-10 kW) are also widely used for exploiting non-linear optical effects in non-linear media [9]. In these applications, the optical pulses are focused into small spots (from few μm to few tens of μm) using objective lenses, in order to produce very high intensities (of the order of 1 GW/cm²) [9]. Such high intensities are required for producing second order non-linear effects [9]. These are usually described by the product of non-linear susceptibility $\chi^{(2)}$ of the medium being excited and the intensity of the optical beam used to excite it [9]. As the $\chi^{(2)}$ is typically low (1-100x10⁻⁹ esu [46]), high intensities are required. Although the maximum peak powers achieved in this work did not exceed 9.8 W, it is worth mentioning other potential applications of high peak power laser beams that may be accessed with

optimized device designs and external amplification of sub-picosecond semiconductor laser pulses.

One common application of non-linearities of the second-order is the second harmonic generation (SHG) or frequency doubling, where a strong electric field is used to excite the emission of photons at twice the frequency of the input field [40, 47]. Typical non-linear crystals employed with femtosecond Ti:Sapphire lasers include β -barium borate (BBO = β -BaB₂O₄), potassium titanyl phosphate (KTP = KTiOPO₄) and lithium triborate (LBO = LiB₃O₅) [48]. Ti:Sapphire lasers are widely tunable between 700 and 1000 nm (even more) and, therefore, ultraviolet and blue light can be easily accessed with this technique [47]. Optical pulses of few ps generated using semiconductor lasers and amplified using external amplifiers have been used for SHG [49]. A further application of high intensity optical beams is two-photon fluorescence microscopy or bio-imaging, where a biological sample is scanned with high intensity photons at a given frequency ω_0 . At the photon frequency, the linear absorption is poor, but there is enough non-linear absorption to absorb pairs of photons, whose sum-energy is then re-emitted at twice the photon frequency ω_0 . As the two-photon response is dependent on the sample composition, this technique gives a spatial insight into it. In this application, semiconductor ML lasers [50] (a series of a ML laser with two semiconductor optical amplifiers, with a peak power requirement of 20 W) have been used as an alternative to femtosecond Ti:Sapphire lasers [51].

1.6 Thesis outline

In this chapter, the aims of this research work have been explained, with a brief overview of the main potential applications of high peak power ML GaAs/AlGaAs lasers and of devices with high repetition rates (of the order of 100 GHz). The rest of the thesis will be concerned with the concept, development and measurement of the ML semiconductor lasers described above. In next chapter, some pertinent theory of diode lasers and a review of the main design approaches for achieving high power operation and high frequency operation will be presented, followed by a review of their state-of-art. Chapter 3 will give a detailed description of the fabrication steps needed for producing the lasers considered in this project, with more attention to the processes that needed particular development or optimization work. Chapter 4 will present results from some preliminary devices and measurements, made to assess the laser material properties and optimize the final device design. Chapter 4 will also describe the measurement techniques developed for the characterization of the fabricated ML devices. In Chapter 5, the main results of this thesis will be presented, while conclusions will finally be given in Chapter 6.

Chapter 2

Background theory and design approaches

In this chapter, a brief introduction of some basic background theory and design considerations relevant to semiconductor lasers is given, with an overview of the main progress made from their first demonstration to present day devices. This introduction then focuses on the peculiarities of the GaAs/AlGaAs material chosen for this work with the intent of increasing the device output power. Some critical issues related to the high power operation of semiconductor lasers are also discussed here. Mode locking is introduced as a narrow pulse generation method, with some simple theory and techniques applicable to the semiconductor lasers being presented. Moreover, in the last sections, the state-of-art performance reported in literature in terms of shortest pulse-width, highest average and peak power and highest repetition rate are reviewed. Ultimately, the last section gives a summary of the design approaches chosen in this work.

2.1 Semiconductor lasers

This section is intended to give a brief introduction into the field of semiconductor lasers and is based on the concise tutorials by Weisbuch [52] and [53]. A knowledge of the basics of solid-state and semiconductor physics is assumed, while the reader wishing to find a more comprehensive treatment of the subject is referred to the excellent textbooks [54–57].

Semiconductor lasers can cover a wide range of the spectrum extending from the near ultraviolet to the far infrared ($0.3\text{--}10\mu\text{m}$), thanks to the careful engineering of the bandgap energy of compound semiconductor materials. These are typically alloys of

elements of various groups of the Periodic Table grown as crystals, with closely matched lattice constants between adjacent layers of different compositions. The graph of Figure 2.1 shows material compositions against their bandgap energy, with horizontal lines connecting the materials with matching lattice constants. Of these, three material systems are particularly versatile: GaAs/AlGaAs covering the spectrum between 0.7–0.9 μm , and InGaAsP/InGaAs/InP or InGaAs/InAlGaAs/InP with wavelengths from 0.9–1.67 μm (1.1 μm being the shortest practical wavelength for a laser). The latter two are of particular importance in telecommunications applications [2].

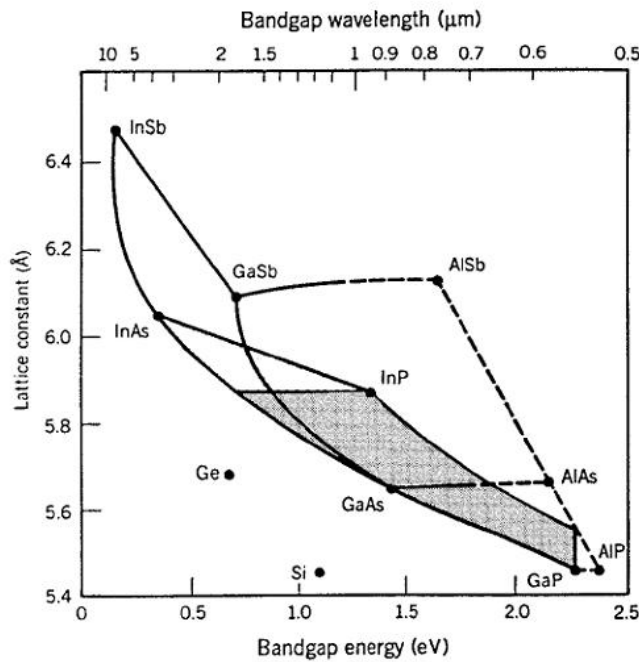


FIGURE 2.1: Lattice constant versus band-gap energy for various III-V semiconductors [55].

The material used in the project is GaAs/AlGaAs, grown using the MOCVD technique, due to it being one of the most mature and well-researched semiconductor systems and also, as explained in the previous chapter, because it operates in the wavelength range of operation of LTG GaAs photomixers. The lattice constants of GaAs and AlGaAs are almost identical, enabling growth of heterostructures with a low concentration of defects and low stress at the interfaces [58]. As the bandgap of $\text{Al}_x\text{Ga}_{1-x}\text{As}$ material increases with increasing Al fraction x , potential barriers are formed at the GaAs/AlGaAs heterostructure interface, whose magnitudes have been determined experimentally as $\Delta E_c = 0.67 \Delta E_g$ and $\Delta E_v = 0.33 \Delta E_g$ for the conduction and valence bands, respectively, where ΔE_g is the bandgap energy [58]. As shown in Figure 2.2, in a GaAs/AlGaAs double heterostructure (DH), the GaAs active layer is sandwiched between two AlGaAs claddings. These provide vertical confinement both for the electrons injected in the

active region and for the photons generated in it, because of the lower refractive index associated to the higher bandgap [55].

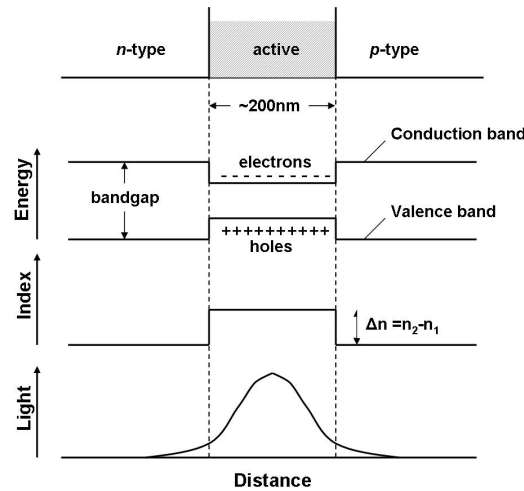


FIGURE 2.2: Confinement of electrons and photons in a double heterostructure [55].

The top and bottom claddings are p -doped and n -doped, respectively, to form a p - n junction, while the active layer is left undoped, in order to enhance the radiative recombination of the injected electron-hole pairs. Figure 2.3 schematically depicts the formation of gain in a semiconductor structure.

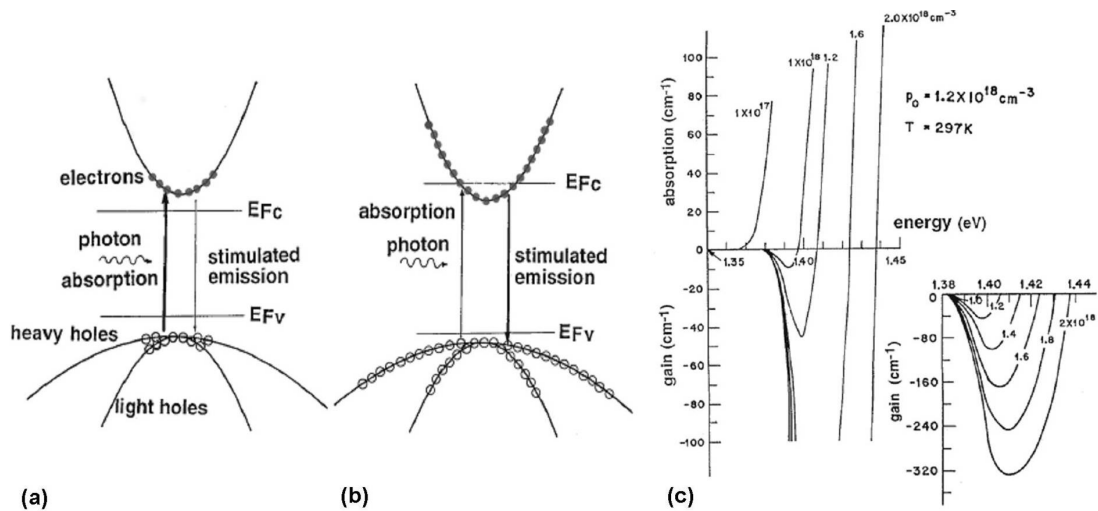


FIGURE 2.3: Schematics of gain formation in a semiconductor: absorption and stimulated emission transitions under weak (a) and strong (b) injection. Note the position of the quasi Fermi levels E_{F_c} and E_{F_v} . (c) Absorption and gain under increasing excitation [57].

Under electrical injection of electrons and holes into the active region from the adjacent n and p -regions, one creates an inversion of excess carrier population near the band edge.

If the injected carrier concentration becomes large enough, the stimulated emission can exceed the absorption and optical gain is created [53, 57, 58]. The standard calculation involves summation, for a particular photon energy, over the various transitions that can occur between all electron-hole pairs, whether inverted or not. The former give gain, and the latter absorption. For a detailed treatment of models describing the optical gain in semiconductor lasers, the reader is referred to [53, 57, 58].

2.1.1 Threshold condition

A schematic of a most basic Fabry-Perot (FP) semiconductor laser with a cavity length L is given in Figure 2.4(a) [52].

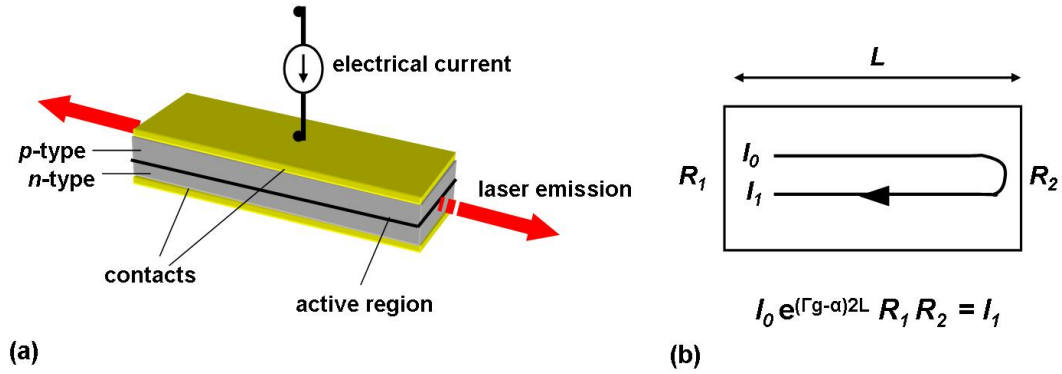


FIGURE 2.4: (a) Schematics of a semiconductor laser; (b) Balance equation for an optical wave completing a round trip in the cavity.

Emission of light takes place between two mirrors formed by cleaved semiconductor-air interfaces. An optical wave propagating within the laser cavity has to satisfy the phase condition

$$\frac{2\pi n_g}{\lambda} 2L = 2m\pi, \quad (2.1)$$

where $n_g = n - dn/d\lambda$ is the group refractive index and m a positive integer. This gives a condition on the wavelength of the longitudinal modes (eigenmodes) allowed to propagate in the cavity:

$$\lambda_m = \frac{2n_g L}{m}. \quad (2.2)$$

For an eigenmode λ_m , the threshold condition is obtained by stating that the intensity is unchanged after a round trip of the cavity, as illustrated in Figure 2.4(b). This can be expressed as

$$R_1 R_2 e^{(\Gamma g - \alpha_i) 2L} = 1, \quad (2.3)$$

where R_1 and R_2 are the reflection coefficients of the mirrors (typically 0.32 for cleaved facets), Γ is the transverse optical confinement of the electric field in the active region,

g is the material gain coefficient per unit length and α_i is the intrinsic (or internal) loss coefficient per unit length. The gain at threshold can thus be expressed as

$$\Gamma g = \alpha_i + \alpha_{MIRR} = \alpha_i + \frac{1}{L} \ln\left(\frac{1}{R}\right), \quad (2.4)$$

where $R = \sqrt{R_1 R_2}$ is the mean mirror intensity reflection coefficient and α_{MIRR} the mirror loss coefficient.

In order to find some practical formula for threshold current I_{th} and optical output power P_{out} in semiconductor lasers, we need to consider the following rate equations, respectively, for the carrier density N and for the photon density N_p [53, 58]:

$$\frac{dN}{dt} = \eta_i \frac{I}{qV} - (R_{sp} + R_{nr} + R_l) - v_g g N_p \quad (2.5)$$

and

$$\frac{dN_p}{dt} = \Gamma v_g g N_p + \Gamma \beta_{sp} R_{sp} - \frac{N_p}{\tau_p}. \quad (2.6)$$

In Equation 2.5, η_i is the material internal efficiency (also called injection efficiency and indicated as η_{inj}), I the injected current, q the electron charge, V the active volume and $R_{sp} + R_{nr} + R_l$ are, respectively, the spontaneous electron recombination, non-radiative recombination and leakage rates. In Equation 2.6, $v_g = c/n_g$ is the group velocity, β_{sp} the spontaneous emission factor and τ_p the photon lifetime in the cavity (defined as $\tau_p^{-1} = v_g[\alpha_i + \alpha_{MIRR}]$). Above threshold (for $I > I_{th}$), we need to impose the steady state condition for both carrier and photon density rate equations, considering also that both carrier density and gain coefficient clamp at their threshold values, N_{th} and g_{th} , respectively [53, 58]. We thus obtain the steady state photon density as

$$N_p = \eta_i \frac{I - I_{th}}{q v_g g_{th} V}, \quad (2.7)$$

with the threshold current defined as

$$I_{th} = \frac{qV}{\eta_i} \frac{N_{th}}{\tau} = \frac{qV}{\eta_i} (R_{sp} + R_{nr} + R_l)_{th}, \quad (2.8)$$

with τ being the carrier lifetime. The total emitted output power can thus be calculated as

$$P_{out} = v_g \alpha_{MIRR} N_p h \nu V_p, \quad (2.9)$$

where V_p is the cavity volume (given by the product of the optical mode area and the cavity length). Defining $\Gamma = V/V_p$ and the differential quantum efficiency as

$$\eta_d = \frac{\eta_i \alpha_{MIRR}}{\alpha_i + \alpha_{MIRR}}, \quad (2.10)$$

we obtain, for $I > I_{th}$,

$$P_{out} = \eta_d \frac{h\nu}{q} (I - I_{th}). \quad (2.11)$$

2.1.2 Confinement of photons and carriers: progress towards present-day lasers

In real laser diodes, only a fraction of the main optical mode overlaps the active region that provides gain and induces stimulated emission. However, the whole of the wave experiences absorption and loss [53, 58]. This is taken into account by the optical confinement factor Γ introduced in Equation 2.4. The waveguiding effect in a DH, whose Γ is relatively large (>0.1), is due to the higher refractive index in the active region, typically $0.1 \mu\text{m}$ thick [53, 58]. Below this value, the active layer is too thin to have a strong waveguiding effect. This is the case of quantum well lasers (QW), whose active layer thickness is only few nm [53, 58]. For this reason, in QW lasers a separate confinement heterostructure (SCH) has to be used to overcome the poor optical confinement. This confines photons in a wider optical cavity surrounding the active QW layer [53, 58]. In the QWs, due to the occurrence of quantum effects, the energy dependence of the density of states, i.e. the number of quantum states per unit energy per unit volume, is step-like in behavior [53, 58]. This reduces the threshold current density (few electrons required for optical transparency) and improves the differential gain (allowing for high speed operation and a narrow output linewidth) [59]. However, the price paid is the saturation of gain, due to the fully inversion of the electron and hole states of a given discrete energy level [53]. Nevertheless, the issue of gain saturation may be overcome by the use of multiple quantum wells (MQW). Obviously this leads to larger transparency current densities, but also allows for improved differential gain and higher gain saturation [2].

Finally, three-dimensional carrier confinement is achieved in quantum-dot (QD) lasers. QD lasers offer a number of advantages, such as wider gain bandwidth, weaker temperature dependence of threshold current and reduced sensitivity to external feedback [58], but the material growth is still less mature compared to QWs.

2.2 GaAs/AlGaAs material

As already mentioned, the semiconductor alloy chosen in this work is a GaAs/AlGaAs epistructure grown by MOCVD. The design was made by Intense Ltd and grown by IQE Ltd for high power applications, such as laser printers [60] or for pumping Er^{3+} -doped

fiber amplifiers (EDFA) [61] or Nd:YAG solid state lasers. The epilayer structure is reported in Table 2.1 and is similar to the ones discussed in [62, 63].

$\text{Al}_x\text{Ga}_{1-x}\text{As}$ layer	mole fraction x (ini.val.-end val.)	thickness [μm]	Doping type and concentration [10^{17}cm^{-3}]	Dopant
cap layer	0	0.1	P ($1*10^2 - 1*10^5$)	Zinc
matching layer	0.32-0.05	0.12	P ($1*10^1 - 5*10^1$)	Zinc
p-cladding	0.32	1.7	P ($1*10^1$)	Zinc
p-cladding	0.32	0.2	P ($5 - 1*10^1$)	Zinc
graded index	0.2-0.32	0.12	UD	none
quantum well	0	0.0044	UD	none
barrier	0.2	0.009	UD	none
quantum well	0	0.0044	UD	none
graded index	0.27-0.2	0.07	UD	none
n-cladding	0.3-0.27	0.03	N (1)	Silicon
n-cladding	0.32-0.3	0.02	N (5 - 1)	Silicon
n-cladding	0.32	0.75	N (5)	Silicon
F.F.R. graded layer	0.29-0.32	0.35	N (5)	Silicon
F.F.R. graded layer	0.32-0.29	0.35	N (5)	Silicon
n-cladding	0.32	1.6	N (7)	Silicon
matching layer	0.05-0.32	0.2	N ($2*10^1 - 7$)	Silicon
substrate	0	645	N ($2*10^1$)	Silicon

TABLE 2.1: Epilayer structure of the 830 nm high d/Γ material designed by Intense.

As can be seen from Table 2.1, the two QWs designed to emit at 830 nm are inserted in a wider SCH waveguiding layer. Moreover, the waveguide core also has a graded Al mole fraction which produces a graded refractive index profile. This waveguide structure, called graded index separate confinement heterostructure (GRIN-SCH), allows for an improved carrier injection efficiency into the active layer (thus lower threshold and higher differential gain) and higher characteristic temperatures, thanks to a more efficient thermalization of carriers into the quantum wells and a better optical overlap with the electrically active wells [58].

The peculiarity of this laser material is the far-field reduction layer (FRL) inserted in the n -cladding. The FRL represents a passive waveguide, due to its higher refractive index compared to the one in the cladding. It thus acts as an optical trap for the optical mode, that is slightly attracted towards the substrate. This enlarges the mode size in the vertical direction, reducing the vertical far field divergence to about 17° [62]. The low beam divergence produced, together with a more symmetric beam profile, improves the coupling efficiency with single mode fibers or other coupling optics. The bandgap energy (calculated as $E_g = 1.424 + 1.247x_{Al}$) and the refractive index (calculation reported in Appendix A) of the 830 nm material are plotted in Figure 2.5, as function of the Al mole fraction x_{Al} along the growth height.

Another main advantage of the FRL is the suppression of higher order transverse modes, useful when single transverse mode operation is required. Moreover, higher order mode

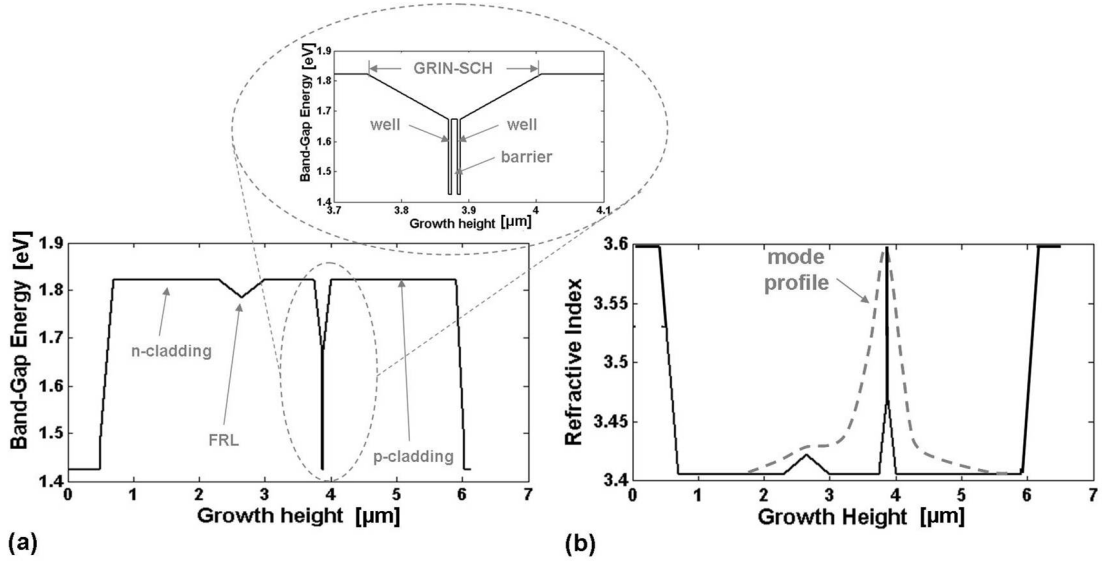


FIGURE 2.5: (a) Bandgap energy as function of the growth height of the 830 nm double QW GaAs/AlGaAs material (calculated as $E_g = 1.424 + 1.247x_{Al}$). (b) Refractive index as function of the growth height (calculation reported in Appendix A). The dashed line illustrates the vertical mode profile enlarged towards the n -cladding.

lasing at high injection current levels cause power kinks, with deteriorated beam quality and slope efficiency above the kink [62, 63]. Higher order modes are suppressed in by the FRL because, when the optical beam is attracted towards the bottom cladding, the optical confinement is reduced and the threshold current needed for lasing is increased. This effect is stronger for higher order modes, which will thus experience more loss compared to the fundamental one [62, 63]. The optimization of the minimum Al fraction in the FRL as well as the FRL distance from the active layer allows for single mode operation, remaining efficient also for relatively deep etchings (up to about 200 nm above the QWs). The graded V-profile also considerably improves the growth tolerance in terms of Al mole fraction, compared to step-like profiles [62]. With this design, kink-free powers of up to several hundreds of mW were demonstrated in continuous wave regime [64].

However, the main aim of this material structure is to achieve a higher d/Γ ratio, where d is the well thickness and Γ the optical confinement in the QWs. The reason for this is that an obvious way for increasing the output power of a laser is by increasing the semiconductor area of injection. However, increases in the waveguide width w are undesired when single transverse mode operation is required. On the other hand, advances through using longer cavity lengths L have historically been delayed by high values of the attenuation coefficient α_i [64]. Progress in the technology of diode laser epistuctures has allowed low attenuation coefficients to be realized, opening the avenue for very long devices. Length scaling need to be accompanied by a reduction in the value of the confinement factor Γ of the epistucture, in order to dilute the high intrinsic gain

of the active region, the critical parameter being the d/Γ ratio [62]. High d/Γ ratios are also necessary to reduce the optical mode area and thus the power density in the most sensitive area of diode lasers, namely the region of the QW at the laser facets [62]. Other virtues include a displacement of the field distribution towards the n side of the laser diode, which reduces free carrier absorption, and a reduction of the distance from the QW to the p -contact, which reduces the thermal and electrical resistances [62].

2.2.1 Ridge waveguide design

A common and effective way of providing the lateral confinement of photons and electrons is by etching the semiconductor material usually up to 200-400 nm above the active region, to form the so called ridge waveguide [53]. In order to find the optimal ridge geometry, the refractive index of each epilayer reported in Table 2.1 was calculated (values plotted in Figure 2.5 and calculation described in Appendix A).

The optimal ridge waveguide structure, in terms of highest optical confinement and single transverse mode operation of the laser, was designed using the commercial mode solver BEAMPROP. Figure 2.6 shows the optical confinement as function of the ridge width, for different values of the etch depth, calculated at an operating wavelength of 830 nm. As shown in Figure 2.6, values of the ridge width between 2 and 3 μm and

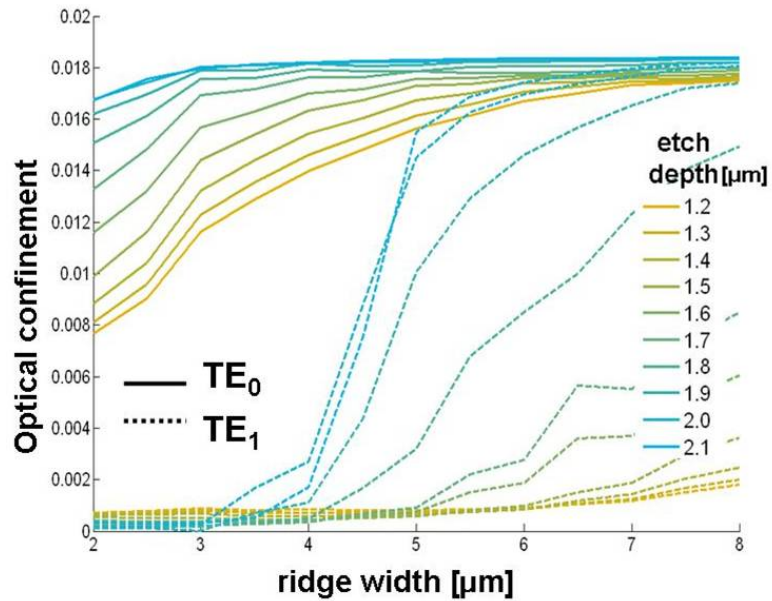


FIGURE 2.6: Optical confinement as function of the ridge width and for different etch depths, relative to the TE_0 and TE_1 modes.

an etch depth between 1.6 and 2.1 μm can provide high confinement and single mode operation. The ridge width was thus chosen of 2.5 μm and the etch depth between 1.7 and 1.9 μm in the fabricated devices. The computed TE_0 mode profile for a 2.5 μm

wide and $1.8 \mu\text{m}$ deep ridge waveguide is reported in Figure 2.7(a), with the vertical cut plotted in Figure 2.7(b). For this geometry, an optical confinement per well of 0.0082 was calculated for both wells, resulting in an effective mode area $A_{eff} = dw/\Gamma = 1.33 \mu\text{m}^2$.

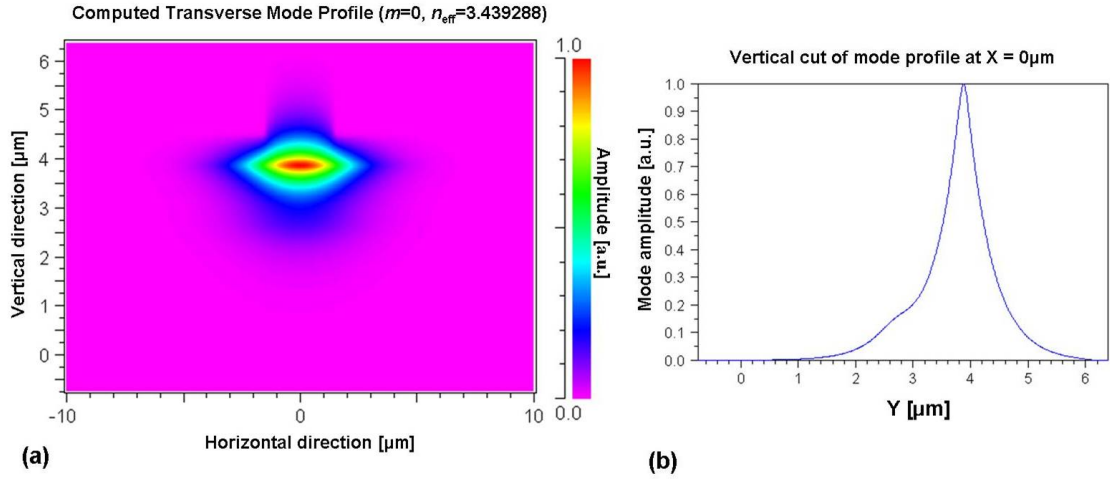


FIGURE 2.7: (a) Computed TE mode profile for a $2.5 \mu\text{m}$ wide and $1.8 \mu\text{m}$ deep ridge waveguide. (b) Vertical cut of the computed mode profile. The vertical mode profile is slightly asymmetric and has a FWHM of $0.6 \mu\text{m}$.

2.2.2 Quantum confined energy levels

The quantized energy levels of the GaAs/ $\text{Al}_{0.2}\text{Ga}_{0.8}\text{As}$ double QW material structure considered in this work were calculated by solving the Schrödinger equation [58, 65]. These calculations, reported in Appendix B, were useful for interpreting the results from material gain and absorption measurements reported in Chapter 4. From these calculations, one bound state for the electrons in the conduction band was determined. This state was found to be at an energy $E_{C1} = 74 \text{ meV}$ above the QW conduction band energy E_c . Moreover, in the valence band, one bound state was found for the light-holes at an energy $E_{LH1} = 44 \text{ meV}$ below the QW valence band energy E_v . For the heavy-holes, two states were obtained in the valence band, with energies of $E_{HH1} = 22 \text{ meV}$ and $E_{HH2} = 76 \text{ meV}$ below E_v . Therefore, three electron-hole transitions were found in this structure, with energies $E_{C1-HH1} = 1.520 \text{ eV}$, $E_{C1-LH1} = 1.542 \text{ eV}$ and $E_{C1-HH2} = 1.574 \text{ eV}$, corresponding to wavelengths of 816, 804 and 788 nm, respectively. The energy bands in the active region are plotted in Figure 2.8.

Due to quantum mechanics selection rules, not all the transitions between all the quantum confined energy levels are allowed in QWs [53, 58, 65]. As a general rule, only transitions between states with the same quantum number can occur [53, 58, 65]. Thus, in our case, only the $C1 - HH1$ and $C1 - LH1$ ones. These transitions are allowed

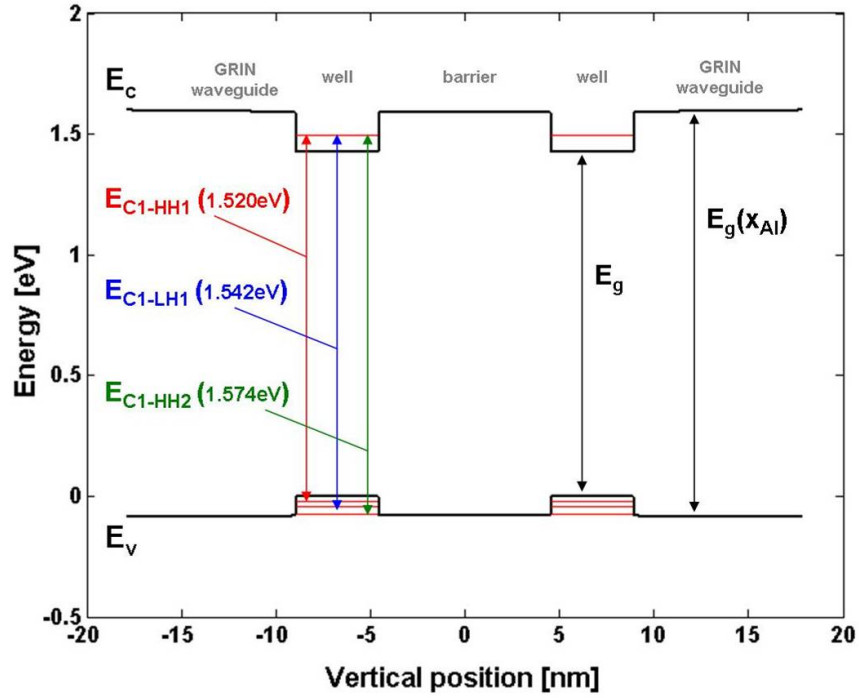


FIGURE 2.8: Energy bands in the active region of the GaAs/Al_{0.2}Ga_{0.8}As double QW material structure considered in this work. Three available electron-hole transitions are indicated as obtained from the calculations reported in Appendix B.

because electrons and holes of these states have non-orthogonal envelope functions (solutions of Schrödinger equation - see Appendix B) and thus give a non-zero contribution to the optical transition matrix element, which represents the strength of the optical interaction of light with each available electron-hole state [58, 65]. However, this is true only with barriers with infinite height (energy), where the quantized momentum does not depend on the effective mass of electron and holes and the envelope functions for electrons and holes have the same momentum [58, 65]. For finite height barriers, like in our case (low Al fraction in the barriers), the different electron and holes effective masses have to be considered when calculating the momentum associated with a particular quantized state. As a result, the non-orthogonality of states with different quantum number can be partially broken, allowing for a small contribution to gain from these transitions [53, 58, 65]. Therefore, it can be expected a small contribution to the gain or spontaneous emission also from the $C1 - HH2$ transition, for high injection levels. Figure 2.9 shows the room temperature photo-luminescence (PL) spectrum of the laser material (courtesy of Bocang Qiu, from Intense Ltd). The main two electron-hole transitions are visible, the $C1 - HH1$ at 816 nm and the $C1 - LH1$ at 804 nm, in good agreement with the values calculated in Appendix B.

The strength of the interaction of light with a given electron-hole state, as quantified with the optical transition matrix element [53, 58, 65], also depends on the direction

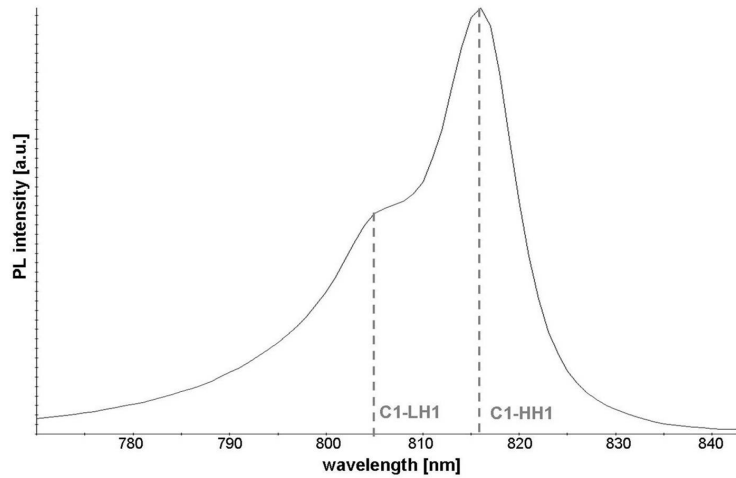


FIGURE 2.9: Room temperature photo-luminescence (PL) spectrum of the laser material (courtesy of Bocang Qiu, from Intense Ltd). The main two electron-hole transitions are visible, the $C1 - HH1$ at 816 nm and the $C1 - LH1$ at 804 nm, in good agreement with the values calculated in Appendix B. PL measurements are explained in Section 3.6.3.

of the electric field of the optical wave (i.e. the polarization of light). This results in a null interaction (at low current density) between transverse magnetic-polarized (TM) light with the $C1 - HH1$ transition, which will thus be available only to transverse electric-polarized (TE) light [53, 58, 65].

2.2.3 Many-body effects

In the calculation of quantum confined states reported in the previous section, electron and holes were considered as free carriers, as a first simple approach for determining the optical transitions of the material. However, in most practical cases, it is also important to consider the mutual interactions of the particles (electrons and holes) in the semiconductor system, often referred to as many-body effects. These include lineshape broadening, exciton states and bandgap shrinkage [53]. The inclusion of these effects was useful for interpreting the results from material gain and absorption measurements reported in Chapter 4.

The first effect, the lineshape broadening, is related to the collisions between particles and/or phonons in the crystal. These cause the broadening of the lineshape function, which represents the energy distribution of the electron-hole transition pairs [53]. The lineshape function, usually described using the intraband relaxation time parameter τ_{in} (i.e. exponential decay of the particle in a given state - around 0.1 ps in bulk GaAs), represents the energy uncertainty (broadening) associated to a given electron-hole transition [53]. In general, the lineshape broadening ($\Delta E_{e-h} = 2\hbar/\tau_{in}$) increases

with temperature and carrier density [58], resulting in a broadening in the gain and spontaneous emission spectra.

A more significant many-body effect at high carrier densities is the bandgap shrinkage. This effect is due to the screening of the atomic forces experienced by the charges at high carrier densities, which weakens the atomic potential with a consequent bandgap energy reduction [53]. This phenomenon is usually observed as a red-shift of spontaneous emission and gain spectra with increasing carrier density [53, 66, 67]. One main consequence of the gain spectrum red-shift in QW semiconductor lasers is the increase in the threshold wavelength, compared to the nominal position of the gain peak [67]. A further red-shift and reshaping (enhanced symmetry) of the gain spectrum is produced by inhomogeneous broadening effects, due to fluctuations in quantum well thickness and composition, or defects and impurities in the material [67].

A third significant effect is the Coulomb interaction between electron-hole pairs, particularly pronounced in semiconductor materials at low temperatures and/or with low carrier densities (when both particle collisions or screening effects are reduced) [65]. The strength of this mechanism depends on the binding energy of the electron-hole pair (referred to as exciton), which is proportional to the Rydberg exciton energy [65]:

$$R_{C-H} = R_y \frac{(m_r/m_0)}{(\epsilon_s/\epsilon_0)^2}, \quad (2.12)$$

where R_y is the Rydberg energy (i.e. unity energy state of the hydrogen atom [65] - 13.605 eV), ϵ_0 the vacuum permittivity, ϵ_s the semiconductor permittivity ($13.1\epsilon_0$ for GaAs), m_0 the free electron mass and m_r the reduced electron-hole mass given by

$$m_r = \frac{m_e m_h}{m_e + m_h}, \quad (2.13)$$

with m_e the effective electron mass in the QW conduction band and m_h the effective hole mass in the QW valence band (light or heavy hole, according to the electron-hole pair involved - see Appendix B). In our material, the Rydberg energy is 4.4 and 3.1 meV for $C - HH$ and $C - LH$ excitons, respectively. In bulk materials, the exciton effect is observed as the occurrence of extra absorption peaks at energies below the bandgap ($E_g - R_{C-HH}$ and $E_g - R_{C-LH}$), as a result of the Coulomb attraction between electron and hole [65]. In QW materials, this effect is enhanced due to the higher confinement of electron-hole pairs, whose binding energy lies between 1 (bulk case) and 4 (pure two-dimensional case) times the Rydberg energy. Therefore, a stronger exciton peak is observed for both $C - HH$ and $C - LH$ transitions, at energies typically between $E_{C1-HH1} - R_{C1-HH1}$ and $E_g - 4R_{C1-HH1}$ for heavy-holes and between $E_{C1-LH1} - R_{C1-LH1}$ and $E_{C1-LH1} - 4R_{C1-LH1}$ for light-holes [65]. In conclusion, in our material,

the $C1 - HH1$ and $C1 - LH1$ exciton peaks are expected to appear at around 825 and 809 nm, respectively, considering a binding energy of $4R_{C-H}$.

2.3 High power operation issues in semiconductor lasers

Output power limitations in semiconductor lasers are generally imposed by the already discussed lateral mode instability and also by facet degradation which leads to catastrophic optical mirror damage (COMD) [68, 69]. COMD was found to be the limit in our devices under continuous wave operation. Classical models describing the COMD mechanism include the following sequential steps: non-radiative recombination at the facet mirror releases thermal energy to the lattice, increasing the local temperature. This induces a band gap narrowing in the region close to the mirrors, that enhances the self-absorption at the facets. The additional free carriers generated, which recombine non-radiatively, further increase the temperature of the facet region. This feedback mechanism can increase the temperature of the facet, which can eventually melt locally [70, 71].

Experimental investigations about the facet local temperature have revealed a thermal runaway initiated for a critical temperature between 120 and 140°C in GaAs/AlGaAs lasers [70]. Compositional changes are observed at the facet during the life of the device. Uncoated mirror facets undergo a fast oxidation process that leads to COMD. The oxidation rate at the facets is enhanced by the local temperature and output light density [70]. The nature of the semiconductors forming the active regions and the cladding layers is determinant for the oxidation of the facets; the Al based compounds are easily oxidized, while Al-free lasers have shown much better facet stability [68, 69]. The interface between the oxide and the semiconductor can be also viewed as a sink for either III or V elements (typically As in GaAs/AlGaAs lasers), leaving behind defects in the active region, which can be vacancies, clusters or stoichiometric defects. These defects can be at the origin of the dislocation loops observed in COMD facets. The facet heating of QW lasers is primarily due to the current injection density [72]. It was demonstrated that the facet temperature of QW lasers can be lowered, reducing the surface current [73]. Since facet degradation is due to the carrier density in the facet region, the first step for suppressing COMD is to ensure that current is not injected near the facet [74]. However, since the main contribution to facet degradation above threshold is from nonradiative recombination of photogenerated electronhole pairs, reducing the absorption coefficient in the facet region is essential.

Non-absorbing mirror (NAM) lasers, also known as window lasers, were developed to increase the power capability of lasers prone to COMD [75]. Increasing the bandgap

energy of the NAM regions at each facet reduces the absorption coefficient, hence the photogenerated carrier density. Quantum-well intermixing (QWI) [75] is by far the most common technique for increasing the bandgap energy of the NAM regions and has proved >300 mW COMD powers in a 830 nm GaAs/AlGaAs material [64]. For this reason NAMs were used in some of our devices. In the next chapter, more details of the QWI process used in this work and the reasons of this choice will be given.

Another common way to avoid COMD is to suppress the facet oxidation by using under-vacuum cleaving and protective coating for the facets [76]. Moreover, the combination of high reflection (HR) and anti-reflection (AR) coatings can be used to unbalance the facet reflectivities and increase (nearly double) the out-coupling efficiency of the laser, without modifying the total mirror loss.

Thermal roll-over is another common limitation on output power in semiconductor lasers. This mechanism is due to the heat generated in the device when large current densities are injected. The induced increase in temperature causes a degradation of the material internal efficiency, mainly due to the increased rate of non-radiative recombinations and leakage of carriers [53].

Within the timescale of this work, the two approaches investigated for improving the COMD power limit are NAMs and protective facet coatings in RWLs. However, only the NAM approach was considered in ML devices.

2.4 Mode locking concept

This section is intended to give some basic theory relevant to the mode locking operation of semiconductor lasers. For a laser above threshold, one or several longitudinal modes satisfying the Equation 2.2 are excited in the semiconductor laser cavity, at the same time. The aggregate electric field of laser radiation is thus the superposition of all the field strengths of individual modes

$$E(t) = \sum_m E_m \exp[j\varphi_m + j(\omega_0 + m\Delta\omega)t] \quad (2.14)$$

where the modes E_m satisfy Equation 2.2. The spectral spacing between adjacent longitudinal modes is thus given by

$$\Delta\lambda = \frac{\lambda^2}{2Ln_g} \quad (2.15)$$

where n_g is the group refractive index and L is the cavity length. If N modes of equal amplitude E_0 are excited, the intensity of light in the cavity is constant and equal to $N|E_0|^2$, if the modes are phase-unmatched. If the phase-matching is achieved, (when

the phases of the longitudinal modes are not only constant but may be considered approximately equal [77–80]), amplitude-modulation of the light is produced within the cavity. This corresponds to an optical pulse repetitively reshaped as it circulates in the laser cavity. The laser thus emits a train of pulses of peak intensity $N^2|E_0|^2$ and duration $\tau_p = 2\pi/N\Delta\Omega$. The pulse repetition rate is equal to an integer multiple M (a harmonic) of the cavity round-trip frequency

$$f = M \frac{c}{2Ln_g}, \quad (2.16)$$

where M is the number of pulses coexisting in the cavity. From Equation 2.16, a rough adjustment of the repetition frequency is possible either by mode locking a laser of desirable length, or, particularly if high-frequency operation is required, using a construction in which $M > 1$ pulses circulate in the laser cavity, simultaneously. In this case, the regime of operation is called harmonic mode locking (HML).

2.4.1 Mode locking approaches

The standard methods of achieving ML are either modulation of one of the laser parameters at frequency f (active ML), or exploiting non-linear properties of the medium, usually by introducing a saturable absorber (SA) into the laser cavity (passive ML). The combination of these methods is known as hybrid ML; in particular, if the external modulation is in the form of short pulses, the corresponding regime is referred to as synchronous ML [58].

In active ML, the gain or loss of the laser is modulated at a frequency synchronized to the cavity round-trip frequency (tens of GHz) or at a harmonic thereof [2]. This modulation is achieved by applying an external electrical signal to a modulation device, such as an electro-absorption modulator. In this way, all of the longitudinal modes resonating within the cavity are intensity modulated at the cavity round-trip frequency, and a constant phase relationship is established between them. Therefore, some form of elongated (extended) cavity is usually required for actively ML lasers to allow modulation at electrically achievable frequencies [58].

In passive ML, no external modulation is required and the phase locking between the cavity modes is achieved efficiently by introducing an intensity dependent (non-linear) loss element into the laser cavity. In the case of diode lasers, the SA usually consists of an additional section to the laser waveguide, which is either reverse biased or is treated by ion implantation to create absorption centres. The SA is usually placed between the active medium and one of the end facets and has the same energy bandgap as the gain section, thus effectively absorbing the generated light [2]. As will be better explained in

next section, the SA is modulated by the optical pulses themselves and narrows them thanks to the saturation mechanism, providing shorter pulses compared to active ML. The absorber saturation is attributed to the band filling effect, whereby photogenerated electrons tend to fill the conduction band due to the low density of states therein, and thus push the absorption edge towards the short-wavelength end of the spectrum. In other words, the majority of states near the bottom of the conduction band become occupied and are therefore unable to accept any further electrons from the valence band [30].

Hybrid ML may be considered as a combination of both active and passive ML, wherein the optical pulses are generated in the same way as in a passively ML laser, but the pulses are synchronized by means of an external electrical signal applied to the absorber [81, 82], or by the injection of subharmonic repetition rate optical pulse trains from an actively ML laser [83]. Benefits here include the possibility to control the pulse timing externally, as in an actively ML laser, whilst achieving shorter pulse durations, as in a passively ML device. There are also associated timing jitter reductions, even with subharmonic modulation.

2.4.2 Conditions for ultrashort pulse generation

The formation of pulses in a laser cavity is due to the interplay between saturable absorption, gain saturation and carrier lifetimes in both SA and gain sections [2, 84]. This interplay requires for several conditions to be satisfied, as described previously in great detail by Haus [78, 85]. At the lasing start up, when the phases of the modes are unlocked, random intensity spikes in the laser cavity can experience less SA loss, due to the absorption saturation. These random spikes are thus repeatedly reshaped (become shorter and of higher intensity) at every round trip, as the low intensity light is absorbed more by the SA [2]. This mechanism leads to the emission of pulses at the round-trip frequency $1/T_R$ (with T_R the cavity round-trip time), if the single pulse in the cavity experiences net gain only in a short temporal window. The described pulse-width shortening process is illustrated in Figure 2.10 [2].

As shown in Figure 2.10, when the randomly formed pulse enters the SA, the leading edge experiences loss until its intensity is high enough to saturate the SA. The SA bleaching produces a window of net gain and thus an increase in pulse intensity. With slow SAs (whose recovery time is longer than the pulse duration, which is the case of semiconductor SAs), the dynamic gain saturation reintroduces net loss on the trailing edge of the pulse [2]. This situation can occur only if the loss saturates faster than the gain (i.e. the saturation energy E_a^{sat} of the absorber must be less than that of the gain

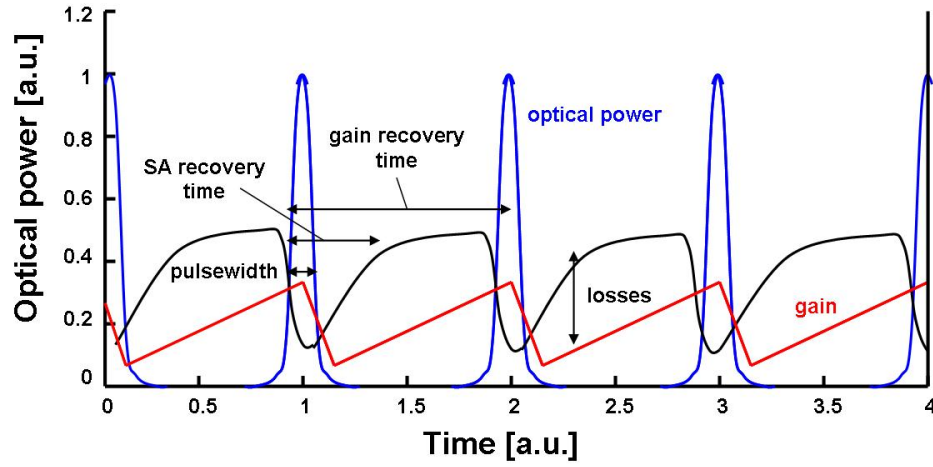


FIGURE 2.10: Time domain explanation of the temporal evolution of optical power, gain and loss in a passively mode locked laser with a slow saturable absorber. The saturable absorber causes a loss modulation, which is fast for the leading edge of the pulse, whereas recovery of the absorber takes some longer time [2].

section E_g^{sat}). This is the main requirement for mode locking [86]. Moreover, as this mechanism has to happen on every pass of the pulse trough the SA, the SA must recover faster than the gain, i.e. $\tau_g > \tau_a$, where τ_g and τ_a are the carrier recovery times of the gain and absorber sections, respectively [2]. In this way, the loss will remain greater than the gain everywhere except for the peak region of the pulse (requirement also known as New's background stability criterion [87]). The requirement on the saturation energies, $E_g^{sat} > E_a^{sat}$, may be analysed further as it is known that the saturation energy of the gain or absorber section may be given by [88]:

$$E_{g,\alpha}^{sat} = \frac{h\nu A_{g,\alpha}}{d(g,\alpha)/dN_{g,\alpha}} \quad (2.17)$$

where h is Planck's constant, ν is the optical frequency, $A_{g,\alpha}$ is the cross sectional area of the laser mode (active region cross section area divided by the optical confinement) and $d(g,\alpha)/dN_{g,\alpha}$ is the differential gain or absorption. Thus the requirement on saturation energies may be rewritten as:

$$\frac{h\nu A_g}{dg/dN_g} > \frac{h\nu A_\alpha}{d\alpha/dN_\alpha}. \quad (2.18)$$

This condition is satisfied in QW lasers due to the non-linear dependence of the gain on the carrier density [53, 89, 90], as shown in Figure 2.11 (here the gain is plotted as function of current density). Here it is known that the modal gain may be well approximated by the simple three parameter logarithmic formula (for $g \geq 0$) [90]:

$$g = g_0 \left[\ln\left(\frac{J}{J_0}\right) + 1 \right], \quad (2.19)$$

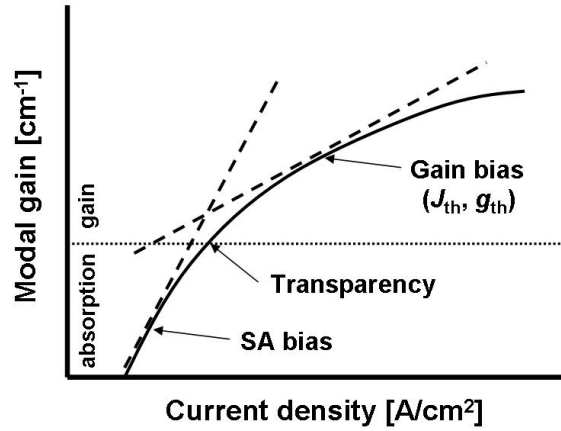


FIGURE 2.11: Schematic illustration of the modal gain (or absorption) versus current density for QW material. The dashes lines represent the differential gain/absorption.

where g_0 is the optimum gain point, J is the current density and J_0 is the point in the curve where g equals g_0 (also the point where the line passing through the origin is tangent to the curve). The differential gain is larger in the absorber section (lower carrier density), compared to the one in the gain section (higher carrier density), ensuring that the aforementioned requirement is met. The reduction in differential gain with increased carrier density is particularly large in QW lasers due to the step-like density of states characteristic [91].

As the relaxation time of QW SAs is usually around 1 ns, too long for ML operation, the requirement on the gain and SA recovery times is usually met by proton or ion bombarding the SA region to introduce defects, or reverse biasing a separated section in the laser cavity, to increase the absorption, thanks to the quantum confined Stark effect (QCSE) [2]. The electric field produced by the applied voltage sweeps out the generated carriers from the absorber region more quickly, therefore decreases the absorption recovery time [2]. As no damage is induced in the material, the technique is thought to be more reliable and is now commonly used in the fabrication of monolithic semiconductor ML lasers.

Apart from the mechanisms mentioned above, there are other non-linearities which contribute to the duration of the emitted laser pulses. Such non-linearities mainly arise due to the very high density of population inversion, of the order of 10^{18} electron-hole pairs per cm^3 , and the broad energy spectra of semiconductor media [30]. Changes in carrier density in the gain section are accompanied by strong self-phase modulation (SPM), i.e. intensity dependent changes in the refractive index along the pulse, due to gain saturation [2]. Chromatic dispersion is another effect, also known as group velocity

dispersion (GVD), by which different spectral components of the pulse travel at different velocities. In this way, these reach the output facet at different times, hence the pulse becomes wider. Dispersion thus imposes chirp on the pulse, i.e. the time domain variation of the instantaneous frequency of the pulse which causes the spread in time of the pulse itself. The pulse-width may only reach a minimum value, i.e. the transform limit, and be unchirped when dispersion is absent in the mode-locking system [2]. SPM in the pulsed regime also imposes chirp on the pulses. If the dispersion is positive, then the SPM of the gain and absorber sections causes serious chirp, which increases with increasing SPM [2]. For negative dispersion, almost no chirp is induced as it is compensated by the chirp caused by the gain and absorber sections. Therefore, the presence of both dispersion and SPM do not necessarily have a detrimental impact on the quality of the mode-locking [2, 92].

2.4.3 State of art performance of monolithic semiconductor passively mode locked lasers

In the last two decades, great efforts have been made and substantial improvements have been achieved in the reduction of the pulse-width in monolithic semiconductor ML lasers. A recent review work [84] has reported that in FP MQW lasers the shortest pulses achieved are of the order of 1 ps (while typical values are around 3-10 ps) and at frequencies up to around 50 GHz at 1.55 μm . The average output power in MQW ML lasers are typically below 10 mW and peak powers of several tens of mW, as pulse gain saturation energies in conventional semiconductor lasers are generally small and in the 0.3-3.0 pJ range. Recent experiments have shown that, in a slab coupled optical waveguide geometry, the gain saturation energies can be scaled up to 30-100 pJ, by increasing the optical mode area and by reducing the overlap of the optical mode with the active region [93]. A schematic illustration of a slab coupled waveguide is shown in Figure 2.12. Average output powers of 200-250 mW and pulsewidths of 5-6 ps (peak power close to 4 W) have been reported in around 8-10 mm long devices with this waveguide design [93–95], at repetition rates of 4-7 GHz. With a similar waveguide structure, 10 ps wide pulses at a record peak power of 5.8 W were achieved at 4.29 GHz in 2006 [96].

Sub-picosecond pulses are usually more easily generated in quantum dot and quantum dash ML lasers with the further benefit of the increase in the pulse peak power. Quantum dot materials have demonstrated several advantages over bulk and QW materials such as low threshold currents, enhanced temperature stability, broad gain spectrum, and reduced linewidth enhancement factor [97–99]. A number of these advantages make QD lasers particularly well suited for use as ML lasers, and as high power laser sources.

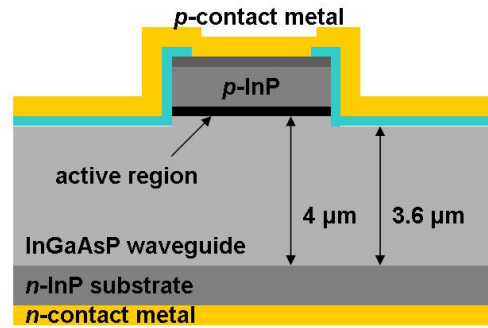


FIGURE 2.12: Schematic of the cross section of the laser. The mode resides mainly in the InGaAsP waveguide layer [94].

The broad gain spectrum and low linewidth enhancement factor of QD lasers have been demonstrated as key elements for generating ultrashort Fourier limited pulses within monolithic semiconductor lasers, and indeed much work has recently been devoted to this area [97–99]. The low saturation energy, weak QCSE and fast recovery time of the QD absorber also make it ideal as a mode locking SA. In standard QD ML lasers, pulses not shorter than 1-3 ps are typically achieved and with average powers not higher than around 50 mW [97–99]. However, the combination of QD materials and flared waveguide geometries, implemented to both increase the output power and to enhance saturation within the absorber, has allowed to achieve transform-limited pulses as short as 360 fs, with peak powers from hundreds of mW up to few W [100–103] (a maximum peak power of 2.25 W [104] was achieved at 1.28 μm). A schematic of a ML laser with a flared waveguide (also called clarinet laser) is given in Figure 2.13. Similar results have also recently been reported from quantum dash ML lasers without flared geometries [105, 106].

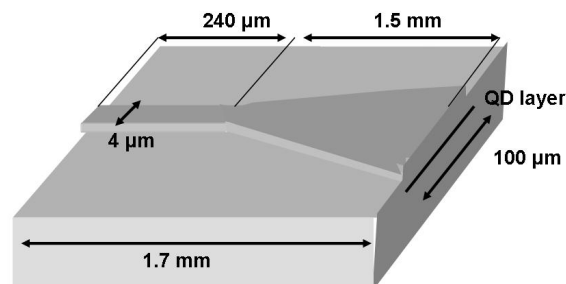


FIGURE 2.13: Schematic of the structure of a tapered waveguide ML laser [104].

2.4.4 Approaches for increasing the pulse repetition rate

In order to achieve sub-THz/THz frequencies, a number of techniques have been proposed. An obvious solution would be to minimise the cavity length L . Sub-picosecond pulses at nearly 200 GHz were obtained using a short-cavity (160 μm long) diode laser with a bulk GaAs active layer and a heavy oxygen implantated SA [107]. Later, the same technique was used to obtain 0.65 ps pulses on a 110 GHz repetition rate from a bulk InGaAsP/InP laser at a wavelength of 1.535 μm [108]. However, practical constraints on the cavity length and low output power preclude further increase of the pulse repetition frequency using this approach. External pulse multiplication techniques allow pulse rates to be multiplied by external processing of the optical signal from a relatively low-frequency ML laser. These include the use of FP interferometers, split-delay-recombine configurations or configurations with a splitter, a couple of band-pass filters and a coupler [109]. Pulse rate multiplication can also be performed within the laser cavity itself, by mode-locking the laser at a harmonic (integer multiple M) of the fundamental (single pulse) repetition rate. This condition is achievable when the saturable absorber is placed in a particular position in the laser cavity, instead of being placed to one end, as in simple colliding pulse mode locking (CPM) or asymmetric colliding pulse mode locking (ACPM). Colliding pulses are produced if the cavity is divided by the absorber in two parts with a length ratio of n/m , n and m being integer numbers without common factors ($n = m = 1$ in CPM, $n \neq m$ in ACPM), as shown in Figures 2.14(a) and (b). Thus the number M of pulses in the cavity is given by the sum of n and m . A similar pulse repetition rate multiplication mechanism is obtained in multiple colliding pulse mode locking (MCPM), with multiple absorbers. These configurations have produced picosecond and subpicosecond pulses at repetition frequencies from tens to hundreds of GHz (with maximum frequencies of about 860 GHz), in both 1.5 and 0.8 μm material systems [110–113], with a maximum excited harmonic of 12.

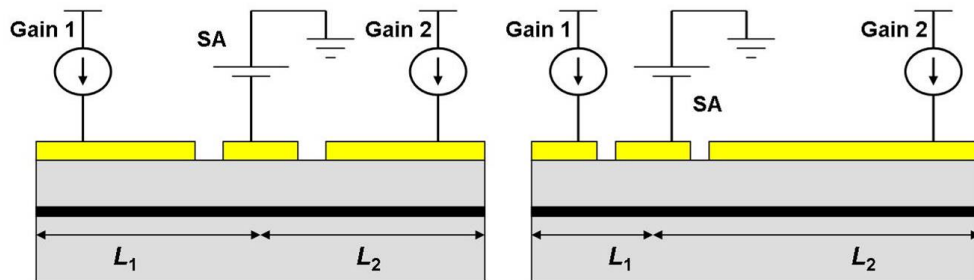


FIGURE 2.14: Schematic of a CPM (left) and of a ACPM (right) mode-locked laser.

However, the highest pulse repetition frequencies and harmonic numbers, to date, have been achieved with a different HML version known as compound-cavity mode locking

(CCM). It was first observed in the unusual behavior of semiconductor laser structures incorporating an SA and a distributed Bragg reflector (DBR) section at high pumping currents [114]. For a DBR section 90 μm long, mode locking at 400, 800 and 1600 GHz was observed with increased pumping levels [114].

As schematically illustrated in Figure 2.15, in the CCM configuration the pulse rate multiplication is achieved by the creation of two coupled sub-cavities of lengths L_1 and L_2 (of ratio $L_1/L_2 = n/m$, n and m being integer numbers without common factors) in the laser cavity (of length $L = L_1 + L_2$). Thus, only the common FP modes of the coupled subcavities are allowed to propagate within the laser cavity. CCM lasers can make use of an external mirror (external cavity mode locking), or proper coupled-cavities configurations using cleaved-facets inter-cavity gaps [115–118], X or Y couplers (non-linear geometries) [80, 119] or an intra-cavity reflector [120], as elements to couple the sub-cavities. The best performances, in terms of stability, ease of realization and highest achieved ML frequencies, have been obtained in monolithic CCM lasers with an ICR. These devices achieved the mode-locking frequency of 2.1 THz [120], record for a semiconductor laser.

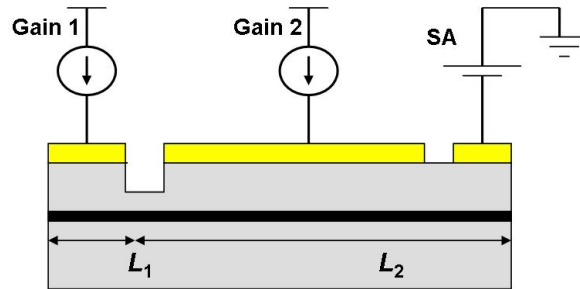


FIGURE 2.15: Schematic of a CCM mode-locked laser.

2.5 Summary of design approaches

In conclusion of this chapter, a summary of the design approaches chosen for the devices fabricated and tested in this work can be given. The first choice that has been explained is about the use of the high d/Γ GaAs/AlGaAs material operating at 830 nm. This material was considered with the intent of exploiting the reduced optical confinement given by the FRL. The FRL ensures high kink-free output powers and the possibility to increase the cavity length with a beneficial improvement in the output power. The use of passivation techniques such as NAMs, obtained by intermixing the regions close to the facets, and protective facet coatings has also been justified for the need to increase the COMD power limit of the devices. Ultimately, two main configurations for achieving

high pulse repetition rates are CCM and CPM (both symmetric and asymmetric) one. However, within the time scales of the project, the author was able to investigate lasers only in fundamental or colliding pulse ML configurations. Moreover, the presence of the SA placed close to the facets facilitates the occurrence of COMD, being a further source of absorption. Therefore, CPM configurations were adopted also to keep the SA far from the facets and far from the NAM regions.

Chapter 3

Fabrication of passively mode locked GaAs/AlGaAs lasers

This chapter is intended to give details of the steps needed for the fabrication of monolithically integrated passively ML lasers in the GaAs/AlGaAs system. Section 3.1 describes in general the structure of the devices considered in this work, with an overview of the fabrication steps involved. The following sections focus on the fabrication stages with some critical aspects or aspects that required some particular development or optimization work. These include electron beam lithography, wet and dry etching processes, quantum well intermixing and *p*-contact pad definition and are reported in summary in Appendix C. Section 3.8 gives a summary of the chapter. Most of the fabrication was done in the James Watt Nano-fabrication Center (JWNC) clean room or in the clean room of the Ranking building of the University of Glasgow. Only in some cases some external partners were involved in the fabrication and will be mentioned in the thesis, where required.

3.1 Fabrication of ridge waveguide lasers with multiple contacts and non-absorbing mirrors

As already mentioned in the previous chapter, the simplest implementation of a passively mode locked semiconductor laser includes a ridge waveguide with two or more *p*-contact sections. One contact is the gain section and the others are the SAs. The SAs have typical lengths between 2 and 15% of the cavity length. The isolation between the contacts is guaranteed by leaving a 10 μm gap between them and by etching the highly doped GaAs cap layer (100 nm in our case) in the gap itself. This procedure produced

good isolation between the contacts, with measured inter-contact resistances of around $5 \text{ k}\Omega$. Figure 3.1 gives a three-dimensional schematic of a typical ML laser with one SA in the middle of the cavity and with NAMs on both facets.

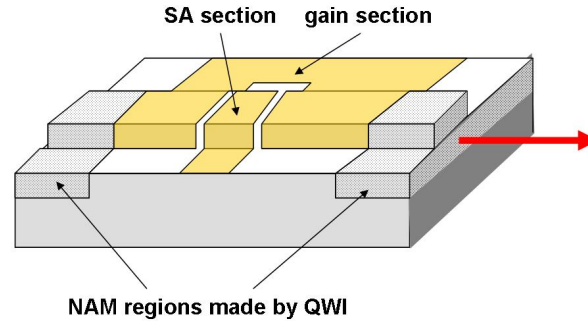


FIGURE 3.1: Three-dimensional schematic of a typical ML laser with one saturable absorber in the middle of the cavity and with non-absorbing mirrors on both facets [121].

The fabrication of the device represented in Figure 3.1 involves six electron beam lithography (EBL) stages. The first stage defines the EBL alignment markers, while the second allows for the definition of the NAM windows, i.e. the regions where the QWI process takes place. This stage is followed by the etching of the ridge waveguides and then by the etching of the gaps that isolate the p -contact pads. In the next step, the contact windows are defined in the silica film on top of the ridge waveguide. The last stage is the definition of the p -contact pads. The fabrication is then completed by thinning the back of the sample to a typical final thickness of $100\text{-}200 \mu\text{m}$ and by the deposition of the n -contact layer on the back of the sample. The sample is then cleaved into laser bars that are fixed on rigid conductive mounts for being tested. In Figure 3.2, the main fabrication steps are listed with schematic drawings illustrating the cross section and planar views for each step. The steps listed in Figure 3.2 are valid for all the devices realized in this work, with minor changes mainly involving some geometrical differences between the devices.

Obviously, for devices without NAMs, the definition of alignment markers and ridge waveguides is done at the same time, reducing the number of EBL steps from six to four. More details about the EBL steps are given in next section.

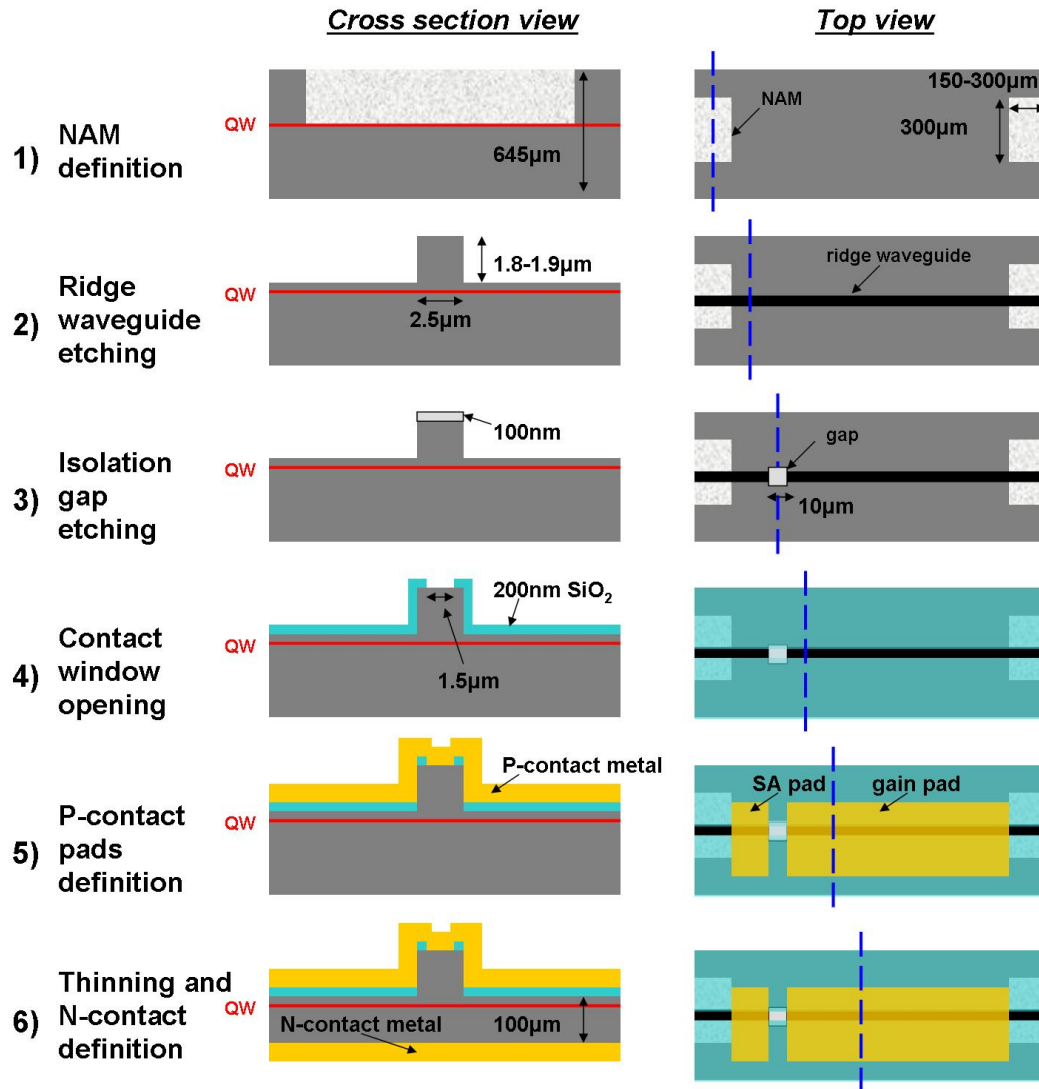


FIGURE 3.2: Steps for the fabrication of a typical ML laser with one SA and NAMs on both facets. In the schematic, both cross section and top views of the device are illustrated, with the blue vertical dashed lines indicating the position in the top view to which refers the correspondent cross section view.

3.2 Patterning using electron beam lithography

A general overview of the lithographic techniques used in this work is given in this section, with particular attention to the electron beam technique. The definitions are mainly taken from JWNC lithography course notes and documentation found in [122], to which the reader should refer for more detail. Lithography is the transfer of a desired pattern into a material. The pattern is defined by exposing a radiation sensitive polymer or a sensitized resin, called resist, which is pre-deposited on the sample surface by spinning. In the optical lithographic techniques, the wavelength used in the exposure (typically in the range of $200\text{-}500\text{ nm}$) defines the minimum feature size achievable. This

type of lithography was used in this work to fabricate the oxide stripe lasers described in Section 4.1, where the pattern resolution was not critical ($75\ \mu\text{m}$ wide features). Another approach is the electron beam lithography, characterized by an extremely high resolution (of the order of nanometer). It consists in a raster scan of a highly collimated electron beam (e-beam) on the wafer surface. It directly writes the pattern into the resist via a multitude of electro-magnets, which are in turn computer controlled [123]. EBL is thus slower but more flexible in terms of pattern definition (no mask preparation is required). In this work, the EBL was preferred over the the photo-lithography for both its higher resolution and pattern design flexibility. A Vistec VB6-UHR-EWF e-beam tool, a state-of-the-art EBL machine with a 50kV e-beam, was thus used for the pattern definition of the structures investigated.

The patterns to be written were prepared using the L-EDIT software, by which the chip layout was created. After opportune file format conversions, the generated layouts were processed with another software that fractures the regions to be exposed in small areas (trapezia), corresponding to each position of exposure of the electron beam. These trapezia are positioned over a square lattice grid and the minimum distance between its points is called the resolution. Row by row, the beam scans the grid horizontally, exposing only dots (with Gaussian intensity profile) separated by a fixed gap: the beam step size (BSS) [122, 124]. The BSS is therefore an integer multiple of the resolution and this multiplier is known as the variable resolution unit (VRU). The beam has a finite width that is defined by the spot size (SS) parameter and depends on the diameter of the aperture and on beam current. The pattern is therefore a discrete set of exposed pixels. The BSS should be a fraction of the minimum feature size (MFS) to be written and typically it is suggested to choose $\text{BSS}=\text{MFS}/5$ [122, 124]. Figure 3.3 shows a schematic illustration of the e-beam writing procedure and parameters.

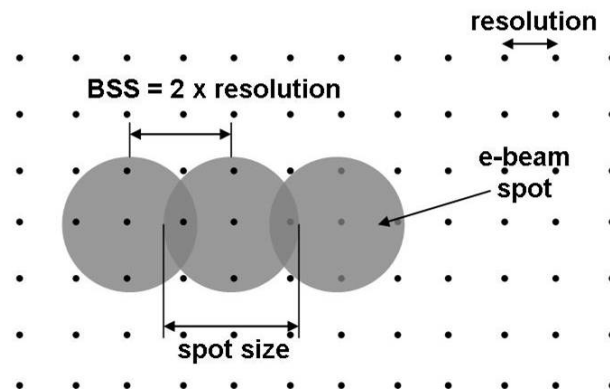


FIGURE 3.3: Schematic illustration of the e-beam writing procedure and parameters [122, 124].

The software BELLE was finally used to submit the pattern to the VB6 tool. The critical details to be specified in BELLE were the beam current, the VRU and the exposure dose (the required charge per unit area ($\mu\text{C}/\text{cm}^2$) to expose the resist). The resist used in the EBL stages was mainly poly-methyl methacrylate (PMMA) of different concentrations and thicknesses, according to the particular use. Therefore, an optimization of the PMMA layer characteristics and e-beam parameters (dose, beam current and VRU) was required.

For the definition of etched alignment markers and ridge waveguides, usually written at the same time, a double layer of 4% 2041 PMMA was used. The mask was realized on the sample surface by spinning each PMMA layer at 5000 rpm for 60 s (which gives a thickness of around 250-300 nm). The first and the second layer were baked after spinning, in a 180°C oven for 30 and 120 minutes, respectively.

For the lift-off stages, required for the definition of NAMs or p -contacts pads, two different layers were used. A more sensitive PMMA (15% 2010) was used as first layer and the 4% 2041 as the second one, baked in the 180°C oven for 30 and 120 minutes, respectively. This particular sequence of PMMA layers has a total thickness of around 1400 nm and guarantees an efficient lift-off of the material deposited on it, if this is not thicker than 400-500 nm. The first PMMA layer is more sensitive to the e-beam and is thus overexposed compared to the one above it, leaving space for the acetone used during the lift-off. This is schematically illustrated in Figure 3.4.

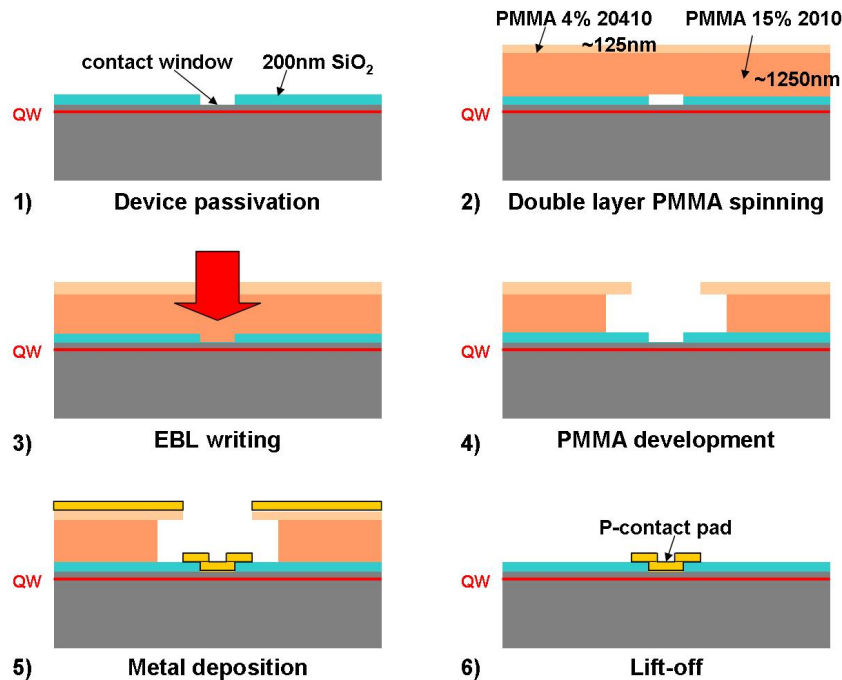


FIGURE 3.4: Schematic of the steps involved in the lift-off process.

In all the cases, the development of the exposed PMMA was done by dipping the sample in the methyl isobutyl ketone (MIBK) : isopropyl alcohol (IPA) (1:1 ratio) developer at 23°C for 35 s, then rinsing it in two beakers of IPA for 30 s each. More details about the lift-off process for the NAMs and p -contact pads definition are given in Sections 3.6 and 3.7, respectively.

3.3 Deposition of silica films

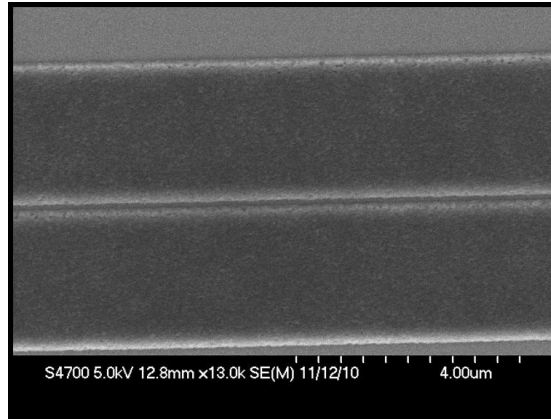
Silica films are typically used as buffer layers between the guiding structures and the metal electrodes. This minimizes the absorption losses due to the interaction of the optical beam with the metal and protects the structure from the outside environment (i.e. dust that produces scattering centers) [124]. These films also allow for confining the injection of current to the path going from the top of the ridge waveguide (p -contact) to the bottom of the substrate (n -contact). Silica films were also used as masks for the various etching processes involved in this work.

Silica films were deposited using a Plasmalab 80Plus plasma enhanced chemical vapor deposition (PECVD) tool. PECVD is a low temperature (around 300°C) method of deposition, where the energy to dissociate the reactants is provided by RF, microwave and photon excitation [124, 125]. In general, gas phase precursors are delivered into the deposition chamber, where free electrons are accelerated by the electric field to create a plasma. The excited atoms are accelerated out from the plasma region towards the deposition substrate, thereby helping to grow a silica coating. The desired stable film is produced as a result of the chemical reaction of the surface with the absorbed species. Therefore, the nature of the deposition is governed by the plasma-induced chemical reactions that produce radicals and ions and by the energy of the reacting species that reach the substrate [124, 125].

Different variables must be taken into account: RF power, temperature and the relative proportions of the input precursors. Each of these variables affects the reactions occurring in the plasma and the interactions occurring on the substrate surface. In this work, however, this process did not require particular development or optimization, as a standard recipe suggested by the JWNC technicians (dry etch laboratory staff: Mr Douglas Lang, Mr Mark Dragses, Mr Ronnie Roger) was used, as summarized in Table 3.1. Figure 3.5 shows an example of pattern transferred into a silica mask. The quality of this silica layer was also found to be characterized by a granular surface, as also visible in Figure 3.5.

Parameter	Value		
	SiH_4	N_2O	N_2
Gas			
Flow [sccm]	9	710	171
Power [W]	10		
Pressure [mT]	1010		
Temperature [°C]	300		

TABLE 3.1: Process parameters for the deposition of PECVD silica films [124, 125].

FIGURE 3.5: Example of pattern transferred on the 200 nm silica film. The pattern contains two $2.5 \mu\text{m}$ wide ridge waveguides, spaced by a 100 nm gap.

3.4 Reactive ion etching

This section gives details of the dry etching processes used for defining ridge waveguides into the GaAs/AlGaAs epilayers and patterns into the silica masks. The silica films were used in this work not only as masks for the GaAs/AlGaAs dry etching steps, but also for passivating the sample surface and defining the contact windows, as illustrated in Figures 3.2 and 3.3.

Dry etching techniques use chemical and physical interactions in plasma discharges (a highly ionized gas containing positive ions and free electrons) to remove the desired material. Wet etching employs liquid based etchants [2, 126]. Dry etching is advantageous compared to wet etching, for its greater repeatability, anisotropy and less mask undercutting, allowing for smaller critical dimensions to be realized [2, 126]. Reactive ion etching (RIE), widely used in our department for fabricating optoelectronic devices, is the best compromise in terms of process anisotropy and selectivity, compared to other available dry etching techniques [2, 126]. RIE was thus used to etch the ridge waveguides.

Typically, in the vacuum chamber of a RIE machine, the chamber itself constitutes a relatively big grounded electrode, while the lower and smaller electrode that holds the sample is capacitively RF coupled, as shown in Figure 3.6. The electrodes asymmetry

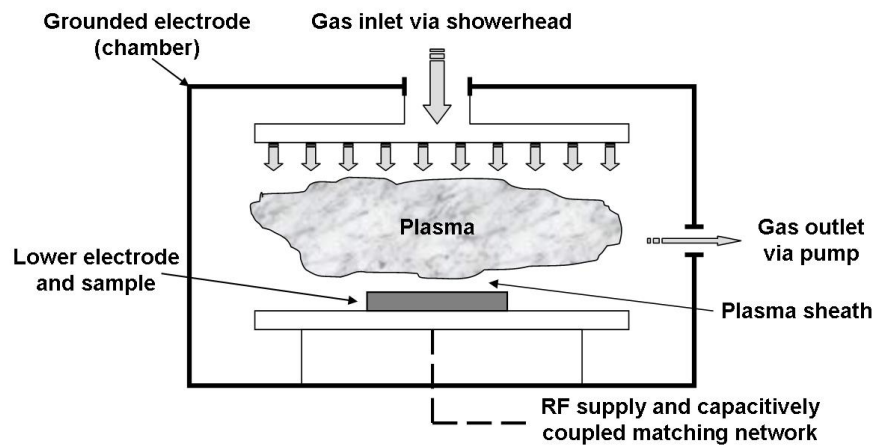


FIGURE 3.6: Typical configuration of a parallel plate RIE system [2].

forces most of the voltage drop between the electrodes, called direct-current (DC) self bias, to occur across the plasma sheath on the smaller electrode. The bias strength is proportional to RF signal amplitude and electrodes area ratio [2]. Low chamber process pressures (typically 5-100 mTorr), that reduce the scattering effects of the ions within the plasma (also known as the mean free path), enhance the RIE directionality.

In general, in a RIE process, the volatile reactive species contained in the plasma are diffused onto the substrate surface to be absorbed and chemically react with it, while the by-product compounds are pumped away from the sample surface. The etching is typically enhanced by physical effects such as ion bombardment [2, 126].

As already explained in the previous chapter, the etching profile of the ridge waveguides is critical for the high power operation of semiconductor lasers. According to the epilayer structure reported in Table 2.1 and to the cross section characterization given in Section 2.2.1, an optimal etch depth of around $1.8 \mu\text{m}$ was required for our devices, in addition to a vertical profile with the smallest roughness possible. A System 100 (S100) (RIE) machine was used with standard process parameters suggested by the JWNC technicians (dry etch laboratory staff: Mr Douglas Lang, Mr Mark Dragses, Mr Ronnie Roger) for the GaAs etching, i.e. SiCl_4 gas with gas flow of 13 sccm, pressure of 5 mTorr and RF power of 250 W. For an accurate control of the etching depth, an etch test was done. For this purpose, six $2\text{mm} \times 2\text{mm}$ samples were patterned in order to have $1\text{mm} \times 1\text{mm}$ windows opened in the silica mask deposited on each of them. Each sample was then etched individually monitoring the interferometric trace usually recorded to control the S100 machine. Figure 3.7 shows an example of the recorded interferometric traces.

The interferometer tool uses an input optical beam that is directed perpendicularly to the sample area to be etched and collects the reflected beam. During the etching, the

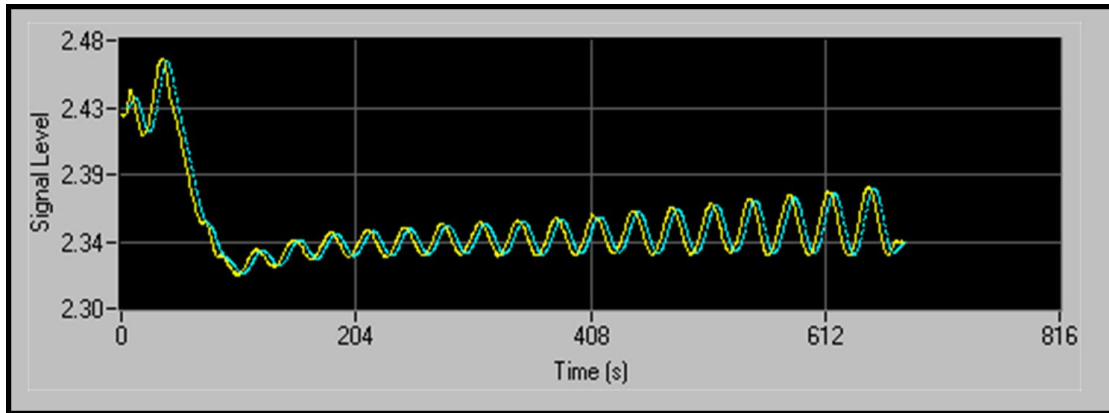


FIGURE 3.7: Example of interferometric trace recorded during the etching process with the S100 RIE machine.

reflected beam is recorded and plotted as function of the etching time. The recorded trace usually takes the form of a wave, with peaks and valleys related to the interferometric pattern generated by the epilayers being etched. As soon as the sample surface is etched, the structure of the superficial layers and thus the reflectivity of the sample change, creating multiple cycles in the interferometric trace being recorded. Each test sample was thus etched for a different number of interferometric cycles. By plotting the measured etch depth as function of the number of cycles for the six samples, it was found an etch rate of 93.9 nm per cycle from the linear fit of the data. Around 19 cycles (12 min circa) were thus used to etch 1.8 μm deep structures. The plot relative to the etch test results is given in Figure 3.8. Examples of etching profiles are shown in Figure 3.9.

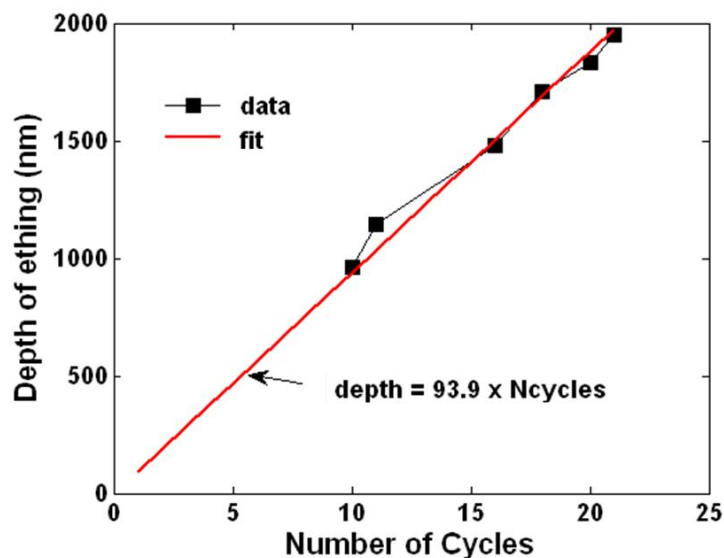


FIGURE 3.8: Etching depth as function of the number of cycles in the interferometric traces recorded during the tests on the RIE process.

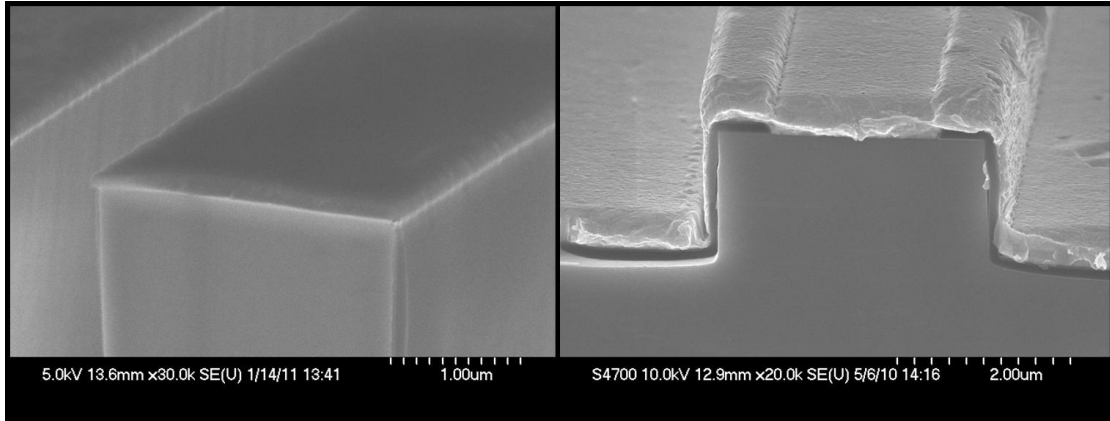


FIGURE 3.9: SEM pictures of dry etched waveguides. In the left image, the ridge waveguide is still has on covered by the silica mask used for the GaAs etching. The right image shows a complete device, with the ridge waveguide covered by a passivating silica film. The contact windows are opened in the silica on the ridge. The whole structure is also covered by the p -contact metal.

Dry etching was also required for defining patterns into silica films. In this case, an Oxford Plasmalab80 Plus RIE tool was used with CHF_3 and Ar gases. The standard process parameters suggested by the JWNC technicians (dry etch laboratory staff: Mr Douglas Lang, Mr Mark Dragses, Mr Ronnie Roger) were: a CHF_3 gas flow of 25 sccm and an Ar gas flow of 18 sccm, a pressure of 30 mTorr and an RF power of 200 W. Although the suggested etch rate was around 30 nm/min, an etching time of 12 min was used for 200 nm thick silica films, in order to guarantee the complete opening of the desired windows.

3.5 Wet etching of GaAs/AlGaAs

In several stages of this work a wet etching of the GaAs/AlGaAs material was needed. In particular, for the removal of the highly doped GaAs cap in the isolation gaps, a selective GaAs/ $\text{Al}_{0.32}\text{Ga}_{0.68}\text{As}$ etching was employed. Another stage requiring the wet etching was the preparation of test samples for the optimization of the QWI process. In this case, the etching purpose was the removal of around 2 μm of material, corresponding to all the epilayers (cap and p -cladding) above the waveguide core. As it will be explained in Section 3.6, this was essential to measure the photo-luminescence spectra of the test pieces and assess the bandgap wavelength shift produced in the wells by the intermixing process. Moreover, in the fabrication of devices with NAMs, some micro-masking problems were encountered during the etching of the ridge waveguides. In this case, as will be better explained in Section 3.6.5, a quick selective wet etch of the GaAs cap layer was used before dry etching the waveguide itself. For these etching processes a citric acid solution was prepared by mixing 1 gram $\text{C}_6\text{H}_8\text{O}_7$ (anhydrous) with 1 ml of

deionized water (DI H₂O), as suggested in [127–129]. Various selective and non-selective etchants are obtained by varying the volume ratio of citric acid to hydrogen peroxide (H₂O₂), as reported in Table 3.2 [127, 128]. The two volume ratios of citric acid to

$C_6H_8O_7 : H_2O_2$	GaAs Etch Rate Å/min.	Al _{0.3} Ga _{0.7} As Etch Rate Å/min.
1 : 2	60	27
1 : 1	69	27
2 : 1	85	24
3 : 1	2169	24
4 : 1	2235	23
5 : 1	3140	27
7 : 1	2882	89
10 : 1	2513	1945
15 : 1	1551	1082
20 : 1	762	918
50 : 1	397	512

TABLE 3.2: Etch rates of GaAs and Al_{0.3}Ga_{0.7} for solutions with different volume ratios of citric acid to hydrogen peroxide [127, 128]. The 5:1 ratio gives a good etching selectivity, while the 10:1 is useful when selectivity is not desired.

hydrogen peroxide used in this work were the 5:1 (with etching time of 1 min), for the selective etching of the cap layer, and the 10:1 (with etching time of 8 min), for the non-selective removal of cap and *p*-cladding layers. All the etchings were performed at room temperature. Approximately fifteen minutes before conducting any material etching, the liquid citric acid/water mixture (considered as one part C₆H₈O₇ in this thesis) was mixed with 30% hydrogen peroxide at a given volume ratio (*x* parts C₆H₈O₇ to 1 part H₂O₂ by volume). The fifteen minute delay is used to allow the etchant to return to room temperature, if any temperature changes occur due to mixing. Before etching, the samples went through a 1 min O₂ plasma descum and then cleaned in a 4:1 volume ratio of 37% HCl-H₂O solution for 30 s, followed by deionized water rinse and N₂ blow dry, as suggested in [129]. This cleaning procedure allowed for the removal of possible resist residuals or GaAs oxides from the sample area to be etched. Other wet etching techniques used in this work are described in Section 3.6.5.

3.6 Quantum well intermixing for non-absorbing mirrors

Quantum well intermixing is a post-growth technique used to selectively increase the bandgap energy in quantum well semiconductor materials. There are different QWI techniques for achieving the bandgap tuning, but they all rely on the out-diffusion of

atoms from the wells which are substituted by atoms diffused from the barriers [130]. This inter-diffusion results in a smoother barrier-well energy profile as compared to the as grown one, i.e. in the barriers the bandgap is lowered while in the wells is widened, as shown in Figure 3.3.

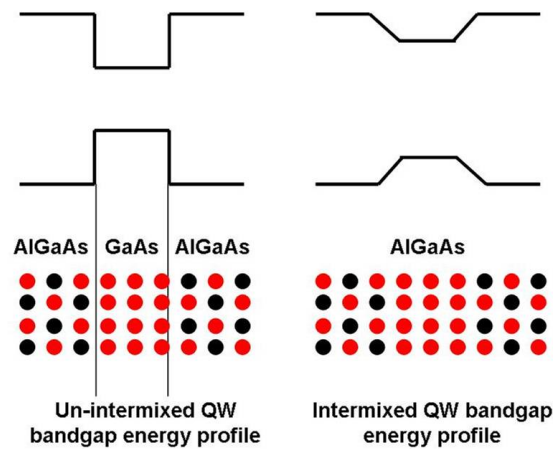


TABLE 3.3: Schematic of the effect of quantum well intermixing on the barrier-well energy profile.

In the QWI process, the wells-barriers atoms inter-diffuse in such a controlled way that the shape of the wells and the quantized states are modified. The result is a blue-shifted band edge. The inter-diffusion at the metastable barrier-well interface happens when the material is exposed to high temperatures [130–132]. Several QWI techniques have been proposed in literature, differing one from the other in the way of introducing vacancies in the semiconductor material. As already explained, the presence of these vacancies is the crucial condition for a selective inter-diffusion of atoms during the annealing step.

3.6.1 Quantum well intermixing techniques

A well known QWI technique is the impurity-induced disordering (IID), where electrically active impurities are introduced in the material to be intermixed, by surface dopant diffusion or ion implantation [133]. These impurities (typically Si or Zn) modify the Fermi level and thus the equilibrium defect concentration, with an increase in the group-III or group-V atoms self-diffusion rate. Although successful with GaAs/AlGaAs, InGaAs/InGaAsP and InGaAs/AlInGaAs systems, this technique has the disadvantage of degrading the electrical properties of the material, due to the presence of dopants or implantation damage. These disadvantages are not present in the impurity-free vacancy disordering (IFVD) technique [134]. Here, a dielectric cap layer is used to promote the out-diffusion of selected atoms at the surface and create point

defects which diffuse in the wells during the annealing. Typically, PECVD SiO₂ cap layers are used in GaAs systems for the out-diffusion of Gallium and PECVD SiO₂ on an InGaAs cap for InP based systems. In this case, the disadvantages are related to the high annealing temperatures required for high bandgap shifts, which can induce undesired chemical reactions between the cap and the semiconductor (particularly in Al based systems) or undesired effects due to the poor thermal stability of the material being processed. In the photo-absorption induced disordering technique (PAID) [135], the quantum well structure is irradiated with laser light (typically Nd:YAG) to produce a high photo-generated (band-to-band absorption) carrier density, that locally heats the well/barrier interface. Although the material quality is excellent in this method (no electrically or optically active impurities), the heat flow limits the spatial resolution of the process. Other techniques using laser light are light-induced disordering (LID) [135] and pulsed-PAID [136], where the exposed material is melted to create new alloys during the re-crystallization or thermally expanded to produce point defects, respectively. In both cases, the disadvantage is the poor control of amount and selectivity of intermixing. In the ion-implantation induced disordering [137], the point defects are generated on the material surface by high energy impacts produced by ion implantation. Electrically inactive species like P and As are used with promising bandgap shifts and spatial resolutions. Another common QWI technique is the sputtering-induced disordering (SID) [138], where the defects are created by the sputtering of a SiO₂ layer on the material surface. High band-edge shifts can be achieved with this process, with a good spatial resolution (few tens of microns) obtained by protecting with PECVD SiO₂ and resist the areas to be left un-intermixed. A similar SID approach was used in this work and it will be better explained in the next section.

3.6.2 Fabrication of non-absorbing mirrors

The quantum well intermixing technique chosen for the fabrication of NAMs is the SID technique, for its achievable high bandgap shifts and high spatial resolution [130, 138]. For the purposes of this thesis, this technique was optimized for the 830 nm laser material in use. In the QWI process considered, a SID layer was deposited on a sample patterned with PMMA. After the deposition, a lift-off was used to selectively remove the SID layer from the sample regions protected by the PMMA and a 200 nm thick layer of PECVD silica was deposited on the whole sample area. Finally, a rapid thermal annealing (RTA) process was used to activate the QWI process in the regions covered by the SID layer. These steps are illustrated in Figure 3.10. As shown in Figure 3.10, the SID layer was obtained by two subsequent sputtering steps, where a first layer of Cu (around 2-3 nm) and then a second SiO₂ layer (around 230 nm) were deposited. The PECVD SiO₂ layer

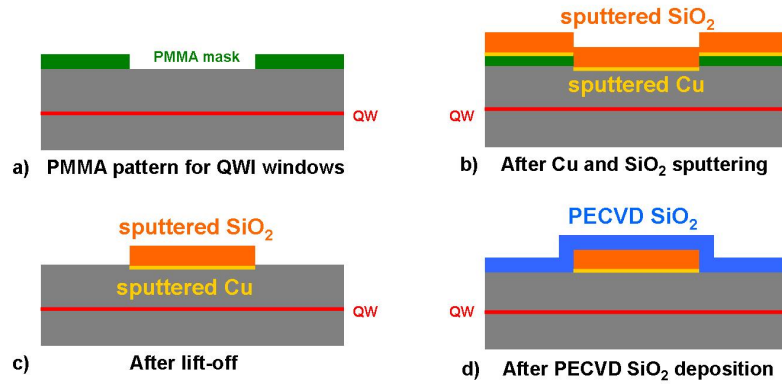


FIGURE 3.10: Schematic of the QWI process steps [121].

was used to suppress the intermixing in the regions where this was not desired. It should be noted that this sputtering technique belongs, in theory, to the family of the IFVD QWI techniques, as it is based on the vacancy disordering produced by the sputtering of the SiO₂ layer. This layer also acts as an attractor for the Ga atoms out-diffusing from the wells during the RTA step, with a consequent migration of vacancies into the active region. It has been shown that the use of Cu during the sputtering step enhances both the production of point defects (i.e. vacancies) on the semiconductor surface and the migration of these into the sample, giving better bandgap shifts with lower annealing temperatures [131]. Cu is known to diffuse interstitially and move onto group III lattice sites through the "kick out" mechanism [131]. However, Cu also represents an impurity in the semiconductor material. It is then important to control its concentration and its distance from the active region to avoid the degradation of the optical and electrical properties of the devices, being Cu both optically and electrically active [131].

3.6.3 Optimization of the sputtering and rapid thermal annealing processes

The SID sputtering was carried out in a Nordiko sputtering machine, with a structure illustrated in Figure 3.11. Sputtering is a physical vapour deposition (PVD) technique of thin film application, in which material is removed from the surface of a pre-determined target and re-deposited onto a substrate to form a uniform coating [2, 139]. The atoms at the target surface are bombarded from ions of the inert gas used in the sputtering process, usually Argon. When these ions impact upon the target atoms, a transfer of energy takes place in which some of the target species are displaced from the surface and then travel within the chamber to condense on other surfaces, including the substrate [2, 139]. In order to achieve a high number of fast moving ions, the target is immersed within a plasma. A highly negative voltage is then applied to the target surface in order

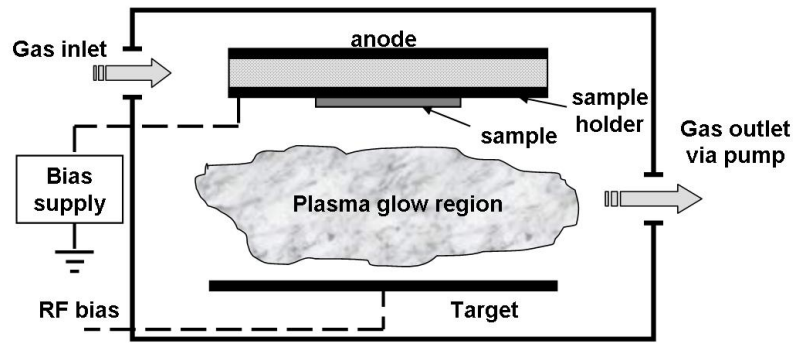


FIGURE 3.11: Schematic of the Nordiko RF sputtering machine used for the SID QWI process [139].

to attract the positive ions towards it [139]. The mechanisms are similar to those of RIE, as described previously.

During both the Cu and SiO₂ sputtering steps, the main process parameters to be controlled were RF power, DC self bias and duration. All sputtering depositions were made by the technician Mr Thomas Reilly. For initial film characterisation, small glass test pieces patterned with half of the area masked by S1818 photoresist were used. The reason for this was so that Dektak surface profiler measurements could be taken post deposition via lift-off processing. For the deposition runs, the process chamber was pumped down to a base pressure of below 4×10^{-6} mbar prior to processing. The sputtering gas mixture of Ar/O₂ (with 10% O₂) was then introduced to the chamber via a mass flow controller (MFC) at a constant flow rate of 35 sccm, giving a chamber process pressure of 3 mTorr (3.99×10^{-3} mbar). The SiO₂ film was deposited for varying times with 200 W being applied to the target, while 60 W were applied for depositing Cu films. The samples were measured using a Dektak surface profiler. The measured film thickness results, with linear fitting, are shown in Figure 3.12. A linear fit to the data yields a deposition rate of around 6.54 nm/min for Cu and 5.23 nm/min for SiO₂.

Temperature and duration are the crucial parameters for the RTA step. The RTA machine used is a J.I.P.ELEC JetFirst Processor tool that has both pyrometer and thermocouple controls, although it was used in the thermocouple control option. This machine has 12 tubular halogen lamps that produce the desired temperature change (up to 1250°C) through infrared emission. A schematic of the RTA tool is illustrated in Figure 3.13(a), while Figure 3.13(b) shows a typical temporal profile of the temperature in the RTA machine.

First attempts to obtain the desired bandgap shifts were made using some standard sputtering parameters suggested by the author's colleague Dr Steven McMaster, working

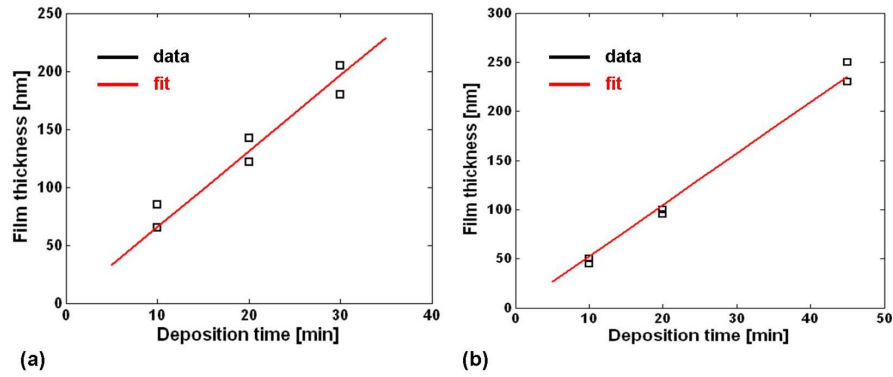


FIGURE 3.12: Measured sputtered film thicknesses as function of the deposition time for (a) Cu and (b) SiO₂. The linear fits to the data yield a deposition rate of around 6.54 nm/min for Cu and 5.23 nm/min for SiO₂.

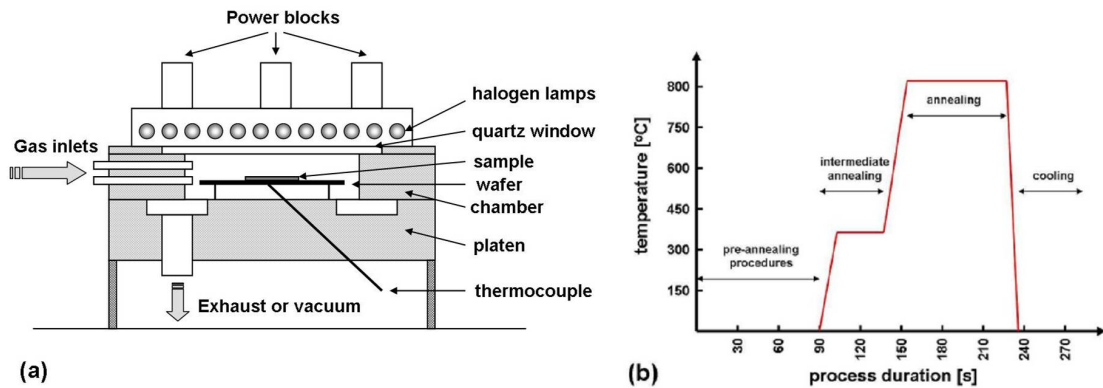


FIGURE 3.13: (a) Schematic of the RTA machine. (b) Typical RTA step temperature profile.

on QWI in the InGaAsP/InP material (reported in the second column of Table 3.4 and named Process 1).

Process parameters	PROCESS 1	PROCESS 2
Ar flow rate [sccm]	35	35
Ar pressure [mTorr]	3	3
Cu target clean (shutter closed) [min]	15	15
Cu deposition time (shutter opened) [sec]	50	25
Cu deposition RF Power [W]	30	60
Cu deposition DC bias [V]	200	400
SiO ₂ target clean (shutter closed) [min]	15	15
SiO ₂ deposition time (shutter opened) [min]	44	44
SiO ₂ deposition RF Power [W]	200	200
SiO ₂ deposition DC bias [V]	0.18	0.18

TABLE 3.4: Parameters for the two different developed QWI SID processes.

Several test samples were processed using Cu sputtering times of 40, 45 and 50 s. From each sample, several pieces of 1x1 mm² were cleaved off and annealed at temperatures

between 760 and 860°C. The annealing time was varied from 60 to 75 s. The maximum shift achieved with these test pieces was of 31 nm (Cu sputtering time of 50 s and an annealing of 60 s at 800°C). Higher bandgap shifts were obtained by increasing the RF power for the Cu sputtering, with the intent of producing a higher damage on the semiconductor surface (higher concentration of point defects). The Cu sputtering time had to be reduced to 25 s to balance the higher RF sputtering power and avoid excessive amounts of Cu in the material. The parameters of this varied process (named Process 2) are reported in the third column of Table 3.4. The measured bandgap shifts obtained from all the test pieces are reported in Figure 3.14.

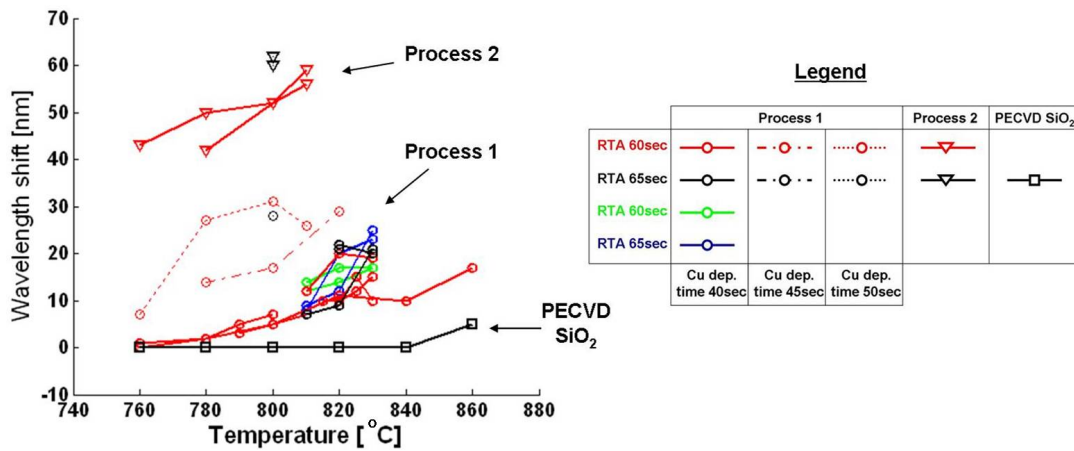


FIGURE 3.14: Bandgap wavelength shifts for different annealing temperatures. The curves marked with circles refer to test samples sputtered with the Process 1 in Table 3.4, while curves marked with triangles refer to the Process 2. The QWI parameters are specified in the legend on the right. The curves marked with squares are samples coated with PECVD silica only.

The bandgap tuning was assessed by measuring the photoluminescence (PL) spectrum of each sample, using the set-up illustrated in Figure 3.15(a). Here, the sample is irradiated with green laser light at a lower wavelength (wider band-gap) than that of the QW material, such that direct band-gap absorption occurs, exciting electrons from the valence to the conduction band. Some of these electrons are trapped by the quantum wells in the conduction band, as are the holes in the valence band. These carriers then relax to the band edge to recombine, emitting photons of energy equal to that of the effective band-gap of the wells [140]. The measurements were taken at 77 K using liquid N₂, in order to lower the rate of non-radiative recombination, allowing for more efficient emission and thus clearer spectra. Figure 3.15(b) shows the PL spectra of the as-grown, PECVD SiO₂ capped and SID-layer capped (Process 2) samples. Process 2 was found to be better than Process 1 (with a maximum bandgap shift of 63 nm) and was thus used for fabricating NAMs in the lasers considered in this work.

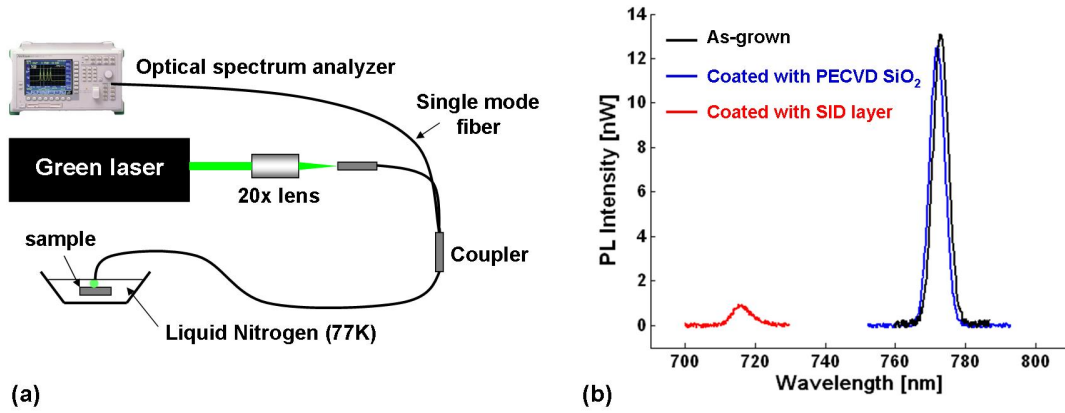


FIGURE 3.15: (a) Schematic of the PL set-up as used in the measurements of the induced band-gap shifts of the AlGaAs MQW material. (b) PL spectra of the as-grown, PECVD SiO₂ capped and SID-layer capped (Process 2) samples, recorded at 77 K.

3.6.4 Lateral grading of the quantum well intermixing process

When using QWI for creating passive sections (like NAMs) on a semiconductor chip, the spatial resolution of the process is a crucial aspect. For the SID technique under investigation, as in other techniques, a spread of the QWI outside the windows exposed to the sputtering is usually seen. This is due to the lateral diffusion of the point defects during the annealing step, which produces a graded QWI profile at the interface between regions exposed and regions unexposed to the sputtering. This results in a grading of the optical and electrical properties of the semiconductor at the interface. To investigate this behavior and to generally evaluate the quality of the developed process, a bar of 1 mm long ridge waveguide lasers was fabricated with QWI windows placed in opportune positions. Figure 3.16 shows a schematic of the laser bar layout. In the laser bar, the 2.5 μm wide ridge waveguides were 200 μm spaced, while the 200 μm wide QWI windows were 175 μm spaced. In this way, the minimum lateral distance between the QWI/non-QWI interface and each ridge waveguide was graded, from the left to the right of the bar, in steps of 25 μm .

For each laser the output light-current (LI) and voltage-current (VI) curves were measured in order to evaluate the grading of the threshold current, slope efficiency, emitted wavelength, voltage and resistance as function of the lateral distance. The VI curves of all the tested lasers are shown in Figure 3.17. Here one can see how this QWI technique does not significantly affect the built-in voltage and the resistance (the slope of the curve above the turn-on voltage) of the devices.

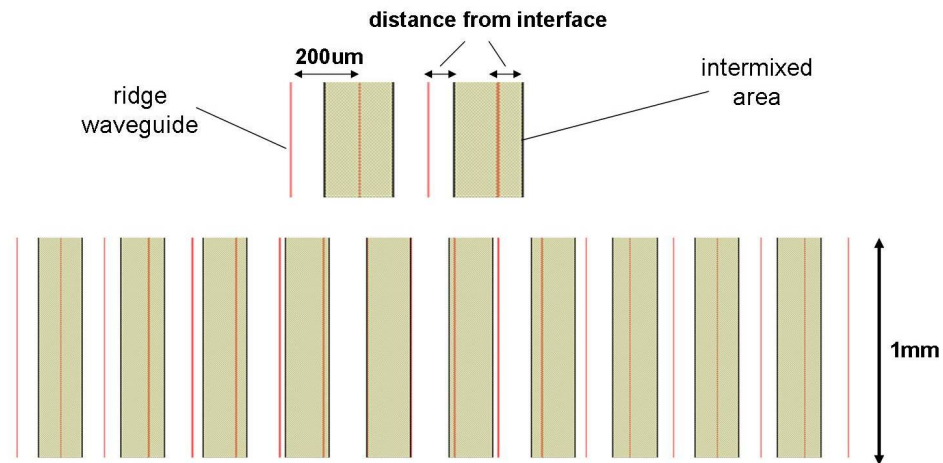


FIGURE 3.16: Schematic of the laser bar fabricated for the evaluation of the QWI lateral grading.

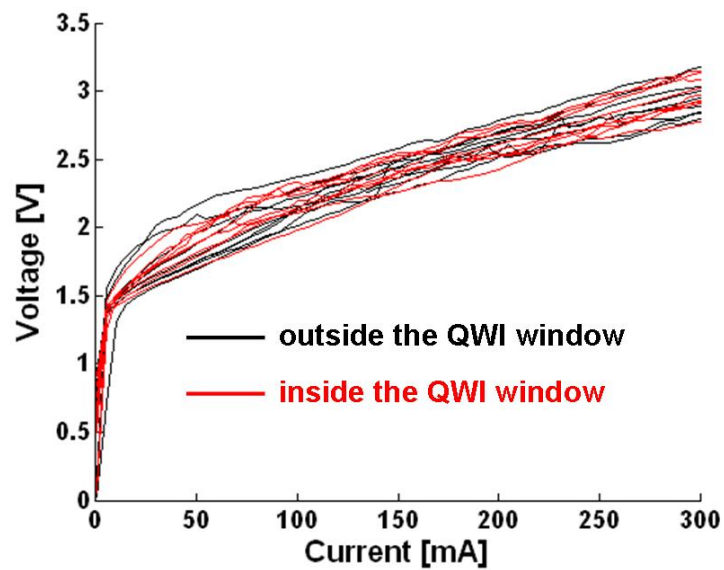


FIGURE 3.17: VI curves for lasers with distances from the QWI/no-QWI interface varying from -125 to $150 \mu\text{m}$. As it can be seen, both the turn-on voltage and the resistance (the slope of the curve above the turn-on voltage) do not vary significantly with the lateral distance from the QWI interface and no particular trend is observed with the varying distance.

In Figures 3.18(a) and (b), the measured slope efficiencies and threshold currents are reported as a function of the minimum lateral distance of the lasers from the QWI/non-QWI interface. These results suggest that the optical properties of the material are degraded up to 100-125 μm outside the QWI window. Figure 3.19 shows the measured optical spectra of the lasers at 200 mA, for different values of the lateral distance.

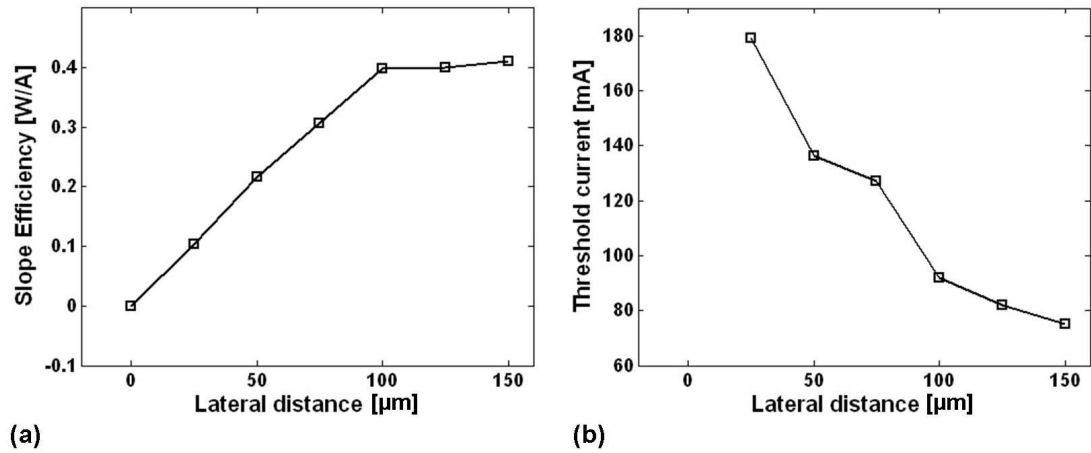


FIGURE 3.18: (a) Slope efficiency and (b) threshold current grading as function of the laser distance from the QWI/non-QWI interface.

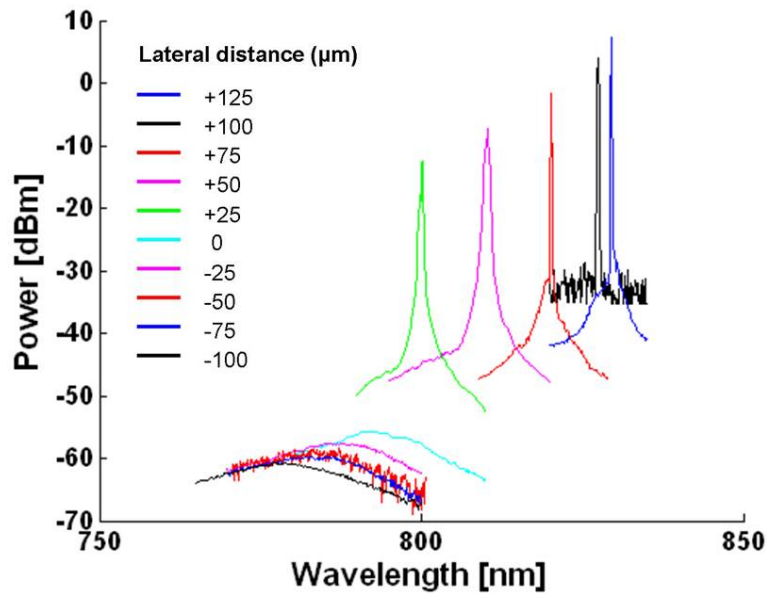


FIGURE 3.19: Optical spectra for lasers with different distances from the QWI/non-QWI interface.

One can firstly note that the lasers positioned in the QWI window or at its interface did not lase. Furthermore, it is clearly visible that the effect of the QWI on the optical gain is gradually stronger when moving from outside the QWI window (positive values of lateral distance) to inside it (negative values), as expected from the corresponding decrease in

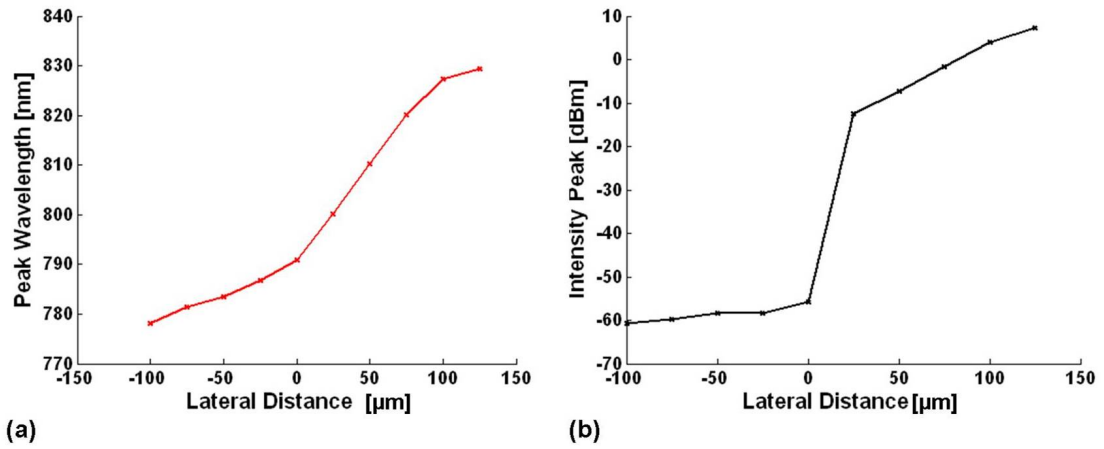


FIGURE 3.20: Optical spectrum peak wavelength and peak intensity for lasers with different distances from the QWI/non-QWI interface.

the peak-value and peak-wavelength of the optical spectra. These results suggest that the NAMs fabricated at both facets of a laser are expected to have dimensions larger than desired. In particular, for 150 μm long NAMs, one may expect an effect of the QWI outside the sputtered section, with a strength that gradually decreases when moving from the NAM toward the center of the gain section. As the measured maximum lateral grading is around 125 μm , one may consider an averaged effect with an extra length of around 60 μm for each NAM and thus a gain section around 120 μm shorter than its designed length.

3.6.5 Intermixing process reliability and repeatability

The QWI process considered in this work required great efforts in terms of reliability and repeatability, due to the several critical steps involved in it. The first critical aspect is the sputtering process. The sputtering machine used in this work, beside being very old and thus not completely reliable, is not computer controlled and had to be manually operated by its responsible technician, with unavoidable reduced accuracy in the control of the sputtering conditions and duration. This was particularly critical for the deposition of the 1-2 nm thick Cu layer. Figure 3.21 shows an optical microscope image of two QWI test samples, exposed in two different runs to the same sputtering process. The different colour of the two samples demonstrates the different thicknesses of the SID layer deposited in two sputtering runs.

Another aspect related to the type of sputtering machine under use is that this does not have a separate chamber for loading the sample into it, but the load is done directly in the chamber where the targets are set and where the sputtering takes place. This causes repeated exposures of the chamber and of the targets to atmosphere and thus to

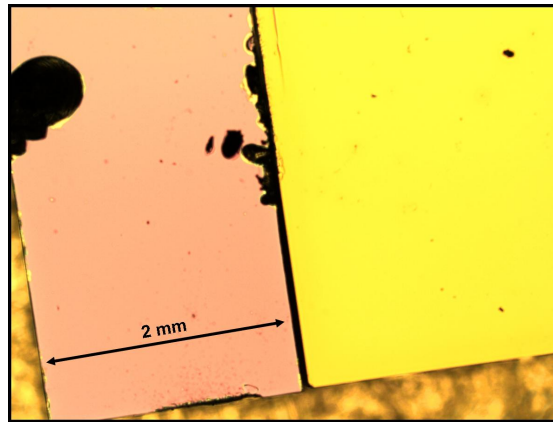


FIGURE 3.21: Optical microscope image of two QWI test samples exposed in two different runs to the same sputtering process.

contamination. This has to be added to two other aspects. One is that different materials (GaAs, Au, Cu, SiO₂, Ti, Ni, Al, Pt, Ge) are deposited with the same machine, that is in turn equipped with only two target holders. This causes the continuous need to replace the targets, to satisfy the needs of different users. Moreover, the machine itself is not placed in a proper clean room environment, causing further contamination of the sample and of the chamber during the loading stage. Figure 3.22 shows an optical microscope image of a sputtered test sample with contaminations of the deposited layer. The contamination spots shown in Figure 3.22 were found really hard to remove after the RTA step, being these transformed in an undefined mask on the sample surface, as shown in Figure 3.23.

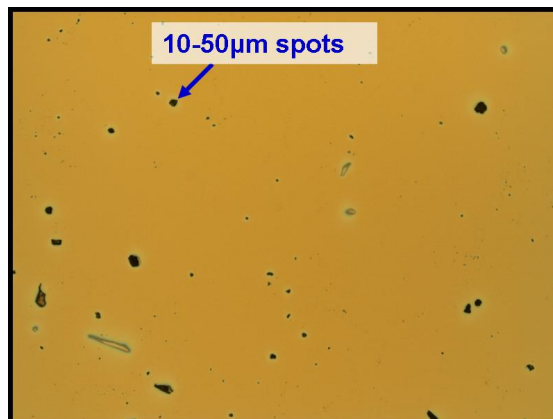


FIGURE 3.22: Optical microscope image of a sputtered test sample with contaminations of the deposited layer. The contaminating spots have dimensions varying from few μm to several tens of μm

The control of the RTA step is also critical for the repeatability of the QWI process, as the bandgap shift induced in the material is strongly dependent on temperature and duration of the annealing. As in the case of the sputtering machine, the fact that the RTA machine was used for several different processes and sample materials was found

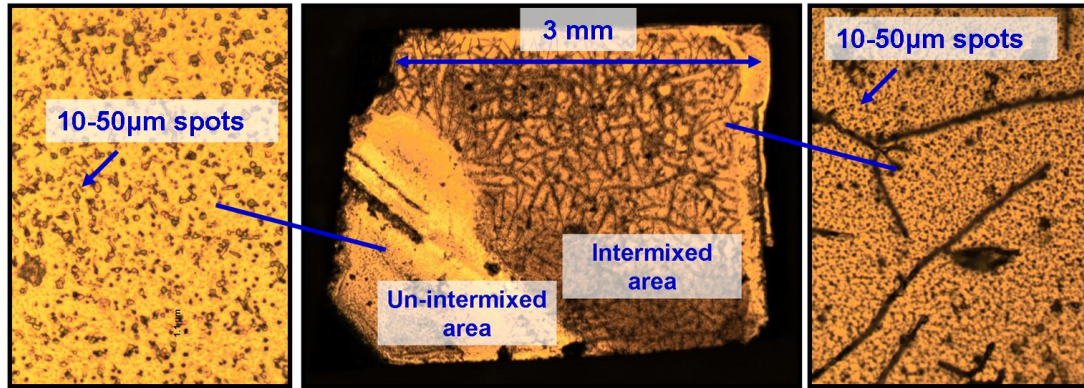


FIGURE 3.23: Optical microscope images of a QWI test sample exposed to a contaminated sputtering. In the central image, one can see the left part of the sample that was coated with photo-resist before the sputtering, in order to make the QWI spatially selective. The details of the unintermixed and intermixed contaminated areas are shown in the left and the right figures, respectively. As can be seen, the contaminations affect the quality of the sample surface also in the areas protected by the resist.

to be a further source of contaminations. For this reason, in all the RTA runs made, the shared sample holder (silicon wafer) present in the machine was replaced by a personal one, always pre-cleaned and only used for the QWI process. In addition to this, before every RTA run, the integrity and position of the thermocouples put in contact with the RTA sample holder were checked, in order to guarantee the same annealing conditions (as the RTA process was computer-controlled through the thermocouples). Moreover, the sample had to be placed on the sample holder always in the same position (on top of the central thermocouple) and covered by the same piece of silicon wafer. The piece of silicon put on top of the sample is essential for avoiding the desorption of the As atoms.

3.6.6 Issues and improvements of the SID layer lift-off

As explained in the previous sections, the definition of the NAMs requires the patterning of a double film of PMMA in order to lift-off the SID layer from the areas to be left un-intermixed. Differently from the lift-off of the p -contact pads, which happens as the last lithographic stage, in this case a long (1 hour minimum) ultrasonic bath could be added to the standard bath in warm acetone (at 50°C for one night), to improve the process cleanliness, without the risk of damaging the waveguides or the contact pads. However, in most cases, residuals of PMMA were left around the edges of the QWI windows after the lift-off step, as shown in Figure 3.24. These residuals or the undesired ones eventually present in the QWI windows themselves were found very hard to remove after the RTA stage. For these reasons, particular attention was given to the cleaning of the sample before and after the sputtering, lift-off and RTA steps. A gentle ash with O₂ plasma at 100 W for 60 s was used after the PMMA development and before the

sputtering. The lift-off itself was improved by following a different set of steps: first was

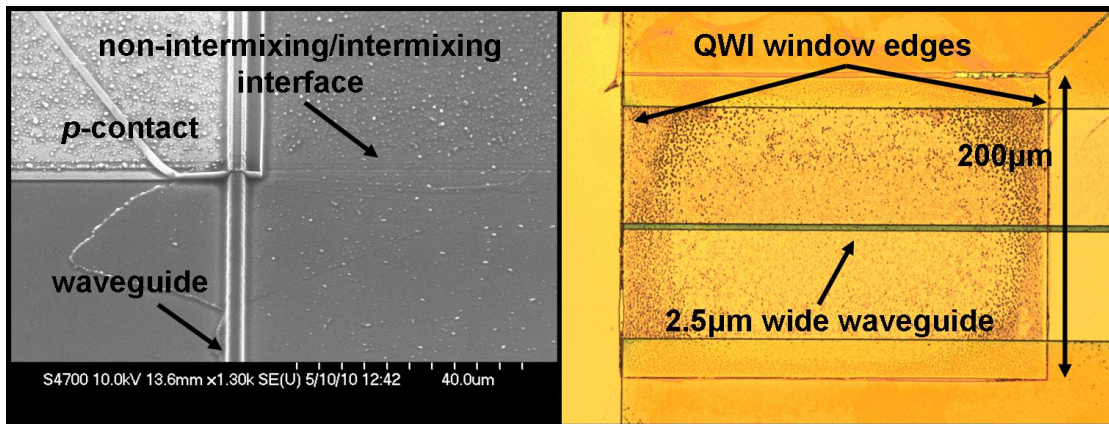


FIGURE 3.24: SEM (left) and optical microscope (right) photographs of NAM regions realized by lift-off of the SID layer, with residuals left on the sample surface.

the deposition of 200 nm of PECVD silica on the sample, second were the spinning and patterning of the PMMA, third the dry etching of the silica and last the sputtering of the SID layer and lift-off. At the end of these steps, further 200 nm of PECVD silica were deposited before the RTA stage. In this way the amount of residuals left on the sample was drastically reduced, as shown in Figure 3.25(a). Finally, optimized cleaning procedures were developed for improving the surface quality after the QWI, particularly to avoid micro-masking problems during the dry etching of the ridge waveguides. An example of a ridge waveguide dry etching affected by micro-masking due to the QWI procedure is shown in Figure 3.25(b). As a first procedure, a longer (8 minutes) hydro-

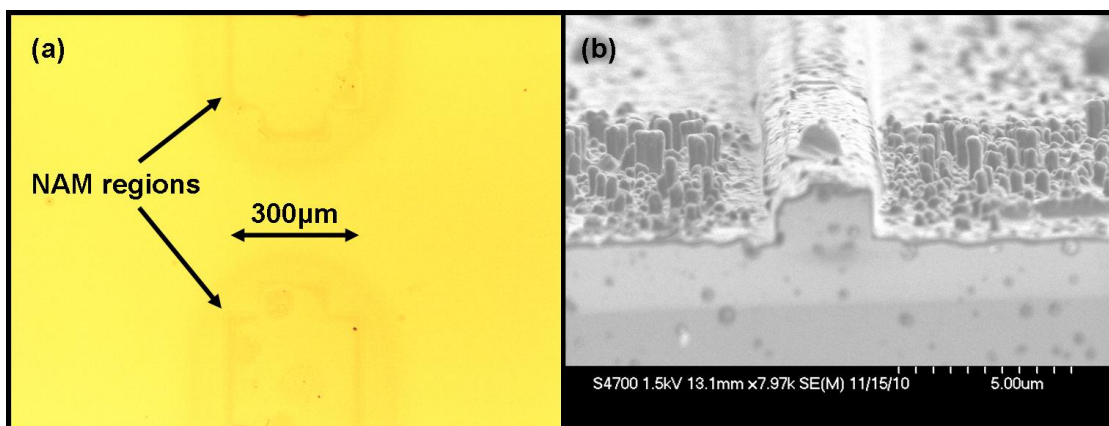


FIGURE 3.25: (a) Optical microscope picture of a sample with NAMs defined with improved lift-off procedures, allowing the reduction of residuals left on the sample surface after QWI. (b) SEM picture of a sample with the ridge waveguides etching affected by micromasking due to residuals left after the QWI process.

fluoric (HF) wet etching (5:1 solution) was used to remove most of the SID layer from the QWI windows. Then the sample was left in warm acetone (at 50°C) for one night and then in an ultrasonics bath for several hours, to remove eventual residuals of PMMA.

Afterwards, a digital wet etching was employed to remove Cu residuals from the sample surface. The digital wet etching consists of two steps that can be repeated several times, according to need. In the first step, the sample surface is oxidized using H_2O_2 for 30 s. In the second one, the thin atomic layer of surface oxide is etched using a 4:1 solution of $\text{HCl}:\text{H}_2\text{O}$ or a solution of acetic acid and hydro-chloric acid ($\text{HCl}:\text{20 CH}_3\text{COOH}$ which removes both GaAs and Cu oxides [141, 142]). When these procedures were not enough, a selective wet etch of the GaAs cap layer was employed before dry etching the ridge waveguides. Figure 3.26 shows a SEM photograph of a ridge waveguide realized with this procedure.

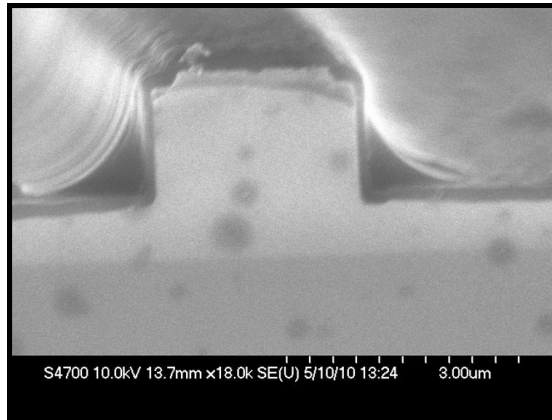


FIGURE 3.26: SEM photograph of a ridge waveguide realized with a wet etch of the GaAs cap layer before the dry etching of the ridge waveguide.

3.7 Definition of device contacts

A crucial aspect of most semiconductor devices and particularly of high power semiconductor lasers are ohmic contacts, which allow the current to flow into and out of the chip. Contacts behaving like resistors (i.e. with a linear voltage-current relationship) are defined ohmic. In practical cases, non-linear rectifying (Schottky) behaviors are typically produced when simply depositing metal onto III-V semiconductors [2]. This happens due to the large potential barrier occurring at the metal-semiconductor interface that produce an asymmetric flow of carriers. However, by highly doping the semiconductor, the depletion region at the interface can be reduced to allow the quantum mechanical tunneling of electrons, thus a linear V-I relationship [2, 143–146]. For this reason, the laser material considered in this work has a 100 nm thick highly Zn doped ($1:10 \times 10^{19} \text{ cm}^{-3}$) GaAs layer for the *p*-type contact and a GaAs substrate doped with Si to a level of $2 \times 10^{18} \text{ cm}^{-3}$, for the the *n*-type contact.

These benefits are enhanced by employing eutectic alloys for the contacts. In particular, for *n*-type GaAs, a Au/Ge/Au/Ni/Au layer structure (with thicknesses 14/14/14/11/240 nm) is deposited using evaporation. The Au/Ge alloy is used because, as Ge is a group IV element, it can dope the GaAs. The layer of Ni is also included to improve surface morphology post annealing, as it does not form an eutectic with the contact metals, at temperatures below the alloying temperature [2].

For the *p*-type contact, Ti, Pt and Au layers are used. The Ti is used as an adhesion layer as it is a reactive metal and oxidizes readily, adhering well to the dielectric layer (SiO₂) used for isolation. However, as the sheet conductivity of Ti is not exceptional (as compared to Au), only a 33 nm thin layer is deposited. The 50 nm Pt layer is used as a diffusion barrier, preventing the Au from penetrating into the semiconductor material [2]. A 240 nm thick top Au layer is used to enhance sheet conductivity, allowing for the device to be tested reliably. These layers were firstly deposited on the samples using evaporation. Then a further 300-400 nm thick layer of Au was sputtered to improve the metal layer uniformity on the ridge waveguides. The contacts are then alloyed using a RTA for 60 s at 380°C. The high temperature anneal also breaks down any native surface oxides between the semiconductor and the metals.

An alternative way of ensuring the uniformity of the metallisation on the ridge waveguide is to implement a planarisation process before depositing the metal, to reduce the sample height disuniformity. For this purpose, a process was developed by the author's colleague Dr Michael Strain. This method makes use of a triple silica layer for the passivation of the lasers. The first and the last layers are PECVD silica films, 200 and 100 nm thick respectively, while the second is a silica film obtained by spinning for 60 s at 4000 rpm the hydrogen silses-quioxane (HSQ) resist, which is then baked at 180°C for one hour. This layer, being deposited by spinning, is not uniform along the sample surface, but is thinner on top of the waveguide, resulting in a more planar sample surface before the metallisation step, as shown in Figure 3.27(b). This variation of the passivation process allows the sputtered 300-400 nm thick Au layer not to be used.

The transfer length method (TLM) was used to assess the quality of the *p*-type ohmic contacts. The test structures consist of several ohmic contact pads, separated by varying gap widths, as shown in Figure 3.28. Using a 4-probe technique (which eliminates the parasitic resistance introduced by probes and connecting wires), current is owed across the gap, with the potential difference measured [2], as illustrated in Figure 3.28.

The resistance R between the pads can thus be measured as a function of gap width x and can be expressed as

$$R = 2 R_c + \frac{R_{sh} x}{W} \quad (3.1)$$

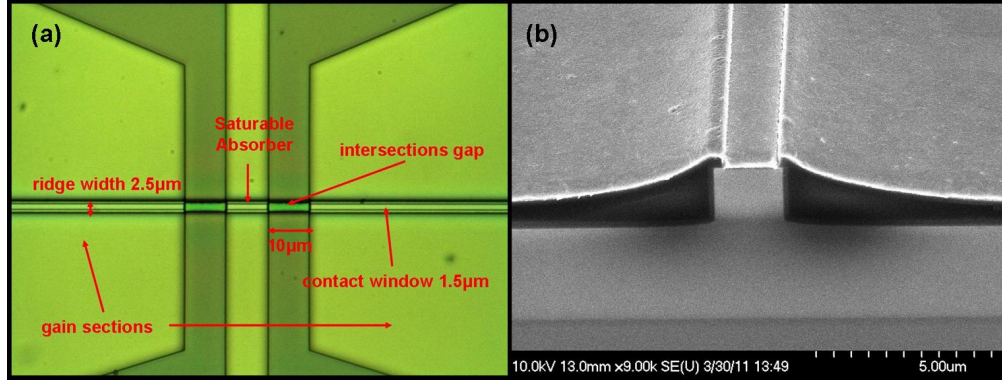


FIGURE 3.27: (a) Optical microscope picture of p -contact pads for a CPM laser, defined by lift-off. (b) SEM picture of the cross section of a ridge waveguide device fabricated using the planarisation procedure.

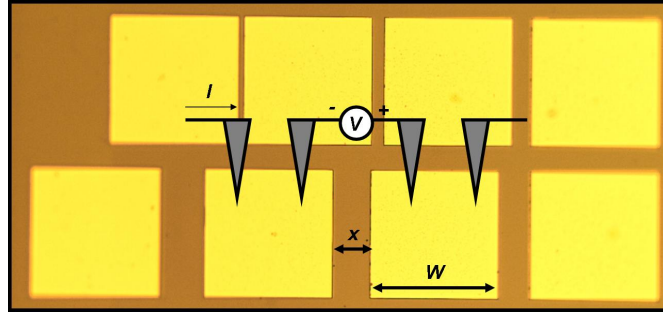


FIGURE 3.28: Optical image of two fabricated TLM test structures for measuring contact resistance. The pad width W is 100 μm and the distance between pads, x , varies in the range 5-35 μm in steps of 5 μm .

where R_c is the contact resistance, R_{sh} the semiconductor sheet resistance (assumed to be the same both between and under the pads) and W is the width of the square contacts [147]. By plotting R as a function of x , one can then infer the value of the contact resistance by linearly extrapolating the data to the intercept with the R axis. The slope of the line is equal to R_{sh}/W , therefore one may also determine the sheet resistivity. Another important quantity, related to the lateral distance necessary for the flow of current into and out of the device, is the transfer length L_t . This is equal to $\sqrt{r_c/R_{sh}}$, where r_c is an important parameter known as the specific contact resistance, measured in Ωmm^2 . The specific contact resistance may also be expressed as $r_c = R_c L_t W$ for $W > 1.5L_t$ [143]. After annealing, the resistance values were measured using a semiconductor parameter analyzer, with the results being plotted in Figure 3.29. The linear extrapolation of the data points intersects the R axis at $\approx 2.8 \Omega$, indicating a contact resistance value of $R_c \approx 1.4 \Omega$. Here $L_t = 3 \mu\text{m}$, $R_{sh} \approx 46 \Omega/\text{square}$ and $r_c \approx 4 \times 10^{-4} \Omega\text{mm}^2$. These results show that the p -type ohmic contacts are suitable for the devices in this research (typical values required lie between $r_c = 0.8$ to $8 \times 10^{-4} \Omega\text{mm}^2$ [147]). Typical values of resistance obtained from the fabricated devices were of few Ω (e.g. 5 Ω for 0.6 mm long and 2.5 μm wide ridge waveguide lasers).

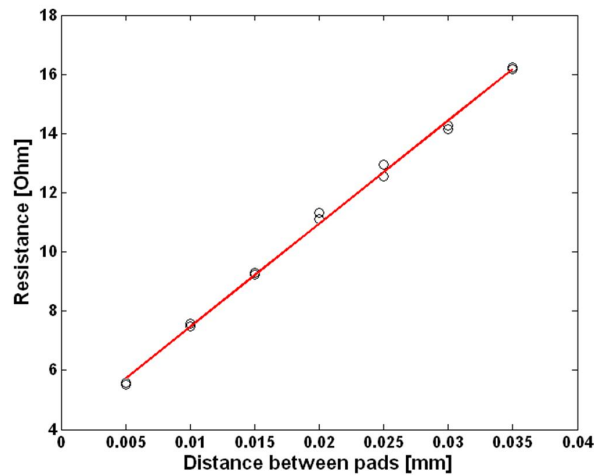


FIGURE 3.29: Results of TLM measurement on highly doped p -type GaAs contact layer, annealed at 380°C for 60 s.

3.8 Chapter summary

The steps used for the fabrication of passively mode locked lasers with non-absorbing mirrors in the GaAs/AlGaAs material under investigation have been explained in this chapter. These steps include electron beam lithography, wet and dry etching processes, quantum well intermixing and p -contact pads definition. These are reported in summary in Appendix C. Significant efforts were required for optimizing the SID QWI technique, chosen for the definition of non-absorbing mirrors in our devices. A maximum bandgap shift of 63 nm was assessed in the intermixed samples, using PL measurements. Purpose-fabricated lasers allowed for the evaluation of the lateral grading of the QWI process, inside and outside the QWI regions. A spatial resolution of around $125\ \mu\text{m}$ was also found. In next chapters, the results from the fabricated devices will be given.

Chapter 4

Material properties and approaches for the characterization of mode locked lasers

In this chapter, some preliminary results recorded for the evaluation of some material parameters are given. In particular, results from oxide stripe lasers are given in Section 4.1, while results from ridge waveguide lasers are in Section 4.2. Multi-contacted ridge waveguide devices, fabricated for measuring the gain and the absorption spectra of the material, are described in Section 4.3, where details of the measurement technique and results are also reported. The effect of the length of the non-absorbing mirrors on the output power of ridge waveguide lasers is discussed in Section 4.4, with considerations on the improvements in COMD power. Increased COMD powers were also obtained with protective facet coatings, as will be discussed in Section 4.5. Section 4.6 gives an overview of the techniques that were considered for characterizing the fabricated mode locked lasers. Particular emphasis is given to the time-domain measurement techniques developed for assessing the emission of pulses and for evaluating their duration.

4.1 Oxide stripe lasers

A common way of assessing material quality is by fabricating and testing broad-area lasers. Indeed, broad-area devices are the simplest type of laser diode, as they do not require any etching of semiconductor material. They can be fabricated simply by defining

metal contact stripes on the semiconductor surface, or by depositing a layer of insulator (silica) and etching contact window stripes followed by blanket metallization. In the latter case, such devices are usually referred to as oxide stripe lasers (OSL). In order to make practice with the fabrication and test of lasers and to have some preliminary information about the 830 nm GaAs/AlGaAs high power material in use, OSLs were fabricated and tested. The fabrication process comprised the cleaning in ultrasonic bath (Opticlear, Acetone, IPA), the deposition of a 200 nm SiO₂ mask, spinning and baking of S1818 photo-resist, UV exposition using a photo-lithography mask with 75 μm wide apertures for the contact windows, development in Microposit developer and an SiO₂ dry etch using CHF₃ to open the contact windows. A second photo-lithography step was then used to define the 120 μm wide *p*-contact pads, followed by metallization, lift-off, thinning to a final thickness of 200 μm, a second metallization for the *n*-contact and a final annealing at 380°C. Figures 4.1 (left) and (right) show pictures of OSLs at the fabrication stage of the pattern for the contact windows defined in the photo-resist and the *p*-contact pads defined after lift-off, respectively. Bars with several 75 μm wide OSLs

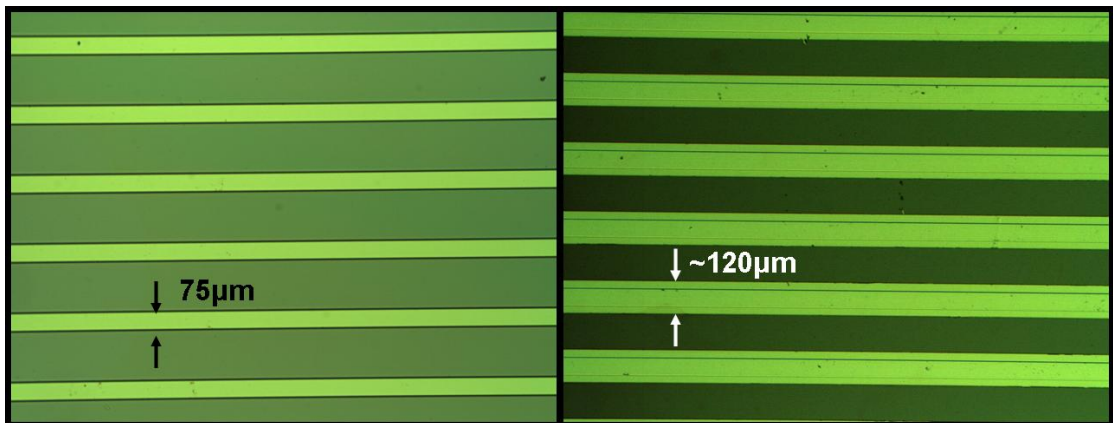


FIGURE 4.1: Optical microscope pictures of the fabricated oxide stripe lasers at the stage of (left) the pattern for the contact windows defined in the photo-resist and (right) of the *p*-contact pads defined after lift-off.

were then cleaved to lengths of 0.5, 1, 1.5 and 2 mm. For all the devices, LI and VI curves were recorded in a pulsed regime (with current pulse-width of 0.5 μs and duty cycle of 0.1%) to avoid heating effects. Figure 4.2 shows the logarithm of the measured threshold current density as function of inverse cavity length, for all the tested devices.

The red line in Figure 4.2 indicates the best fitting curve obtained using the relation:

$$\ln(J_{th}) = \frac{L_0}{L} + \ln(J_\infty), \quad (4.1)$$

where J_{th} is the threshold current density, L is the cavity length, J_∞ and L_0 are characteristic parameters of the material deriving from standard analysis of broad area lasers [58]. From the best fit of the data in Figure 4.2, the parameters $L_0 = 228.6 \mu\text{m}$, $J_\infty =$

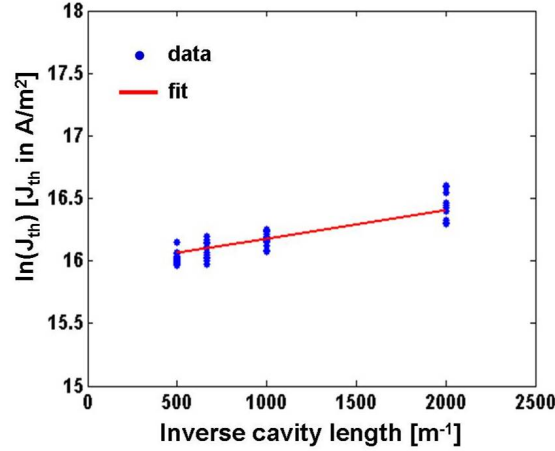


FIGURE 4.2: Plot of the logarithm of measured threshold current densities as function of inverse cavity length of the fabricated OSLS. The red line indicates the best fit of the data.

843.5 A/cm² were determined. Furthermore, L_0 is given by

$$L_0 = \frac{\ln(\frac{1}{R})}{g_0 n_w \Gamma_w}, \quad (4.2)$$

where g_0 is the optimum gain point (with reference to the Equation and Figure), n_w the number of wells (equal to 2 for our material) and Γ_w the optical confinement per well in the active region (equal to 0.0082 in our material) and R is the mean facet reflectivity. From Equation 4.2, $g_0 = 3019 \text{ cm}^{-1}$ can thus be calculated. The modal gain $g_{0m} = g_0 n_w \Gamma_w$ is thus equal to 49.82 cm^{-1} . Unfortunately, the detector used to record the LIs for only these devices was found to be inaccurate (not properly calibrated) and thus the values of the output power were not considered reliable. Therefore, it was not possible to extract the internal loss α_i and the injection efficiency η_{inj} from these data. However, the recorded LIs could still be used for accurately evaluating the threshold current of the devices and thus the material parameters related to it.

4.2 Ridge waveguide lasers

Using the process described in the previous chapter, 2.5 μm wide ridge waveguide lasers (RWL) with an etch depth of 1.8 μm were fabricated and cleaved to lengths of 0.6, 1, 2 and 3.7 mm, in order to perform a material characterization similar to the one presented for oxide stripe lasers. LIs were recorded for these devices and Figures 4.3(left) and (right) show the logarithm of the threshold current density as function of the inverse of the cavity length and the inverse differential efficiency as function of the cavity length, respectively. The performance in terms of threshold current and slope efficiency are

expected to be decreased in ML lasers, where higher losses occur due to presence of the SA, as will be shown in next chapter.

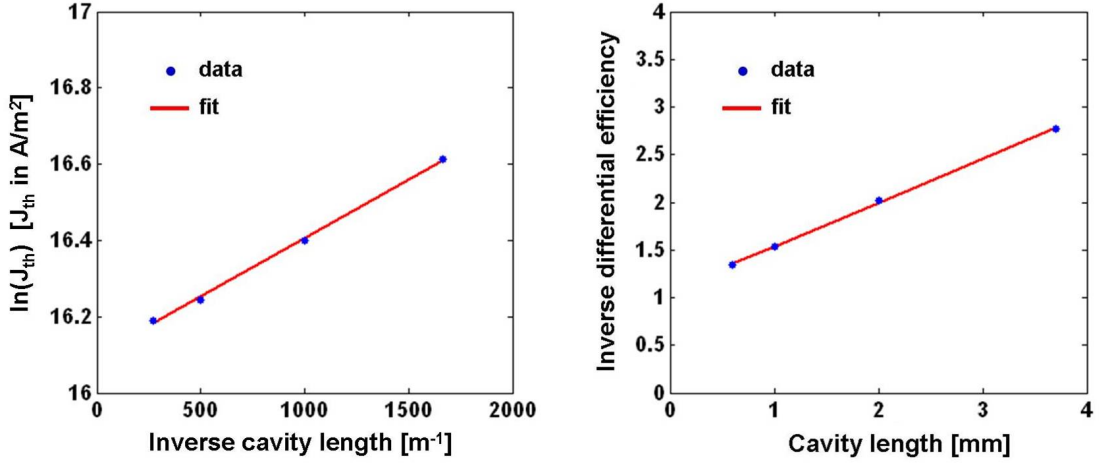


FIGURE 4.3: Plots of (left) the logarithm of measured threshold current densities as function of inverse cavity length and of (right) the inverse of the measured external quantum efficiency as function of cavity length of the fabricated ridge waveguide lasers. the red lines indicate the best fit of the data.

Similarly to the analysis presented in the previous section, from the best linear fit of the data reported in the plot of Figure 4.3(left), $J_\infty = 982 \text{ A/cm}^2$, $L_0 = 305 \text{ }\mu\text{m}$ and $g_{0m} = 37.3 \text{ cm}^{-1}$ ($g_0 = 2261 \text{ cm}^{-1}$) were extracted. Compared to the OSL data, as expected, the value of g_0 is lower and the value of J_∞ is higher, due to the higher waveguide losses of RWLs and their increased junction heating due to the DC testing conditions (OSLs were instead tested with pulsed currents). Moreover, the red line in Figure 4.3(right) indicates the best fitting curve obtained using the relation

$$\frac{1}{\eta_d} = \frac{\alpha_i}{\eta_{inj} \ln(1/R)} L + \frac{1}{\eta_{inj}}, \quad (4.3)$$

where η_d is the differential quantum efficiency, η_{inj} the injection efficiency and α_i the internal losses. The differential efficiency is evaluated from the slope efficiency $\eta_s = dP_{out}/dI$ read from the LIs, using the formula $\eta_d = \eta_s 2q/(h\nu)$. From the best linear fit of the data reported in the plot of Figure 4.3(right), $\alpha_i = 4.86 \text{ cm}^{-1}$ and $\eta_{inj} \approx 0.93$ were extracted.

Knowing J_∞ , g_0 , α_i and η_{inj} , and using the formula [30]:

$$J_\infty = \frac{J_{tr}}{\eta_{inj}} \exp\left(\frac{\alpha_i}{n_w \Gamma g_0}\right) = \frac{J_0}{e \eta_{inj}} \exp\left(\frac{\alpha_i}{n_w \Gamma g_0}\right) \quad (4.4)$$

the value of J_0 was found to be 2177 A/cm^2 , where J_0 is the saturation parameter introduced in Equation 4.1 in Section 2.4.2. The transparency current density J_{tr} can

also be calculated as $J_0/e = 800 \text{ A/cm}^2$ (where e is the Euler's number). The material parameters determined from OSLs and RWLs are reported in summary in Table 4.1

Parameter	L_0 [μm]	g_0 [cm^{-1}]	J_∞ [A/cm^2]	J_0 [A/cm^2]	J_{tr} [A/cm^2]	α_i [cm^{-1}]	η_{inj}
OSLs	228.6	3019	843	-	-	-	-
RWLs	305	2261	982	2177	800	4.86	0.93

TABLE 4.1: Summary of material parameters determined from OSLs and RWLs.

4.3 Gain and absorption measurements

The modal gain spectrum as function of the injection current and the absorption spectrum as function of the applied reverse bias are useful parameters that can be used to model the gain section and the SA section behavior in ML semiconductor lasers [148]. In this work, the gain and absorption spectra were measured using the multi-section technique [149, 150] and were used in Chapter 6 for explaining the SA failure mechanism.

For this purpose, multi-section ridge waveguide lasers were fabricated in the 830 nm material. Multi-section devices are normal ridge waveguide devices, but with multiple contacts of the same length L_{sect} , isolated by a gap etched through the highly conductive cap layer. For this work, $2.5 \mu\text{m}$ wide and $1.8 \mu\text{m}$ deep ridge waveguides devices with four or five equal contacts, isolated by $10 \mu\text{m}$ long and $100\text{--}150 \text{ nm}$ deep gaps, were cleaved to a length of 1 mm . The measured resistance between the contact sections was about $5 \text{ k}\Omega$, proving good isolation between them. Figure 4.4 shows an optical microscope picture of the top view of a device with four contact sections.

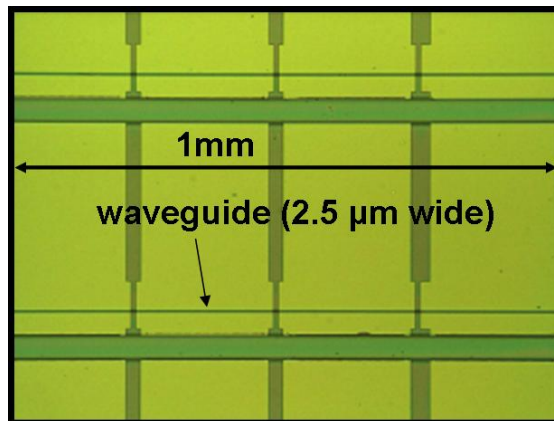


FIGURE 4.4: Optical microscope picture of the top view of a 1 mm long ridge waveguide device with four contact sections. The waveguide is $2.5 \mu\text{m}$ wide and $1.8 \mu\text{m}$ deep.

In the multi-section technique, the two contact sections close to the device output are biased during the measurement procedure, while the remaining ones are reverse biased to avoid the lasing operation of the device and guarantee single pass measurements, as shown in Figure 4.5. Moreover, in some positions of the unbiased sections, some intentional scratches were made, using the current injection probe tip, in order to further suppress beams reflected by the rear facet and propagating towards the output facet.

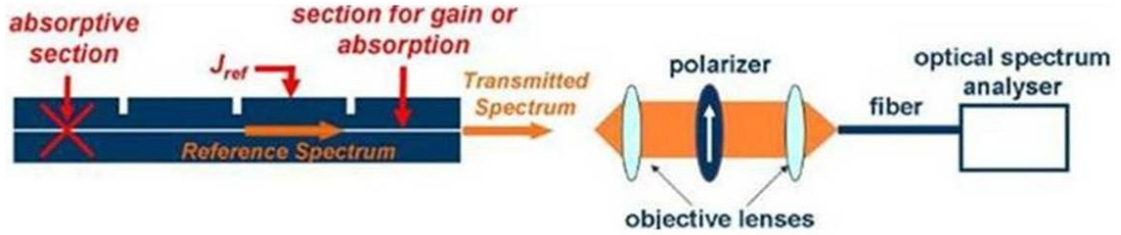


FIGURE 4.5: Schematic of the multi-section device structure and of the multi-section technique measurement set-up. The device is a four contact sections ridge waveguide. The output of the device is collimated and then focused into a fiber using objective lenses. Between the lenses the polarization is controlled using a polarizing beam splitter.

The measurement set-up simply comprises an objective lens which collimates the output beam of the device, a polarizer that selects the TE or TM polarization and a second objective lens that focuses the light into the input fiber of the optical spectrum analyzer, as shown in Figure 4.5. In the technique, a reference spectrum I_{ref} is measured by injecting a reference current density J in the first section. This is then compared to a second spectrum I_2 , obtained by injecting the reference current density in the second section, while absorption or gain is induced in the first one, respectively reverse or forward biasing it, as shown in Figure 4.5. In the measurement of the net modal gain spectrum, the reference current density J is injected in the first section during the second step, while, in the measurement of the absorption spectrum, a reverse field F is applied to it. The two steps iterated for measuring the gain spectrum for each current density are illustrated in Figure 4.6.



FIGURE 4.6: Illustration of the iterated steps of the multi-section technique used for measuring the gain spectrum for each current density. In the first step a reference spectrum is recorded by injecting a reference current in the first section. The same current is then injected in each of the first two sections in the second step and a second spectrum is recorded to be compared to the reference one.

The TE and TM amplified spontaneous emission spectra $I_{ref}(J, \lambda)$, measured for several values of the current density, are plotted in Figures 4.7(left) and (right), respectively.

As shown in Figures 4.7(left) and (right), the reference beam $I_{ref}(J, \lambda)$ is available only

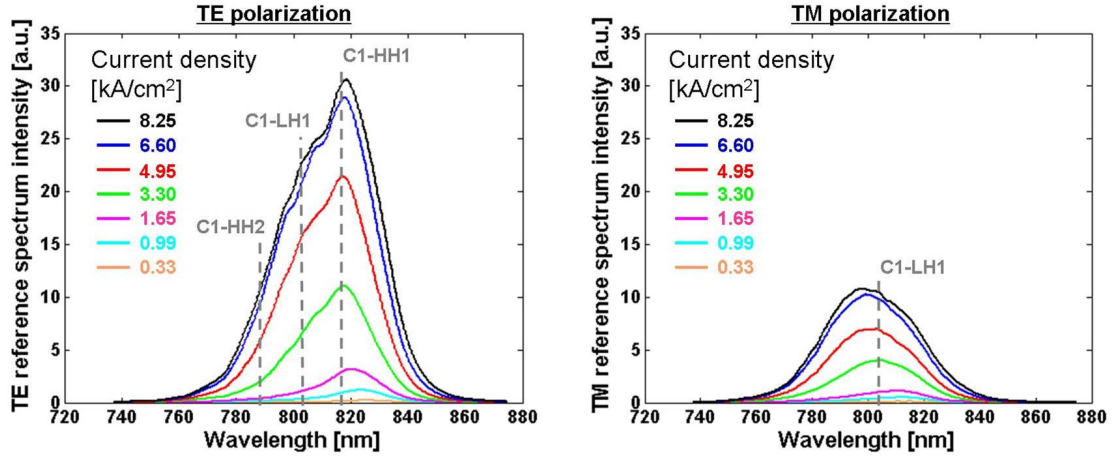


FIGURE 4.7: Measured amplified spontaneous emission spectrum $I_{ref}(J, \lambda)$, for several values of the current density for TE (left) and TM (right) polarized light. The dashed vertical lines indicate the electron-hole transitions associated the our double QW laser structure (as calculated in Appendix B). It can thus be observed that all the transitions are slightly red-shifted (around 10-15 nm) from the respective nominal (calculated) values. The TM spectrum does not show the $C1 - HH1$ transition, as this is not allowed in QW structures [58], while the $C1 - LH1$ transition is allowed for both TE and TM polarizations.

within a limited wavelength range (maximum 780-840 nm at an injection current of 8 kA/cm²), which thus corresponds to the maximum range of validity of the measurement itself. Therefore, one can expect noisy measurements outside this range, particularly for low injected current densities. Figures 4.7(left) and (right) also show the characteristic electron-hole transitions of our double QW laser structure. Moreover, as expected, the TM spectrum does not show the electron-heavy hole transition $C1 - HH1$, while the electron-light hole transition $C1 - LH1$ is observed for both TE and TM polarizations. For high current densities, a weak contribution from the $C1 - HH2$ transition is also observed for the TE polarization. It can also be observed that all the transitions are slightly red-shifted (around 10-15 nm) from the respective nominal values (as calculated in Appendix B). This suggests the occurrence of a thermally-induced bandgap reduction or a bandgap shrinkage due to the high concentration of injected carriers, as already discussed in Section 2.2.3 and as also reported in [53, 66, 67].

With reference to the data acquired with the procedure illustrated in Figure 4.6, the net modal gain was calculated as:

$$G(J, \lambda) = \frac{1}{L} \ln \left[\left(\frac{I_2(J, \lambda)}{I_{ref}(J, \lambda)} \right) - 1 \right], \quad (4.5)$$

where the net modal gain is defined as $G = g_m - \alpha_i = \Gamma g - \alpha_i$. The results of the gain measurements are plotted in Figure 4.8(left) and are in good agreement with other

results reported in literature for similar epilayer structures [58, 151–154]. Figure 4.8(left)

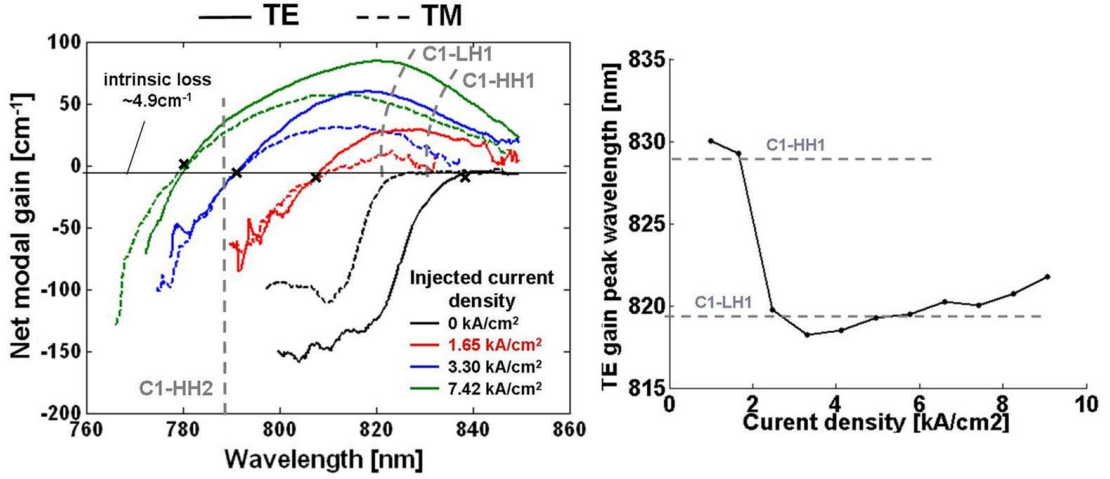


FIGURE 4.8: (left) Plot of TE (continuous line) and TM (dashed line) modal gain spectra, for different injection current densities. The black horizontal line represents the intrinsic loss of the material, found from the crossing points of the TE and TM gain curves. (right) TE gain peak wavelength as function of current density. The TE gain peak moves from around 830 nm ($C1 - HH1$ transition) at low current densities towards around 820 nm ($C1 - LH1$ transition). Both transitions are 10-15 nm red-shifted compared to their nominal value due to many-body effects.

shows that the TE gain is enhanced compared to the TM one, as expected from the stronger optical transition matrix element associated with the $C1 - HH1$ transition [58]. The higher TE gain thus allows for lower thresholds currents to be experienced by TE modes. This effect is further enhanced by the single mode operation provided by the narrow ridge waveguide, as discussed in Section 2.2.1. Therefore, in most cases, only the TE gain spectrum is of interest in QW lasers. The inset of Figure 4.8(right) plots the gain peak wavelength as function of current, showing that the TE gain peak occurs at higher wavelengths compared to the nominal $C1 - HH1$ transition at 816 nm, due to many-body effects discussed in Section 2.2.3. Moreover, as the injection current is increased, the gain peak jumps towards the $C1 - LH1$ transition, while the whole spectrum continues to red-shift and broaden. This is in good agreement with what theoretically predicted in [66, 67] for 5 nm wide GaAs/Al_{0.2}Ga_{0.8}As QWs. Figure 4.8(left) also shows how the intrinsic loss can be evaluated by the crossing points of the TE and TM gain curves [149, 155], found to be around 4.9 cm⁻¹.

The two iterated steps used for measuring the absorption spectrum for each reverse bias applied are illustrated in Figure 4.9.

With reference to the data acquired with the procedure illustrated in Figure 4.9, the absorption was calculated as:

$$\alpha(F, \lambda) = -\frac{1}{L} \ln \left[\frac{I_2(F, \lambda)}{I_{ref}(J_{ref}, \lambda)} \right] \quad (4.6)$$

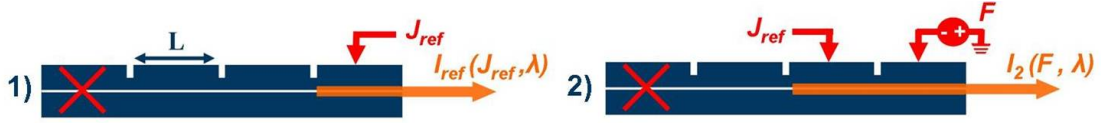


FIGURE 4.9: Illustration of the iterated steps of the multi-section technique used for measuring the absorption spectrum for each reverse field applied. In the first step a reference spectrum is recorded by injecting a reference current in the first section. The same current is then injected in the second section in the second step, while reverse biasing the first section, and a second spectrum is recorded to be compared to the reference one.

The results of the absorption measurements are plotted in Figure 4.10. Here, as already mentioned in Section 2.2.3, it can be seen a red-shift of the absorption edge for both TE and TM spectra, due to exciton effects. Although not clearly visible, the light-hole exciton occurs at around 810 nm (both TE and TM spectrum), while the heavy-hole one occurs around 820-825 nm (TE spectrum only). The fact that both excitons are not clearly distinguishable may be due to one or more of the several factors that generally contribute to weaken the electron-hole Coulomb interaction, such as the presence of the $p - n$ junction built-in voltage (around 1.4-1.5 V - 70-75 kV/cm), thermal effects [156], current leakage from the pumped section or bleaching due to high photogenerated carrier densities [157]. Moreover, as theoretically predicted in [66] and also observed in [156], the $C1 - HH1$ exciton disappears more easily, compared to the $C1 - LH1$ one, with any of the aforementioned factors. Figure 4.10 also shows the wavelength shift of 20 nm of the TE absorption edge obtained with a reverse voltage of 5.5 V (265 kV/cm), due to the quantum confined Stark effect [158].

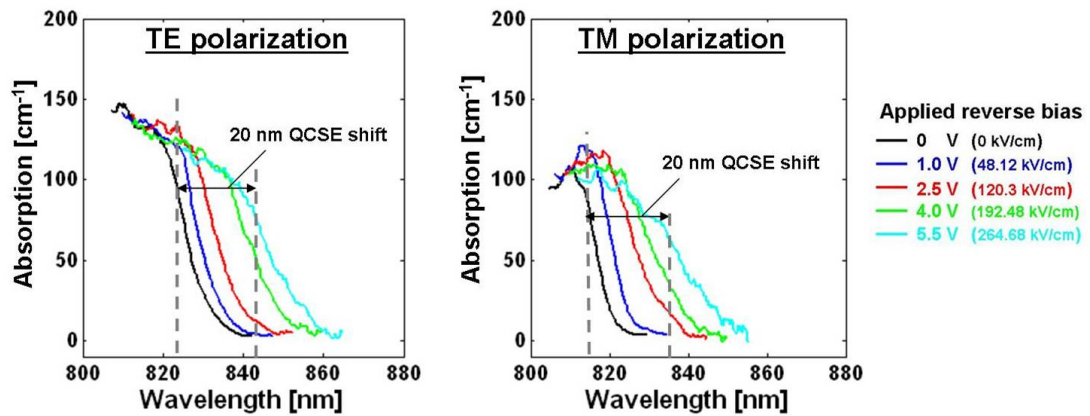


FIGURE 4.10: TE and TM absorption spectra for different reverse bias voltages. A wavelength shift of 20 nm of the TE and TM absorption spectra is obtained with a reverse voltage of 5.5 V (over a 208 nm thick intrinsic region this gives an electric field of 265 kV/cm), due to the quantum confined Stark effect [158]. The absorption edge is measured as the wavelength at which the derivative $d\alpha/d\lambda$ is maximum.

The gain and absorption spectra reported in this section, as already mentioned, will be

used in next chapter to explain some particular operational aspects of the fabricated ML lasers. However, it is opportune here to show that the recorded gain and absorption spectra can be used to accurately predict the threshold current of simple RWLs. For this purpose, the plot of the modal gain peak as function of current density has been considered, as shown in Figure 4.11(left). Figure 4.11(left) also shows the curve modeled using Equation 4.1 and $g_{0m} = 37.3 \text{ cm}^{-1}$ and $J_0 = 2177 \text{ A/cm}^2$, as obtained from RWL data reported in previous section.

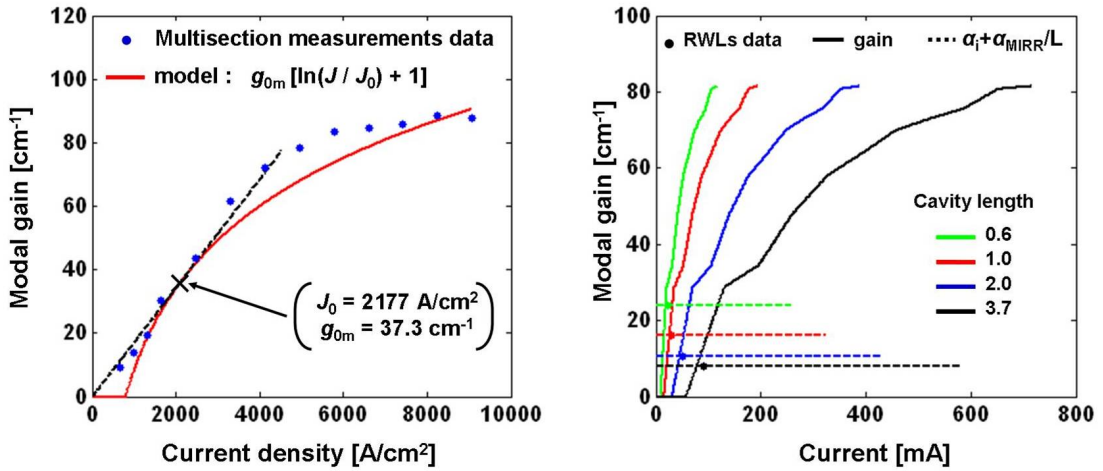


FIGURE 4.11: (left) Modal gain peak versus current density obtained from the multi-section measurements. The red line represents the curve modeled using Equation 4.1 and $g_{0m} = 37.3 \text{ cm}^{-1}$ and $J_0 = 2177 \text{ A/cm}^2$, obtained from the RWL data reported in the previous Section. The black dashed line gives the extraction of the parameters g_{0m} and J_0 . At current densities higher than around 3 kA/cm^2 , the data points and the red curve do not exactly match, due to the jump of the gain peak to the $C1-LH1$ transition. (right) Plot of the modal gain (obtained from the multi-section measurements) versus current, for cavity lengths of 0.6, 1, 2 and 3.7 mm. The dashed horizontal lines indicate the total losses for each cavity length and the dots represent the threshold points for each cavity length, as obtained from RWLs reported in previous Section.

Figure 4.11(right) gives the plot of the modal gain (obtained from the multi-section measurements) versus current, for cavity lengths of 0.6, 1, 2 and 3.7 mm. The dashed horizontal lines indicate the total losses (using $\alpha_i = 4.9 \text{ cm}^{-1}$ as obtained from the multi-section measurements) for each cavity length and cross the relative modal gain curves at the laser threshold point. The dots represent the threshold points for each cavity length, as obtained from RWLs data reported in the previous section. As can be seen from Figures 4.11(left) and (right), the RWLs data are in good agreement with the data obtained with the multi-section measurements.

4.4 Ridge waveguide lasers with non-absorbing mirrors

The developed SID QWI technique described in the previous chapter was used to fabricate ridge waveguide lasers with NAMs. As already explained, NAMs improve the COMD limit in the output power. Figure 4.12 shows SEM pictures of facets of some of the tested lasers, damaged by COMD. For the devices fabricated in this work, COMD powers of 40-50 mW (13.33-16.55 MW/cm²) were typically measured. In order to assess

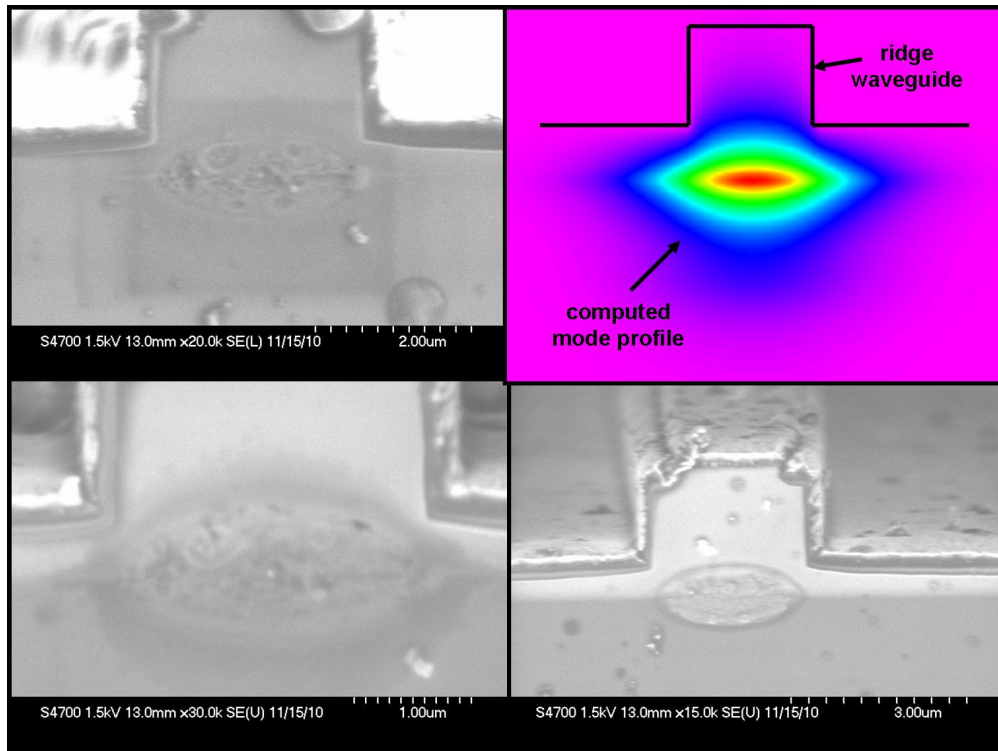


FIGURE 4.12: SEM pictures of a laser facet destroyed by COMD. The facet damage appears as a localized melted area with an elliptical profile. The top right picture is a plot of the computed mode profile for the laser cross section, showing good agreement with the elliptical profile of the COMD effect.

the quality of the developed QWI technique (described in Chapter 3) and also determine the effect of the NAM length on the laser performance, several 2 mm long lasers were fabricated with NAMs on both facets, with NAM section lengths from 0 to 300 μm in steps of 50 μm . Figure 4.13 shows the measured LIs of the best device for each NAM length, while Figures 4.14(top-left), (top-right), (bottom-left) and (bottom-right) are the plots of, respectively, threshold current, slope efficiency, threshold current density and maximum output power (in the 0-500 mA range) as function of the NAM section length. In these plots, the blue dots are the data extracted from the measurements reported in Figure 4.13, while the red lines are the corresponding modeled values. The modeled

values for threshold current I_{th} and threshold current density J_{th} were calculated using

$$J_{th} = J_0 \exp \left[\frac{\alpha_i L + \alpha_{MIRR} L}{g_{0m}(L - 2L_{NAM})} - 1 \right], \quad (4.7)$$

with $\alpha_i = 4.9 \text{ cm}^{-1}$, $\alpha_{MIRR} = 1.139 \text{ cm}^{-1}$, $J_0 = 2177 \text{ A/cm}^2$ and $g_{0m} = 37.3 \text{ cm}^{-1}$, while the slope efficiency was calculated as

$$\eta_{s(NAM)} = \eta_{s(no-NAM)} \left(1 - \frac{2L_{NAM}}{L} \right) \quad (4.8)$$

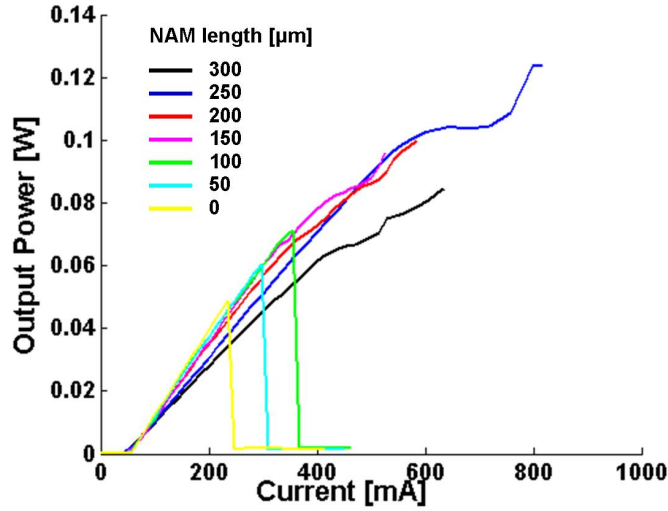


FIGURE 4.13: Measured LIs of lasers with different NAM lengths.

From Figures 4.13 and 4.14 one can firstly note that NAMs long at least $150 \mu\text{m}$ are enough to suppress COMD at output powers higher than 100 mW (the maximum measured was 124 mW for $250 \mu\text{m}$ long NAMs). However, the slope efficiency reduces when increasing the NAM length. This effect becomes particularly strong with NAMs longer than $250 \mu\text{m}$, at least for this cavity length, with a corresponding significant decrease in the output power. Moreover, while the total cavity losses remain the same, the presence of the NAMs reduces the gain section length and thus a higher gain is required to reach threshold. This produces an increase in the threshold current density, although the threshold current slightly decreases. As will be seen in Chapter 5, a higher threshold gain is an advantageous condition for the mode locking operation of semiconductor lasers. Furthermore, the increased threshold current density also determines a reduced dg/dN , which is also advantageous for making the gain section saturation energy higher than the SA one, as expressed in the Equation 2.18.

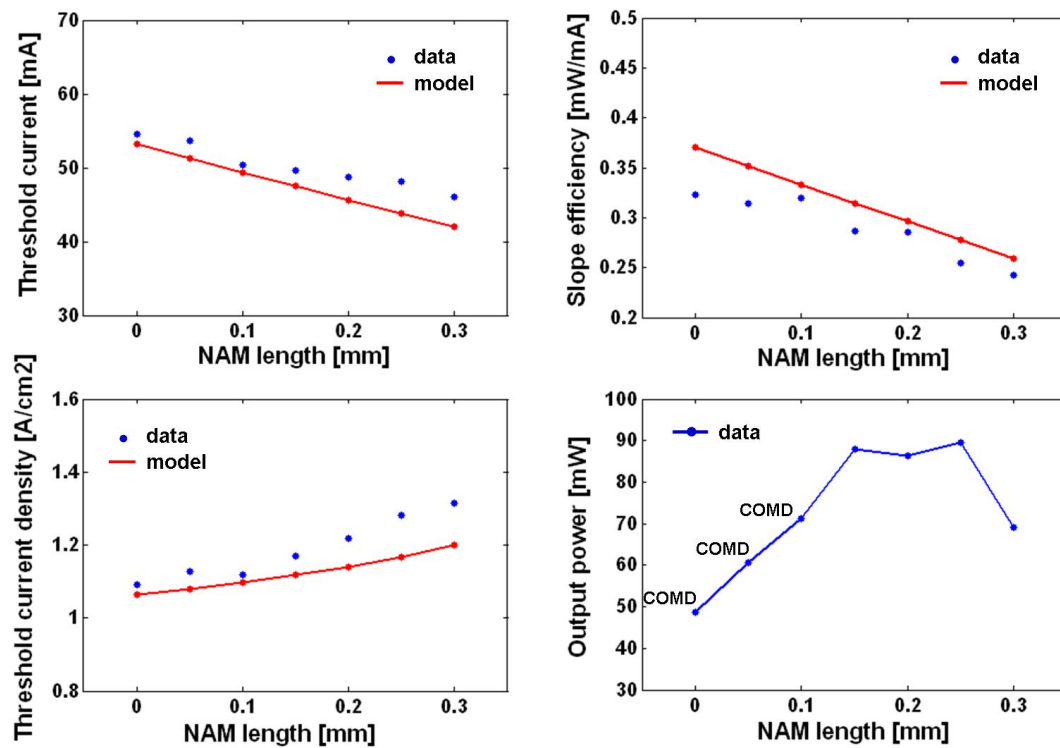


FIGURE 4.14: Plots of (top-left) threshold current, (top-right) slope efficiency, (bottom-left) threshold current density and (bottom-right) maximum output power (in the 0-500 mA range) as function of the NAM section length. In the (top-left), (top-right) and (bottom-left) plots, the blue dots are the data extracted from the measurements reported in Figure 4.13, while the red lines are the corresponding modeled values obtained using Equations 4.7 and 4.8. The modeled values are slightly better than the measured ones, probably due to the lateral grading of the QWI. In the (bottom-right) plot only the measured data are reported and are indicated with blue points. The measured maximum output powers are the COMD values for the devices where COMD occurred below 500mA, while these are the values at 500mA for devices where no COMD was observed in the 0-500 mA range. In this plot, one can also see that 150 μm long NAMs are enough to suppress COMD.

4.5 Ridge waveguide lasers with protective coatings for facet passivation

As already mentioned in Chapter 2, a method for protecting the laser facets from oxidation and thus from COMD is the use of coatings [76, 159]. In this work a test was done to assess the improvement in COMD power achievable with protective coatings. For this purpose, a bar with 2 mm long lasers was sent to Compound Semiconductor Technologies Ltd for being processed. The requirement was for coatings with 30% reflectivity at 830 nm and passivation. The layers deposited on both facets after Argon facet conditioning (Ar ablation) were Si (2 nm), SiO₂ (86 nm), Ta₂O₅ (100 nm) and SiO₂ (209 nm) and were designed and deposited by Compound Semiconductor Technologies Ltd. In this process, the Ar conditioning provides the removal of surface conductive states resulting

from dangling bond imperfections, the removal of any surface oxides already present and the occupation of states prone to oxidation. The thin Si layer acts instead as a diffusion barrier, preventing oxygen incorporation from the atmosphere, oxygen diffusion toward the surface of the crystal from the facet coating, and diffusion of atoms in the crystal outward into the facet coating [159]. The $\text{SiO}_2\text{-Ta}_2\text{O}_5\text{-SiO}_2$ dielectric sequence provides the desired reflectivity of the facets. The reason for the 30% reflectivity is that most of the ML lasers considered in this work had CPM configurations. The CPM geometry is not particularly suitable with unbalanced reflectivities between the two facets, as it does not help to have the maximum interaction between the two pulses circulating in the cavity in opposite directions and colliding in the SA. The LIs of coated and uncoated lasers are plotted in Figure 4.15. As shown, in the device with coatings, an increase higher than 100% is achieved in the COMD power limit, with a maximum value of 115 mW. No increase in threshold current or decrease in slope efficiency is observed, although the LI curve is less linear in the devices with coatings.

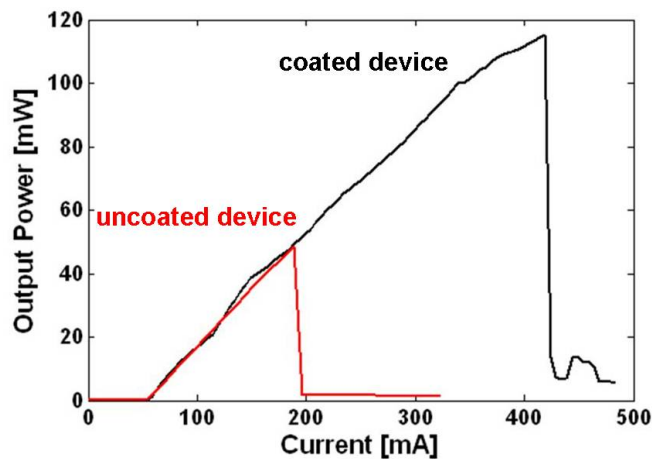


FIGURE 4.15: LI curves in 2 mm long ridge waveguide lasers with and without protective coatings on both facets. Both devices are without NAMs.

The coated bar contained ML devices that, however, did not show any ML operation as well as the uncoated ones and for this reason it was not possible to compare the two devices in terms of output power performance in ML regime. However, as it will be seen in Chapter 5, the limiting factor on ML output power in our devices is not COMD. Therefore, the benefits of protective facet coatings were not exploited in our ML devices.

4.6 Approaches for the characterization of mode locked lasers

Passively mode locked lasers are ridge waveguide lasers with typically one gain section forward biased and at least one SA section reverse biased. Therefore, the set-up used for characterizing these devices included a laser driver for providing the gain section current and a power supply for providing the SA section reverse voltage. The gain current or the SA voltage were applied to the devices using probes moved with three-axis micro-positioners. The devices were usually cleaved in the form of bars containing several ML lasers. Each laser bar was glued on brass sub-mounts with silver paste, in order to provide mechanical support to the devices. The sub-mounts were then screwed on a stage with a thermo-electric cooler (TEC) and a thermo-conductive paste was used to improve the thermal conductivity between the lasers and the heat sink. Typically, the lasers were operated at a constant temperature of 20°C using the TEC controller module of the laser driver. Figure 4.16(left) shows some laser bars mounted on brass sub-mounts, while Figure 4.16(right) shows the three-axes movable stage where the mounted laser bars were placed for testing.

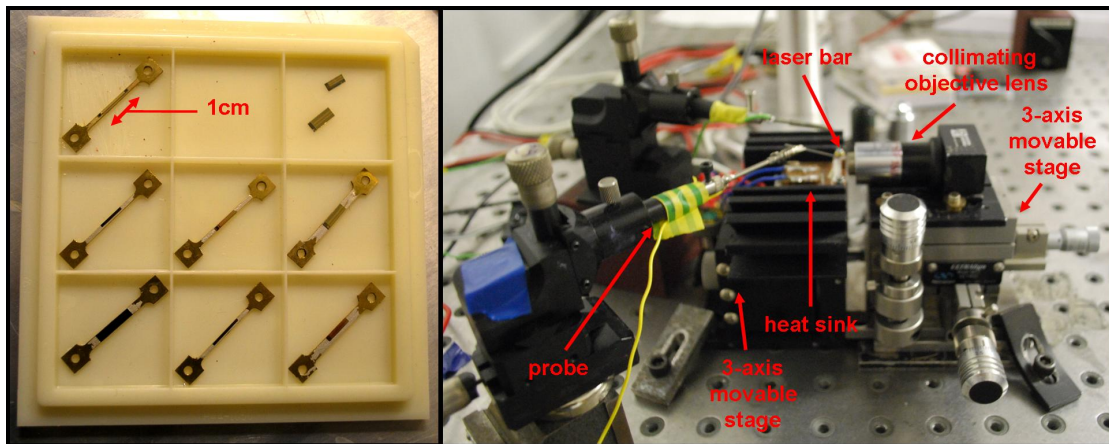


FIGURE 4.16: (left) Photograph of laser bars mounted on a brass sub-mounts. (right) Three-axes movable stage where the mounted laser bars were placed for testing.

The full characterization of the ML devices usually included four main steps. In some of these steps, the measurements were carried out using LABVIEW codes for automated remote control. This was necessary when the measurement had to be iterated several times, like, for example, when scanning the gain current and/or the SA voltage.

The first characterization step was the measurement of the LI curves using a Thorlabs PM100D power meter with a S142C optical power sensor. These measurements were carried out free-space, placing the sensor as close as possible to the laser facet. Typically, VI curves were recorded simultaneously to the LIs. LIs and VIs were used to evaluate

basic laser performance parameters like threshold current, slope efficiency, maximum power (eventually limited by COMD or thermal roll-over), built-in voltage and contact resistance. According to the needs, LIs were recorded by forward biasing both gain and SA sections or by reverse biasing the SA. In some cases, simultaneously to the LIs, the SA photo-current was also recorded. This was necessary in order to monitor the SA current and avoid the damage of the SA itself.

The second step was usually the measurement of the optical spectrum, typically mapped as function of the gain section current and SA reverse voltage. This was carried out by coupling the laser output through a single mode fiber provided with a lensed input, into an optical spectrum analyzer (OSA) (Agilent 86140B). The optical spectrum was useful mainly to evaluate peak wavelength and optical bandwidth of the laser output. Moreover, in most cases, the optical spectrum also revealed the gain current and SA voltage range of mode locking. This because the typical optical spectrum of a laser in ML operation has some peculiarities compared to that shown in CW operation. The spectrum broadens in ML regime because several longitudinal modes contribute to the laser output. Usually, a decrease in the peak power is also observed, as the average power is shared by several modes, differently from the CW regime where one single mode is lasing (or few modes are lasing but not in phase). Furthermore, in colliding pulse ML devices as well as in higher harmonic configurations, some modes are suppressed and some are enhanced in ML regime, according to the particular harmonic being selected. Therefore, the measurement of the longitudinal mode spacing was used as a preliminary way of assessing harmonic mode locking operation. However, the resolution bandwidth of the OSAs under use was 0.06-0.07 nm, which prevented an accurate mode spacing measurement, particularly for long devices (more than 2 mm) whose fundamental cavity mode spacing was smaller than 0.04-0.05 nm. Figures 4.17(left) and (right) show examples of optical spectra measured from a fabricated 0.6 mm long CPM laser, in CW operation and ML regime, respectively.

A further confirmation of the mode locking operation was obtained by measuring the RF spectrum, also mapped as function of the gain section current and SA reverse voltage. This was carried out by coupling the laser output through a single mode fiber provided with a lensed input, into an RF detector (Picometrix PX-D7, 400-900 nm) connected to an RF spectrum analyzer (Hewlett Packard 8564E). The RF detector under use had a maximum bandwidth of 60 GHz, while for the RF spectrum analyzer this was 40 GHz. This means that only for devices operating with pulse repetition rates smaller than 40 GHz, the RF spectrum was recorded, in order to evaluate RF peak amplitude, frequency and line-width. Typically, good ML operation was observed with RF peaks higher than 20 dB over the noise floor and line-widths below 250 kHz at the frequency corresponding to the designed repetition rate. In some cases, as will be explained in next chapter, for

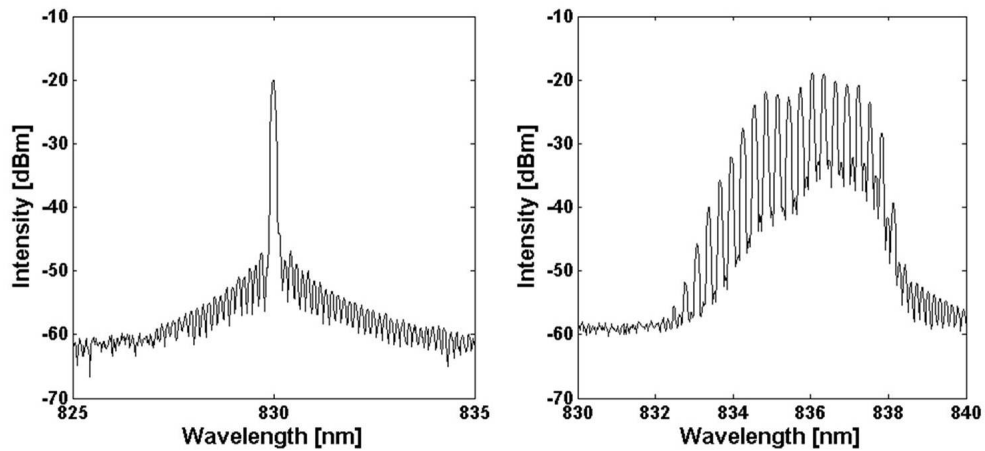


FIGURE 4.17: Examples of optical spectra measured from a fabricated 0.6 mm long CPM laser, in CW operation (left) and CPM regime (right). The FP cavity mode spacing is around 0.15 nm and corresponds to the mode spacing in CW (although one mode only is lasing), while in CPM regime the mode spacing doubles and becomes around 0.3 nm.

some values of the gain current and SA voltage, some peaks in the 0-5 GHz range were observed, suggesting the occurrence of relaxation oscillations self-pulsating (SP) regimes. Figures 4.18(left) and (right) show examples of RF spectra measured from a fabricated 3.7 mm long CPM laser, in SP operation at around 1 GHz and CPM regime at around 19.5 GHz, respectively. In the former case, the 1st harmonic of the CPM peak is also visible at around 39 GHz.

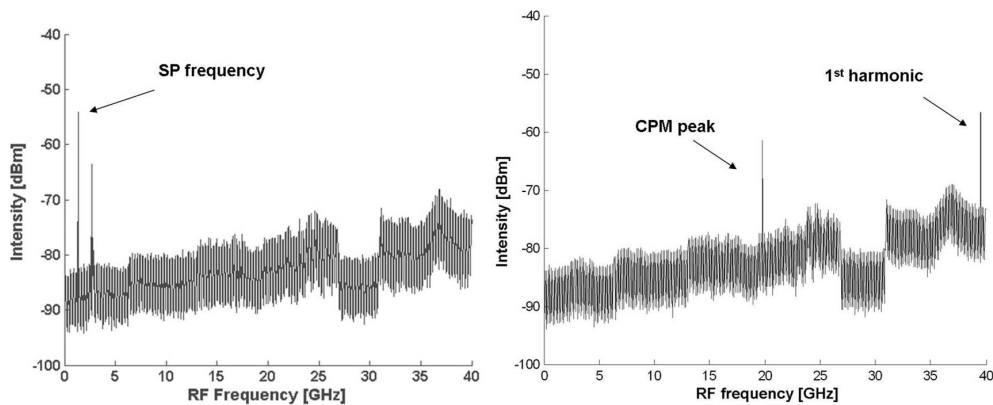


FIGURE 4.18: Examples of RF spectra measured from a fabricated 3.7 mm long CPM laser, in (left) Q-switched self-pulsating operation at around 1 GHz and (right) CPM regime at around 19.5 GHz. The 1st harmonic of the CPM peak is also visible at around 39 GHz.

The last characterization step was the measurement of the laser output in the time domain, in order to further proof the emission of pulses at the desired repetition rate and also to estimate pulse duration and peak power. As this characterization stage

required a significant work for developing the measurement technique and building a dedicated set-up, a more detailed description will be given in the next sections.

4.6.1 Autocorrelation measurements

Several methods have been proposed in literature for the characterization of ultrafast optical pulses, using ultrafast photo-detectors and fast sampling oscilloscopes, for signals modulated at up to tens of GHz, or electron-optical streak cameras which have limited resolution (around 2 ps) and poor sensitivity [30]. Other more powerful techniques make use of interferometer configurations, to split in two the laser beam and then recombine the two after introducing a path length difference. This allows to indirectly deduce the pulse information by analyzing the recorded recombined beams. This autocorrelation technique was chosen for our work, because it is relatively easy to implement and, if carried out properly, is not limited in time resolution and sensitivity. The typical set-up for autocorrelation measurements, as shown in Figure 4.19, includes a Michelson interferometer. This splits the collimated laser output in two beams with a beam splitter and recombines them after each beam has been reflected by a corner mirror. Before the recombination, one of the beams is delayed compared to the other, using a movable stage that controls the mirror position along the beam propagation direction. The signal at the output of the interferometer is then focused into a photodetector. The photocurrent of the detector is recorded by a lock-in amplifier, triggered at the same frequency (typically around 280 Hz) of the chopper placed between the laser and the interferometer.

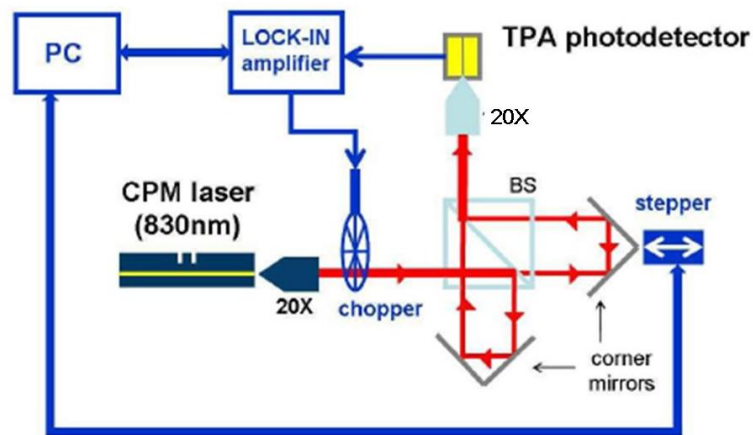


FIGURE 4.19: Schematic of an autocorrelation measurement set-up.

When a laser pulse with a field envelope $E_0(t)$, slowly-varying with respect to the optical frequency ω , is split in two pulses of the same amplitude and delayed of τ in the

interferometer, the real field of the pulses can be represented as

$$E_1(t) = \frac{E_0(t)}{\sqrt{2}} \exp(i\omega t) \quad (4.9)$$

and

$$E_2(t) = \frac{E_0(t + \tau)}{\sqrt{2}} \exp[i\omega(t + \tau)]. \quad (4.10)$$

The instantaneous signal intensity of the recombined beam is given by

$$I(t, \tau) = c\epsilon_0 \langle [E_1(t) + E_2(t)]^2 \rangle_{time} \cong \frac{c\epsilon_0}{4} [E_1(t) + E_2(t)]^2 \quad (4.11)$$

where c is the light speed and ϵ_0 the vacuum electric permittivity. In our case, the detector response is slower than the time delay τ , therefore the recorded photo-current $J_1(\tau)$ can be written as

$$J(\tau) \propto \int_{-\infty}^{+\infty} I(t, \tau) dt \propto WG_1(\tau) \quad (4.12)$$

where W is the pulse energy given by

$$W = \int_{-\infty}^{+\infty} E_0^2(t) dt \quad (4.13)$$

and G_1 is the autocorrelation function. This can have different expressions according to the speed and non-linearity of the detector response. For a linearly responding detector, G_1 is the linear (field) autocorrelation, given by

$$G_1(\tau) = 1 + \frac{\int_{-\infty}^{+\infty} E_0(t)E_0(t + \tau) dt}{\int_{-\infty}^{+\infty} E_0^2(t) dt}. \quad (4.14)$$

The linear autocorrelation, related to the power spectral density through the Fourier Transform, does not contain any phase information and cannot be used for measuring the pulse-width, but only for evaluating the coherence time of a laser output [160–162]. If the detector has a non-linear response, the photo-current is given by

$$J_2(\tau) \propto \int_{-\infty}^{+\infty} I^2(t, \tau) dt \propto \int_{-\infty}^{+\infty} [|E(t) + E(t + \tau)|^2]^2 dt \propto WG_2(\tau), \quad (4.15)$$

where G_2 corresponds to the non-linear autocorrelation (of the second order in this case). If the experimental set-up is not fast enough to sense the fast-varying interferometric fringes, the measurement system is called intensity autocorrelation. In this case G_2 is

given by

$$G_2(\tau) = 1 + 2 \frac{\int_{-\infty}^{+\infty} E^2(t)E^2(t + \tau)dt}{\int_{-\infty}^{+\infty} E^4(t)dt} = 1 + 2 \frac{\int_{-\infty}^{+\infty} I(t)I(t + \tau)dt}{\int_{-\infty}^{+\infty} I^2(t)dt}. \quad (4.16)$$

This situation can also be obtained with an interferometer which combines two cross-polarized beams. If the used detector is fast and sensitive enough to resolve the interference pattern generated by the two beams (i.e. the resolution is 1/10 of the wavelength) [163], the autocorrelation is called interferometric autocorrelation and G_2 (indicated as g_2) is given by

$$g_2(\tau) = 1 + \frac{2 \int_{-\infty}^{+\infty} E^3(t)E(t + \tau)dt + 2 \int_{-\infty}^{+\infty} E(t)E^3(t + \tau)dt + 3 \int_{-\infty}^{+\infty} E^2(t)E^2(t + \tau)dt}{\int_{-\infty}^{+\infty} E^4(t)dt}. \quad (4.17)$$

In this case, as in the linear autocorrelation, the two recombined beams are collinear. In the linear autocorrelation the contrast ratio (signal-to-background ratio) between the maximum of G (at zero delay) and its minimum (at time delays where no overlap occurs between pulses) is 2:1 for the output of a mode-locked laser. With a non-linear photoresponse, the intensity autocorrelation trace has a signal-to-background ratio of 3:1 in the case of mode-locked beam and of 3:2 for the non mode-locked one, while the interferometric one has ratios of 8:1 or 2:1, respectively. The electric field temporal profile of a pulse is plotted in Figure 4.20 (top-left), while the corresponding computed intensity, interferometric and linear autocorrelation functions are shown in Figures 4.20(top-right), (bottom-left) and (bottom-right), respectively.

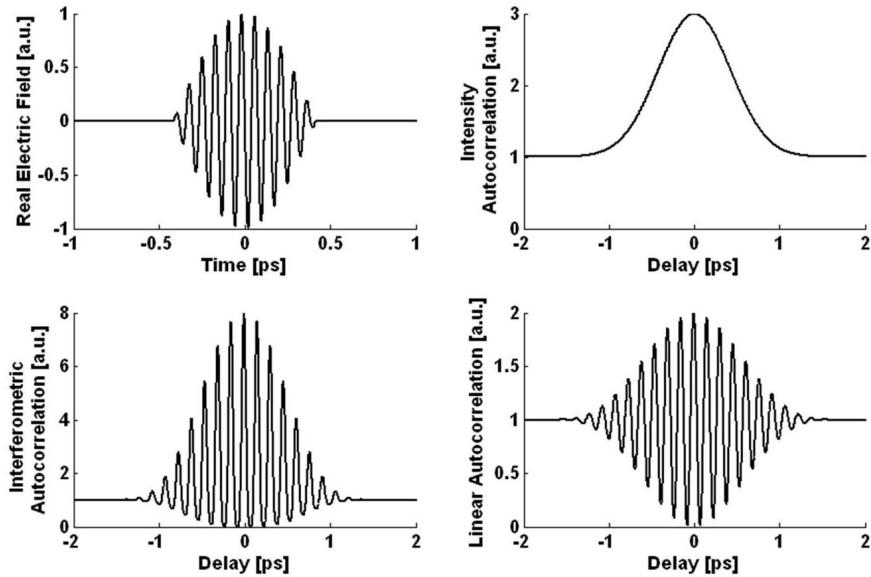


FIGURE 4.20: Temporal profile of the electric field (top-left) and correspondent intensity (top-right), interferometric (bottom-right) and linear (bottom-left) autocorrelation traces.

Beside the higher difference in the signal-to-background ratio, it should be noted that only an interferometric autocorrelator can distinguish between chirped and unchirped pulses. For this reason, it is also the only autocorrelation method capable of giving an indirect estimation of the pulse-width. There exist a number of definitions for key characteristics of short pulses [164], therefore it is important to adopt a single standard for assessing pulse-width, both in the time and spectrum domains. Most commonly, the pulse duration τ_p is defined as the full width at half-maximum (FWHM) of the intensity profile, while the spectral width $\Delta\nu$ (bandwidth) is defined as the FWHM of the spectral intensity. Because of the difficulty in asserting an exact pulse shape, standard waveforms have been selected as best approximations. Relations for expressing the normalized profiles of the two most common pulse shapes, both in frequency and time domains, are reported in Table 4.2 [164].

$I(t)$ (temporal intensity profile)	$I(\omega)$ (spectral intensity profile)	$G_1(\tau)$ (linear autocorrelation)	$G_2(\tau)$ (intensity autocorrelation)	$g_2(\tau)$ (interferometric autocorrelation)	$\Delta\tau_G/\tau_p$	TBP
<u>GAUSSIAN</u> $\exp(-t^2)$	$\exp(-\omega^2)$	$1 + \exp(-\tau^2/4)$	$\exp(-\tau^2/2)$	$1 + 3 G_2(\tau) \pm 4 \exp(-3\tau^2/8)$	1.414	0.441
<u>Hyperbolic secant</u> $\text{sech}^2 t$	$\text{sech}^2(\pi\omega/2)$	$1 \pm \tau/\sinh\tau$	$3 (\tau \cosh\tau - \sinh\tau) / \sinh^3\tau$	$1 + 3 G_2(\tau) \pm 3 (\sinh 2\tau - 2\tau) / \sinh^3\tau$	1.543	0.315

TABLE 4.2: Expressions for temporal $I(t)$ and spectral $I(\omega)$ intensity profiles for a Gaussian (second row) and *sech* (third row) field envelope pulse profiles. The expressions for the linear $G_1(\tau)$, intensity $G_2(\tau)$ and interferometric $g_2(\tau)$ autocorrelation functions are also reported. The relative conversion factors between the interferometric autocorrelation FWHM $\Delta\tau_G$ and the pulse-width τ_p are indicated in the second-last column. The TBP is reported in the last column [164].

The pulse duration can be obtained by first assuming a shape of the ones reported in Table 4.2 for the measured pulse. This is done by searching for the shape with the spectral profile best fitting to the envelope of the laser optical spectrum. Once the best-fitting pulse shape is found, the pulse-width can be determined by deconvolving the measured autocorrelation trace with this assumed pulse shape. In practical cases, the specific conversion factors shown in Table 4.2 are used to calculate the pulse-width from the width $\Delta\tau_G$ of the envelope of the autocorrelation trace. The obtained pulse-width is then multiplied by the optical bandwidth (width of the best fitting envelope of the optical spectrum) to calculate the so-called time-bandwidth product (TBP).

As the temporal and spectral characteristics of the electromagnetic field are related via Fourier transforms, pulse bandwidth $\Delta\nu_p$ and duration τ_p cannot vary independently of each other. This fact is formulated by the Uncertainty Principle, which states that there is a minimum time-bandwidth product (TBP):

$$\Delta\nu\Delta\tau \geq K \tag{4.18}$$

where K is a numerical constant of the order of unity, depending on the actual pulse shape. For the two examples of pulse shapes considered in Table 4.2, the corresponding minimum TBPs are also reported. The TBP of Equation 4.18 is equal to the pulse-specific constant K only for ideal pulses without frequency modulation (chirp), which are often called bandwidth-limited or transform-limited. Such pulses exhibit the shortest possible duration at a given spectral width and pulse shape. If there is a frequency variation across a pulse, its spectrum will contain additional frequency components. Consequently, such pulses will possess a spectral width larger than the Fourier limit given by Equation 4.18.

The pulse characterization procedure adopted for this project is fairly basic and involves the measurement of the bandwidth of the pulse from the optical spectrum and the measurement of the FWHM of the interferometric autocorrelation. In both cases, a Gaussian pulse shape was typically assumed as it gave the best fitting with the measured data.

4.6.2 Autocorrelation set-up

In this work, the method chosen for the temporal characterization of the output of the fabricated mode locked devices is the interferometric autocorrelation, for the previously mentioned reasons. A schematic of the set-up implemented was shown in Figure 4.19, while Figure 4.21 shows a photograph of the purpose-built set-up.

Several aspects needed particular attention during the development of the measurement system and will be here briefly discussed. The accurate alignment of all the optical elements of the set-up is very important, but for some of them this is critical. The beam splitter at the center of the interferometer is the first element to align as it dictates the directions of the input and output beams of the interferometer itself. For this element, a particular holder was used, allowing the control of the angle position in the three axes. Therefore, one needs the accurate positioning of beam splitter and laser source, in order to ensure that the perfect perpendicularity of laser beam to the beam splitter input facet. At this point, both the laser stage and the stage holding the collimating objective lens need to be controlled. Moreover, for the two mirrors of the interferometer, it is opportune to use corner reflectors (shown in Figures 4.19 and 4.21) instead of flat ones, in order to have the incident and reflected beams with parallel directions. This introduces two main benefits to the alignment procedure. The first is that the incident and reflected beams are separated in space and it is easier to check their position using an infrared card. The second benefit is that the angle position of the mirrors does not affect the system alignment and one needs to optimize only their position in the plane perpendicular to

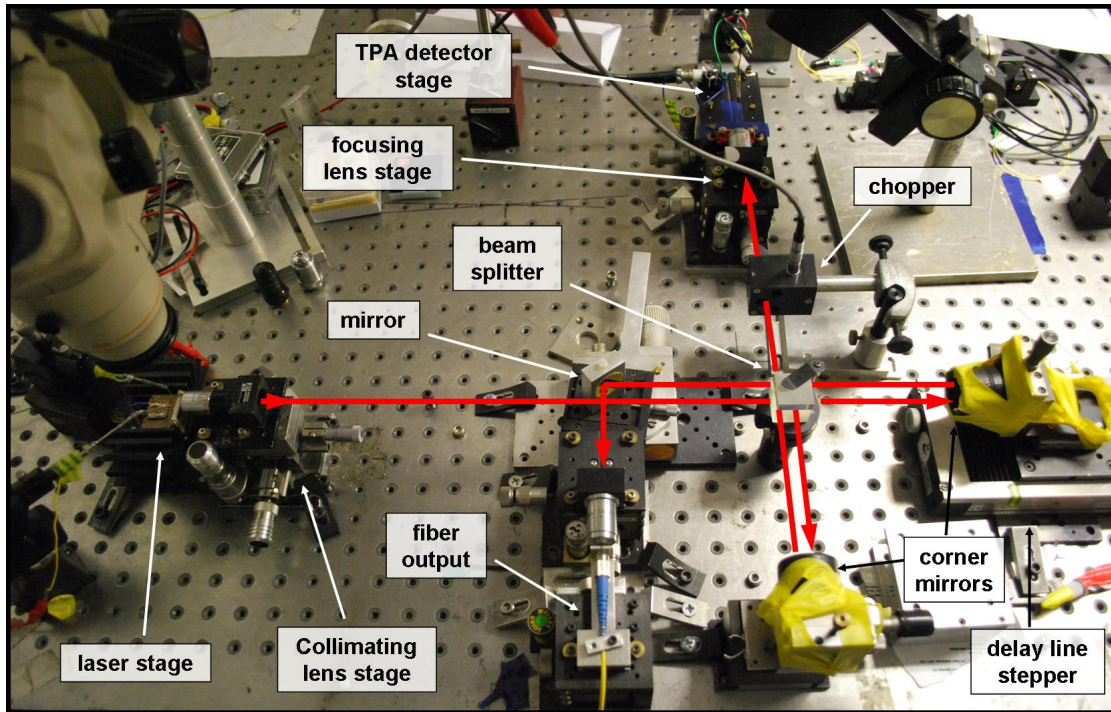


FIGURE 4.21: Photograph of the purpose-built TPA interferometric autocorrelation measurement set-up. The laser beam is collimated using an objective lens (placed on a 3-axes positioner) and then split in two and recombined by a non-polarizing beam splitter (placed on a 3-axes angle positioner). A corner mirror is introduced in each arm of the interferometer to reflect in opposite direction the beams coming from the beam splitter. Each corner mirror is placed on a 2-axes positioner, but only one is movable along the beam direction via remote computer control, to form the interferometer delay line. One output of the interferometer is injected in a fiber using a gold mirror, for on-line monitoring of the laser spectrum. The second output is chopped and focused into the TPA detector (placed on a 3-axes positioner) using an objective lens (placed on a 3-axes positioner).

the beam direction (vertical and horizontal). The third element to align is the objective lens at the output of the interferometer. The lens optical axis must be exactly in the direction of the two output beams, in order to maintain their direction of propagation. Once this is achieved, the detector can be placed on its movable stage, behind the lens. Its position along the three axes needs to be optimized in order to have the lens focus exactly on the detector facet. At this purpose, the detector can be forward biased and the emitted beam collimated (only moving the detector). The detector collimated beam can thus be used as input beam of the interferometer, for a rough alignment. Once, by eye, the laser beams look positioned at the center of the lens close to the detector and the light emitted by the forward biased detector looks positioned at the center of the lens close to the laser source, the alignment can be refined maximizing the lock-in amplifier signal.

Some problems in the implemented measurements were introduced by the non-ideal splitting ratio of the beam splitter, which should be in theory 50:50. In our case, a

ratio of around 55:45 was measured with a resulting reduced signal-to-background ratio in the recorded autocorrelation traces. In most cases this problem was overcome by either reducing the power in the stronger beam of the interferometer, using a neutral density filter, or by slightly misaligning the stronger beam. Another difficulty was due to the poor resolution of the autocorrelator delay line, limited to steps not shorter than $1 \mu\text{m}$, with a correspondent delay step of 6.67 fs. This limit prevented the possibility to completely resolve the interferometric fringes, but allowed for a relatively accurate evaluation of the autocorrelation trace envelope, necessary for the pulse-width indirect estimation.

4.6.3 Two photon absorption detectors

The first photodiodes considered in the set-up were some commercial red lasers emitting at wavelengths ranging from 650 to 750 nm. It has been shown [30] that such devices can be suitable for giving two photon absorption (TPA) of light beams at wavelengths higher than 800 nm. This means that a red-laser can give a second-order response if used for detecting light at 830 nm, our wavelength of interest. In this case, the detector photo-current can be expressed as [30]

$$J = J_1(P) + J_2(P) + C \approx \alpha P + \beta P^2 + C \quad (4.19)$$

where P is the detector input power (which in the experiment substitutes the intensity [30]), J_1 and J_2 are, respectively, the linear and the non-linear contributions of the detector photo-response and C is the detector dark-current (background contribution). The non-linearity of the detector can be evaluated by the ratio between J_2 and J_1^2 , expressed by the non-linearity factor $\gamma = \beta/\alpha^2$. This gives an useful estimation of the suitability of the detector for TPA autocorrelation [30, 165].

Unfortunately, most of the red-lasers used for our purposes showed poor or no non-linear response and most of the recorded autocorrelation traces were linear, with a clear symmetry between the higher and lower envelopes, as shown in Figure 4.22. However, for some red lasers, TPA detection was achieved but with several difficulties. One main disadvantage of commercial lasers is their packaging, i.e. because a protective glass is often placed in front of their output facet. This prevents the positioning of the objective lens at the output of the interferometer, close enough to the device facet. This often resulted in an incomplete focusing of the beam into the detector. Moreover, for commercial devices it is not possible to know their waveguide geometry and dimensions. This is disadvantageous because, for achieving a TPA response, small waveguides are preferred.

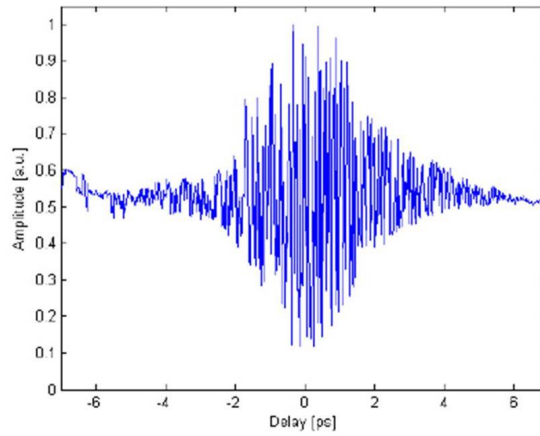


FIGURE 4.22: Linear autocorrelation trace measured with a Michelson interferometer with a delay line and a red laser used as photodetector.

The non-linear response measured for the 651 nm commercial laser (Toshiba TOLD 9442M) used as TPA detector is shown in Figure 4.23. In the horizontal axis of Figure 4.23, the average laser power (recorded at the output of the collimating lens) is plotted. This detector showed a small non-linear response range, being limited, for small powers, by linear contribution or noise and, at high powers, by the saturation of the photo-current. With these devices, non-linear autocorrelation traces could be measured only for laser output powers higher than 15 mW. For powers higher than 30 mW, a variable neutral density filter was used to decrease the power coupled into the detector and avoid its saturation. The measured γ was 2.628 in CW operation, similarly to what reported in [165]. Values of γ similar to the ones obtained in this work have been reported in [30]. With this detector, when the laser power was high enough to excite a non-

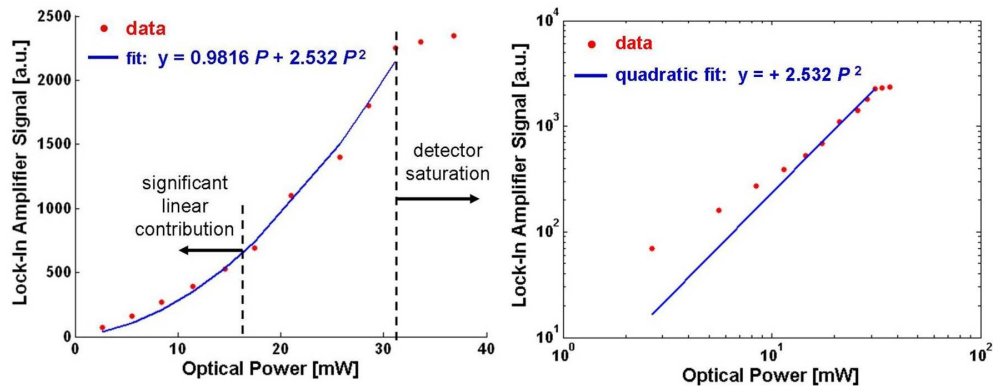


FIGURE 4.23: Non-linear response of the 651 nm commercial laser used as TPA photo-detector in (left) linear and (right) logarithmic scales. In the horizontal axis the average collimated laser output power is considered. The laser is operated in CW regime. This detector showed a small non-linear response range, being limited for small powers by the linear contribution and at high powers by the saturation of the photo-current. The measured γ is 2.628 in CW operation.

linear photo-response much higher (at least 1 order of magnitude) than its linear one,

a non-linear autocorrelation trace was directly acquired. However, when this was not possible, a quick measurement pre-calibration had to be performed immediately before each autocorrelation scan. This was necessary for evaluating the coefficients α and β in Equation 4.19 and eliminate the linear contribution αP from the recorded lock-in amplifier signal, as suggested in [165]. In the pre-calibration procedure, with the ML laser running at full power P_0 (whether ML or not) and the translation stage positioned at a delay in between correlation peaks, two detector readings, J_0 and J_1 , were taken at powers P_0 and $P_1 = P_0/2$ (obtained by placing a 50% filter in the beam), respectively. Assuming the dependence of Equation 4.19, the linear (αP) and quadratic (βP^2) terms can be easily found from the two points. The measured autocorrelation data J_k can then be modified by establishing the ratio J_k/J_0 from Equation 4.19 and correcting it for the linear term. The resulting data are, therefore, normalized to J_0 and approximate the autocorrelation trace that would be registered with a purely quadratic detector.

A wider non-linear response range and a higher γ were obtained with waveguide TPA detectors designed and fabricated for the purpose. The waveguide structure of the designed detector is shown in Figure 4.24. As can be seen, the input of the detector is

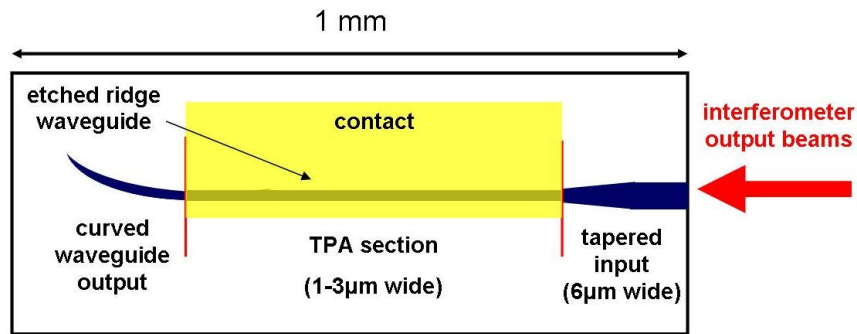


FIGURE 4.24: Top view illustration of the designed TPA photodetector.

tapered in order to simplify the detector alignment and improve the coupling of the laser beam into the detector. The detector waveguide width is then reduced in the detection region, in order to decrease the beam size and increase the optical intensity, being the TPA response stronger for higher intensities. The output of the detector is tapered down and curved, in order to avoid undesired back reflections and ensure single pass measurements. Figures 4.25(a), (b) and (c) show SEM and optical microscope images of the fabricated devices.

The designed material reported in Table 4.3 and used for fabricating these devices was grown by the EPSRC National Centre for III-V Technologies of the University of Sheffield. As can be seen from Table 4.3, the material has a bulk active region as it has been found to have better non-linear response compared to quantum well structures [166]. The Al mole fractions were chosen high enough to make the claddings and the

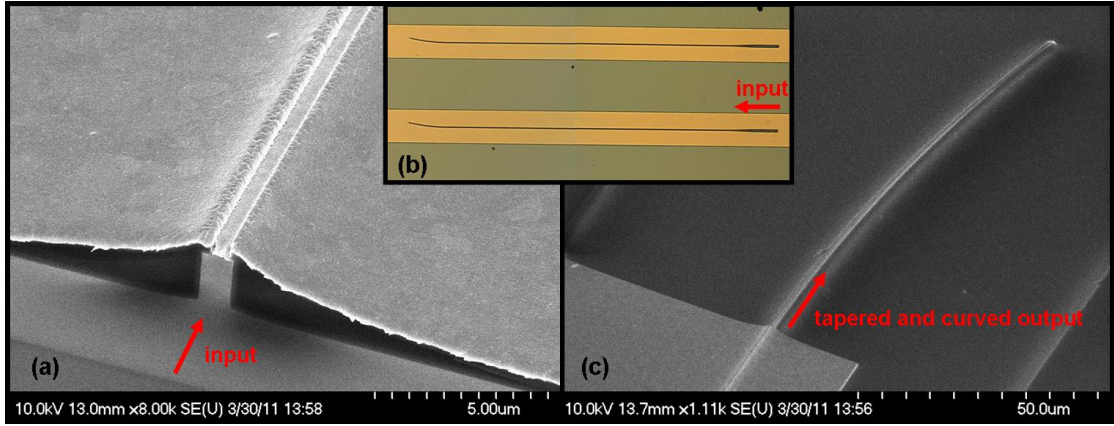


FIGURE 4.25: (a) SEM picture of the input facet of the fabricated TPA detector. (b) Optical microscope image of the top view of the TPA detectors, after the ridge waveguide etching pattern definition in the PMMA mask. (c) SEM image of the tapered and curved waveguide output of the TPA detector.

$\text{Al}_x\text{Ga}_{1-x}\text{As}$ layer	x [Al mole fraction]	thickness [um]	Doping [cm^{-3}]
cap (GaAs)	0	0.1	P++ : $3\text{E}19$
graded ($\text{Al}_x\text{Ga}_{1-x}\text{As}$)	0.45 \rightarrow 0	0.2	P+ : $5\text{E}17 \rightarrow 1\text{E}18$
P cladding ($\text{Al}_x\text{Ga}_{1-x}\text{As}$)	0.45	1.5	P : $5\text{E}17$
waveguide ($\text{Al}_x\text{Ga}_{1-x}\text{As}$)	0.25 \rightarrow 0.45	0.25	UD
Core ($\text{Al}_x\text{Ga}_{1-x}\text{As}$)	0.15	0.5	UD
waveguide ($\text{Al}_x\text{Ga}_{1-x}\text{As}$)	0.45 \rightarrow 0.25	0.25	UD
N cladding ($\text{Al}_x\text{Ga}_{1-x}\text{As}$)	0.45	2	N : $5\text{E}17$
graded ($\text{Al}_x\text{Ga}_{1-x}\text{As}$)	0 \rightarrow 0.45	0.3	N+ : $2\text{E}18 \rightarrow 5\text{E}17$
substrate (GaAs)	0	380	-

TABLE 4.3: Epilayer structure of the material designed for fabricating TPA photo-detectors.

graded index waveguide non-absorbing at 830 nm. The bandgap wavelength of the core was instead chosen to be 750 nm in order to stay away from the laser wavelength and minimize the linear absorption, but close enough to produce the maximum non-linear coefficient and thus the maximum signal-to-background ratio in the autocorrelation, as suggested in [167]. The measured response for these devices is reported in Figure 4.26. As can be seen from Figure 4.26, the fabricated devices have a stronger non-linear response compared to the red laser detectors previously described, with a value of γ of 4.9 in CW laser operation, similarly to what reported in [165]. In addition to the slightly improved sensitivity of the detector, no photocurrent saturation was observed within the power range considered, extending the range of TPA operation also towards higher powers. An easier alignment was also obtained thanks to the widened input waveguide geometry. However, the fabricated detector had to be probed, compared to the red laser

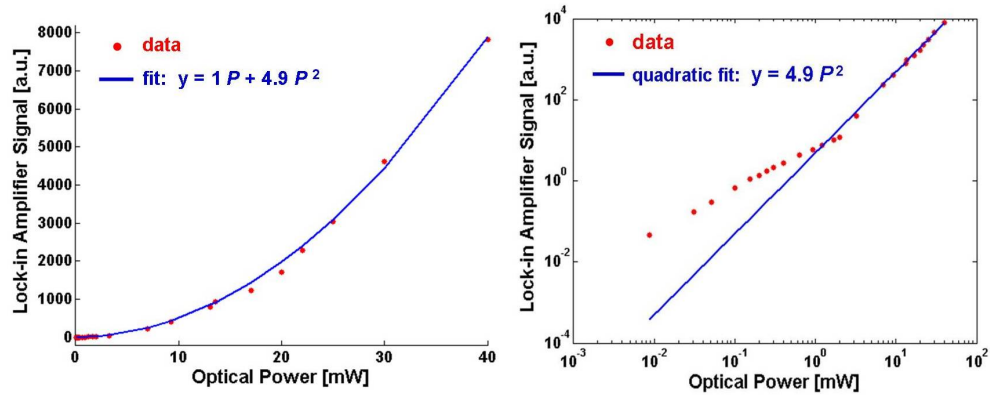


FIGURE 4.26: Non-linear response at 830 nm of the fabricated TPA photodetector in (left) linear and (right) logarithmic scales. In the horizontal axis the average collimated laser output power is considered. The laser is operated in CW regime. The measured γ is 4.9 in CW operation.

that could be biased with wires. The red laser was fixed within an Aluminum cage to shield it from electromagnetic noise, as shown in Figure 4.27(left). On the contrary, the need for the probe for the fabricated devices was disadvantageous during the alignment procedure, because the release of the probe was needed for moving the detector stage. To overcome this limit, the probe and its 3-axes positioner were fixed on the same movable stage of the detector, as shown in Figure 4.27(right).

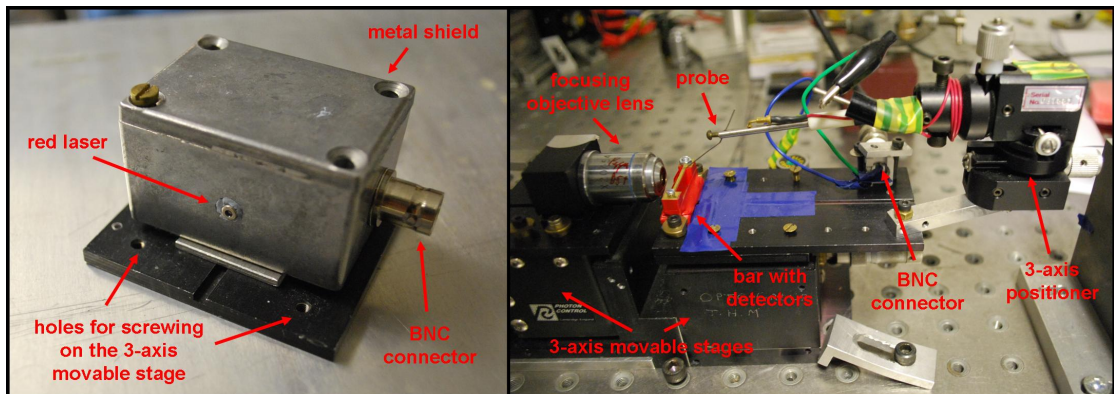


FIGURE 4.27: (left) Photograph of the purpose-built aluminum cage to shield the red laser used as TPA detector from electromagnetic noise. A BNC connector was also added to the cage for recording the detector signal. (right) Photograph of the 3-axes movable stage that moved the fabricated TPA detectors. On the same stage, the 3-axes positionable probe and a BNC connector were also fixed.

With both red lasers detectors and TPA waveguide devices, non-linear autocorrelation traces could be recorded. Examples of such traces will be shown in the next chapter, relatively to the characterization of the fabricated ML lasers.

4.7 Chapter summary

In this chapter, results from several kind of devices have been reported. Oxide stripe lasers and ridge waveguide lasers were fabricated and tested in order to evaluate some material parameters from the measured LI curves, like the infinity current density J_∞ , the cavity parameter L_0 , the optimum gain point g_0 , the intrinsic loss α_i and the injection efficiency η_{inj} . Reasonable agreement was obtained from the two set of measurements, but for ridge waveguide devices the value of g_0 was lower and the value of J_∞ higher. This is due to the higher waveguide losses of RWLs and to their increased junction heating associated with the DC testing conditions (OSLs were instead tested with pulsed currents). Multisection devices were also fabricated and tested in order to measure the TE and TM polarization gain and absorption spectra, under several forward and reverse biasing conditions. From these measurements, the electron-hole transitions of the material were estimated and compared to the values calculated in Appendix B. The values of the saturation parameters g_0 and J_0 measured from RWLs were also confirmed. These important material parameters were then used for evaluating the performance of more complex devices. In particular, a fairly accurate prediction of threshold current and slope efficiency of RWLs with non-absorbing mirrors was made. Devices with NAMs of different lengths were also fabricated and tested, in order to assess the quality of the QWI technique described in Chapter 3 and to evaluate their effect on the COMD power limit. Without NAMs, COMD limited the output power at around 40-50 mW. An optimal NAM length of 150 μm was found as optimal compromise between an increased COMD power and minimized degradation of slope efficiency and threshold current density. COMD-free output powers up to 124 mW were achieved under CW regime, but with degraded LI curve linearity. Similar power levels (with a COMD power of 115 mW) were achieved by using protective facet coatings. In these devices, no degradation of threshold current, slope efficiency or LI linearity was observed. This result demonstrated that the coatings alone can't suppress completely the COMD and need to be used in combination with NAMs, for COMD-free powers higher than 100 mW.

The second part of the chapter described the main approaches used for the characterization of ML lasers. Particular attention was given to the time-domain characterization of the laser output, as this required significant efforts. A dedicated set-up was built for recording TPA interferometric autocorrelation traces, which represent the final proof of the emission of pulses and allow an indirect estimation of pulse-width and peak power. Two kind of TPA detectors were compared for the purpose. A commercial red-laser operating at 651 nm showed a good non-linear response, but in a limited power range, due to a significant linear contribution or to photocurrent saturation. No photocurrent

saturation was instead observed in the fabricated detectors, although a nearly twice non-linearity factor γ was measured, thanks to the optimized material and device design adopted.

Chapter 5

Mode locked lasers results

In this chapter, the main results from the mode locked lasers designed and fabricated in this work are presented. Several cavity designs were considered, but they can be broadly grouped in long devices (> 3 mm) and short ones. Section 5.1 describes the structure and the performance of 3.7 mm long CPM devices, aimed for achieving high output power in ML operation. Some of these devices were fabricated with NAMs on both facets, in order to increase the COMD output power limit. Advantages and disadvantages of the NAMs are discussed and some main conclusions on the output power limitations of such devices are given. Shorter devices (0.6 mm) were also considered in order to produce higher pulse repetition rates. These are described in Section 5.2. In Section 5.3, a different laser epistructure operating at 793 nm is investigated. This wavelength is of interest for a particular spectroscopy application, coherent population trapping in ^{87}Rb . Therefore, details of the application and of the results from such devices will be given, with some considerations on the advantages of the higher d/Γ ratio material employed.

5.1 Mode locked lasers with non-absorbing mirrors

The first ML laser geometry considered in this work consists of a 3.7 mm long cavity with a $2.5\ \mu\text{m}$ wide and $1.8\ \mu\text{m}$ deep ridge waveguide. On both facets, for some devices, NAMs were added in order to increase the COMD output power limit. The optimal NAM length of $150\ \mu\text{m}$ were chosen, as explained in Section 4.4. A CPM configuration was adopted for selecting the first harmonic of the cavity round-trip frequency (around 10 GHz) and thus increase the ML frequency. This configuration also allows for keeping the SA away from the facets, which could otherwise facilitate the occurrence of COMD [44], and away from the NAM sections, in order to avoid QWI effects on the SA. A schematic

of a CPM device with NAMs is shown in Figure 5.1(left), while Figure 5.1(right) shows a SEM picture of the devices.

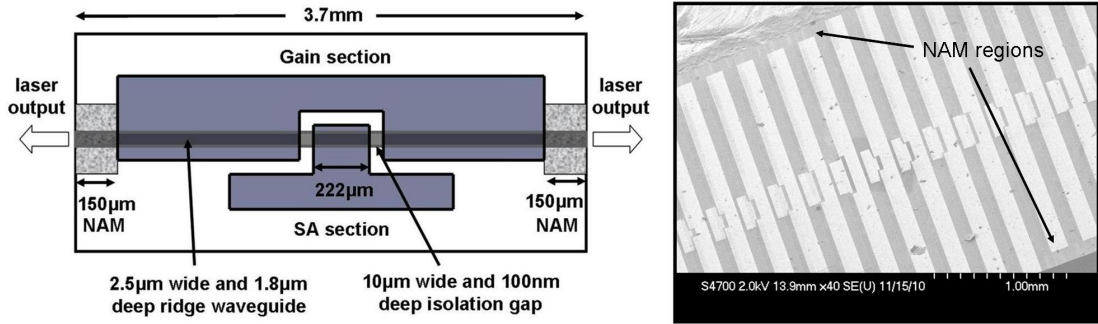


FIGURE 5.1: (left) Schematic of a CPM device with NAMs. Devices without NAMs have the same geometry and cavity length, but the gain section reaches the facets. (right) SEM picture of a laser bar with devices with and without NAMs.

Several SA lengths were considered ranging from 2 to 14% of the cavity length. Devices with short SAs (below 6%) were found to fail easily for reasons that will be explained later in this section, while longer ones were found to have performance similar or degraded compared to the 6% long one. For these reasons, a full characterization was performed only for devices with a 222 μm (6%) long SA. As first test of the fabricated devices, LIs were recorded from CPM lasers with and without NAMs, with the SA forward biased. This test was performed in order to assess their COMD limit. The recorded LIs are reported in Figure 5.2. As shown, the device with NAMs has a threshold current

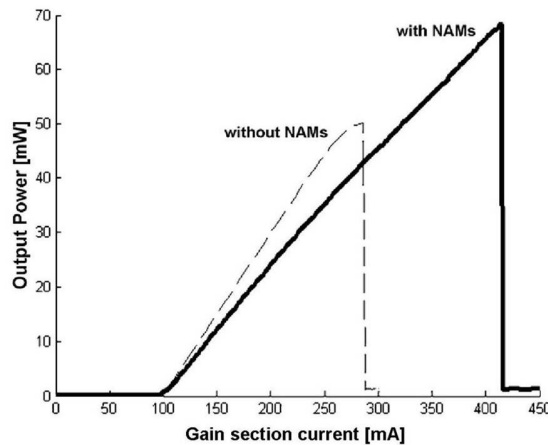


FIGURE 5.2: LI curves for 3.7 mm long CPM devices with 222 μm long SAs forward biased, with (solid line) and without (dashed line) NAMs.

of around 99 mA, while for the non-NAMs device this is around 100 mA. The slope efficiency is around 0.3 W/A without NAMs and decreases of around 0.04 W/A (14.6%) with NAMs. The COMD power is around 50 mW without NAMs, while it is improved by 40% with NAMs. However, COMD was not expected at this power levels (70 mW)

from the results reported in Section 4.4, thus suggesting the presence of some residual absorption in the NAM regions.

Although the output power performance of the NAM devices was not as good as expected from the results in Section 4.4, these were fully characterized and compared with non-NAM lasers, in order to assess the effect of NAMs on ML operation. Another reason for this choice is that the ML regime was found to occur at output powers below the COMD limit and a failure mechanism different from COMD was observed at such lower powers.

A further test included the measurement of the LIIs for several values of the SA reverse bias. The results are shown in Figures 5.3(a) and (b). The output power was measured for the non-NAM device for gain currents I_g between 100 and 240 mA, in step of 4 mA, and SA reverse voltages V_{SA} between 0 and 2 V, in steps of 0.1 V. The NAM device was instead tested for gain currents between 100 and 200 mA, in steps of 4 mA, and SA voltages between 0 and 1.2 V, in steps of 0.1 V. However, they are plotted in the same range for better comparison. These limitations in terms of maximum I_g and maximum

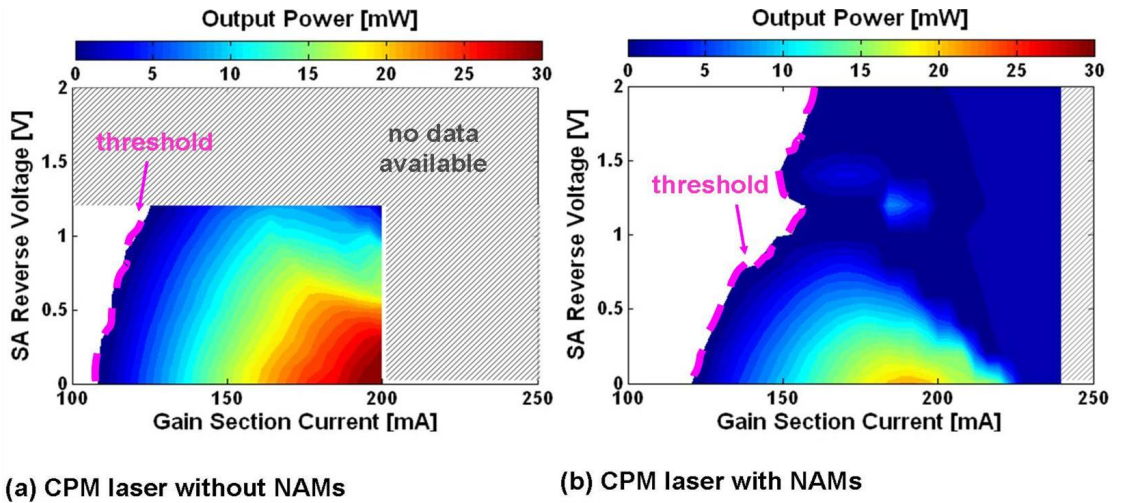


FIGURE 5.3: Map of the output power as function of the gain section current and of the SA reverse bias of 3.7 mm long CPM devices, without (a) and with (b) 150 μm long NAMs on both facets. The gain current step is 4 mA while the SA voltage step is 0.1 V.

V_{SA} were imposed by the failure of the devices due to the damage of the SA. The reason was investigated in this work and will be explained in more detail later in this chapter. However, it can be anticipated that, when a high optical power is absorbed by the SA, a high photocurrent is generated in the SA itself under reverse biasing conditions, causing the catastrophic damage of the SA. The SA failure was recognizable from the $p-n$ junction breakdown, which prevented, after the damage, any current injection in the SA when forward biased. Moreover, this damage also caused the failure of the whole device, which did not lase after the SA degradation. This could also be observed through the

optical microscope during the device operation, because, before the failure, some red light could be seen along the whole gain section length, while, after it, around $300 \mu\text{m}$ of the gain section on both sides of the SA did not emit anymore, indicating the damage of these portions of the gain section as well. Another feature of the recorded LIs is the output power roll-over occurring at relatively high currents. The roll-over power decreases with higher SA reverse voltages. This has been already reported for ML lasers [168], but for higher SA reverse biases. As will be seen in next sections, this behavior significantly affects the laser regimes of operation.

5.1.1 Effect of non-absorbing mirrors on mode locking operation

In order to evaluate the range of mode locking, the RF spectrum was recorded for several values of I_g and V_{SA} . The RF spectrum revealed the presence of peaks around 19.75 GHz, corresponding to twice the round-trip frequency, as expected in CPM operation. The RF peak amplitude (over the noise floor) is mapped as function of I_g and V_{SA} for both non-NAM and NAM devices in Figures 5.4(a) and (b), respectively.

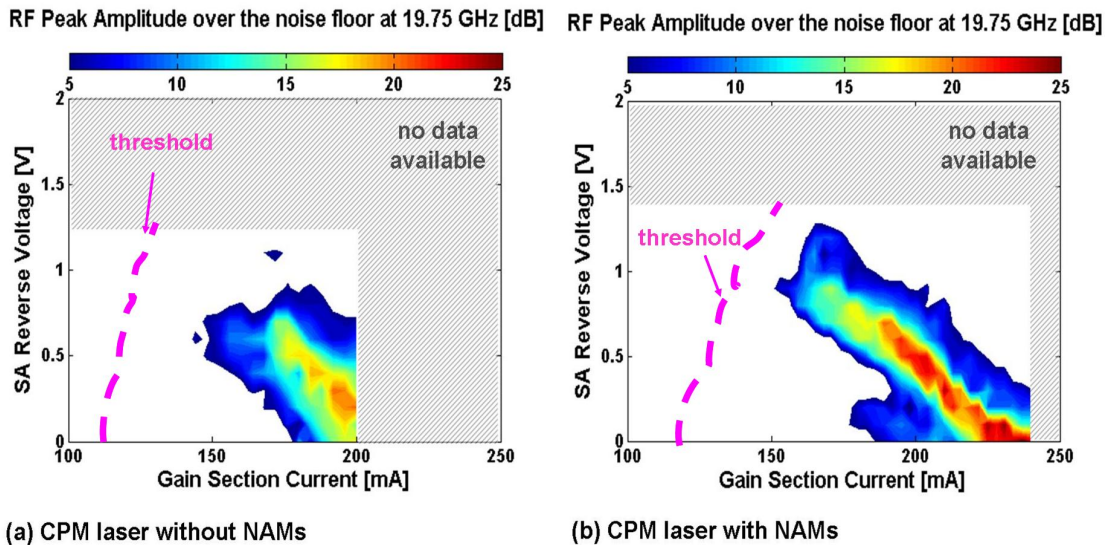


FIGURE 5.4: Map of the 19.75 GHz RF peak amplitude over the noise floor, as function of the gain section current and of the SA reverse bias of 3.7 mm long CPM devices, without (a) and with (b) $150 \mu\text{m}$ long NAMs on both facets. The gain current step is 4 mA while the SA voltage step is 0.1 V.

These maps represent the range of CPM operation, as the emission of pulses was confirmed in this range through autocorrelation measurements. Both NAM and non-NAM devices have the highest RF peak at around $I_g = 200\text{-}210 \text{ mA}$ and $V_{SA} = 0.3 \text{ V}$, but this is stronger and narrower in the device with NAMs, as shown in Figure 5.5(left). The optical spectrum within the range of mode locking has a -3 dB width between 0.2 and 0.55 nm and is slightly larger for the NAM devices. Figure 5.5(right) shows the

correspondent optical spectrum for both devices, where the mode spacing $\Delta\lambda$ doubles the FP cavity one $\Delta\lambda_{FP}$, confirming the CPM operation. The optical bandwidth $\Delta\nu$ is 0.55 nm (0.24 THz) for the device with NAMs, while for the devices without NAMs it is about 0.5 nm (0.22 THz), under best mode locking conditions.

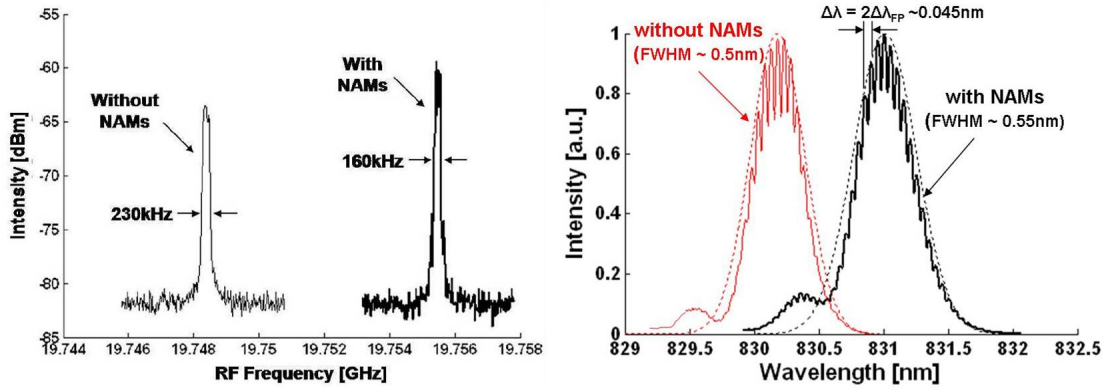


FIGURE 5.5: (left) RF spectra for devices with and without NAMs under best mode locking conditions, for $I_g = 210$ mA and $V_{SA} = 0.3$ V. The -10 dB linewidths are indicated. The measurement resolution bandwidth RBW is 10 kHz, while the video bandwidth VBW is 100 Hz. (right) Optical spectra under best CPM operation for NAM and non-NAM devices, where the FWHM is equal to 0.55 and 0.5 nm, respectively (considering Gaussian envelopes).

An intensity autocorrelation trace for the mode locked NAM device is in Figure 5.6(left). TPA interferometric autocorrelation traces for both devices under best mode locking operation are shown in Figure 5.6(right), with the corresponding FWHM values indicated.

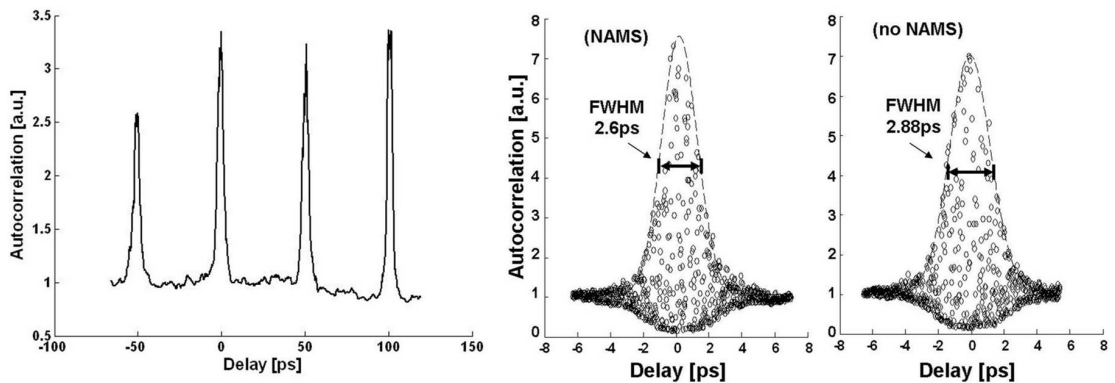


FIGURE 5.6: (left) Intensity autocorrelation trace for the mode locked NAM device. (right) TPA interferometric autocorrelation traces for both NAM and non-NAM devices under best mode locking operation, with the corresponding FWHM values indicated.

As can be seen in Figure 5.6(right), the device with NAMs exhibits 1.84 ps wide pulses (assuming a Gaussian pulse shape), while without NAMs the shortest pulses are 2.04 ps wide. In both cases, they are nearly transform-limited and the average output

powers are 17 mW and 27 mW (corresponding to 462 mW and 675 mW peak powers) in devices with and without NAMs, respectively. The $\approx 10\%$ smaller pulsewidth of the laser with NAMs is consistent with the $\approx 10\%$ wider bandwidth of the optical spectrum. The shorter length ($\approx 10\%$) of the pumped section is also believed to reduce the non-linear phenomena and dispersive effects that usually contribute to broaden the pulses [169]. Furthermore, according to the work of Lau and Paslaski [170, 171] and to what reported in [97], improved ML operation is expected in device geometries with higher steady state gain, which will also benefit from higher gain bandwidth and lower differential gain dg/dN (advantageous for satisfying Equation 2.18). In reference [97], although not directly related to the pulse-width, steady state gain and differential gain are compared in different cavity designs and related to the shorter pulse-width measured in ML lasers with passive sections. In reference [97], it is also suggested to approximate the qualitative form of dependence of dg/dN as function of the carrier density N_g (a material parameter typically not available like in our case), with the derivative dg/dJ of the gain as function of the current density J . The values of g and dg/dJ have been estimated at 830 nm from the gain curves reported in Chapter 4 and are 10.93 cm^{-1} and $25.49 \times 10^{-3} \text{ cm/A}$ for NAM devices, and 9.98 cm^{-1} and $25.67 \times 10^{-3} \text{ cm/A}$ for non-NAM devices. Thus, reduced pulse-widths are obtained consistently with the better mode locking conditions provided by the higher (around 10%) steady-state gain of the devices with passive sections, similarly to what reported in [97, 169]. Moreover, the reduction in pulse-width τ_p is also consistent with the reduction in RF peak power and width $\Delta\nu_{RF}$ observed in devices with NAMs. A dependence $\Delta\nu_{RF} \propto \tau_p^2$ has been also theorized and reported in [172].

5.1.2 Mode locking operation limiting factors

In both NAM and non-NAM lasers, a range of relaxation oscillations self-pulsation regime (SP) was observed from the recorded RF spectra. In this regime of operation, usually lasers emit broad pulses (several ps) at a frequency lower than the cavity round-trip repetition rate and related to the carrier lifetime in the laser gain section [44, 171].

In our case, the RF peaks associated with the SP regime were in the range of 1-5 GHz (main peak at around 1 GHz). The SP peak amplitude (over the noise floor) is mapped as function of I_g and V_{SA} for both non-NAM and NAM devices in Figures 5.7(a) and (b), respectively.

Comparing Figures 5.7 and 5.4, one can deduce that, for a given SA bias, the SP regime occurs at a gain current slightly higher (about 20-30 mA) than the value of best ML operation, preventing mode locking at higher currents and thus higher powers, similarly

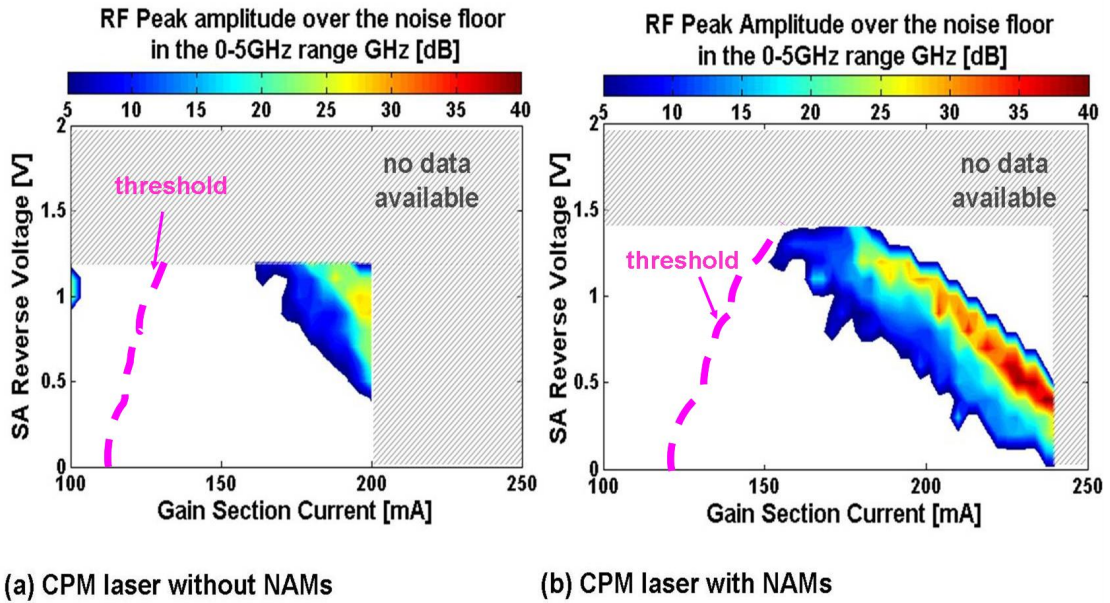


FIGURE 5.7: Map of the SP peak amplitude over the noise floor, as function of the gain section current and of the SA reverse bias of 3.7 mm long CPM devices, without (a) and with (b) 150 μm long NAMs on both facets. The gain current step is 4 mA while the SA voltage step is 0.1 V.

to what reported in [44]. An abrupt jump from one regime to the other was observed when changing the current, with a small region of overlap between the two. Associated to the SP occurrence, an abrupt decrease in the peak wavelength was visible in the optical spectrum, as shown in Figures 5.8(a) and (b), where the peak wavelength is mapped as function of I_g and V_{SA} .

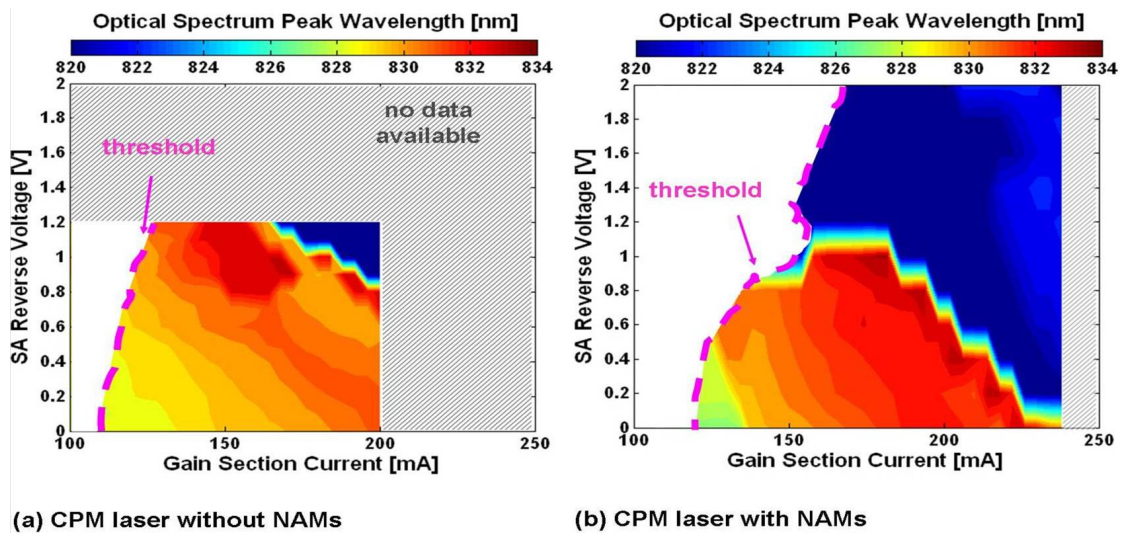


FIGURE 5.8: Map of the peak wavelength as function of the gain section current and of the SA reverse bias of 3.7 mm long CPM devices, without (a) and with (b) 150 μm long NAMs on both facets. The gain current step is 4 mA while the SA voltage step is 0.1 V.

From these plots one can see that when the current is increased, for a given SA bias, the optical spectrum peak moves towards higher wavelengths compared to the threshold value, up to around 832 nm. Above this point, the peak abruptly jumps to around 822 nm. This behavior is similar in NAM and non-NAM devices, the only difference being the current where the abrupt jump occurs. Furthermore, the strongest SP corresponds to the region of low output power in the I_g - V_{SA} map in Figure 5.3. The different regimes of operation are summarized in Figure 5.9(a) for the device with NAMs.

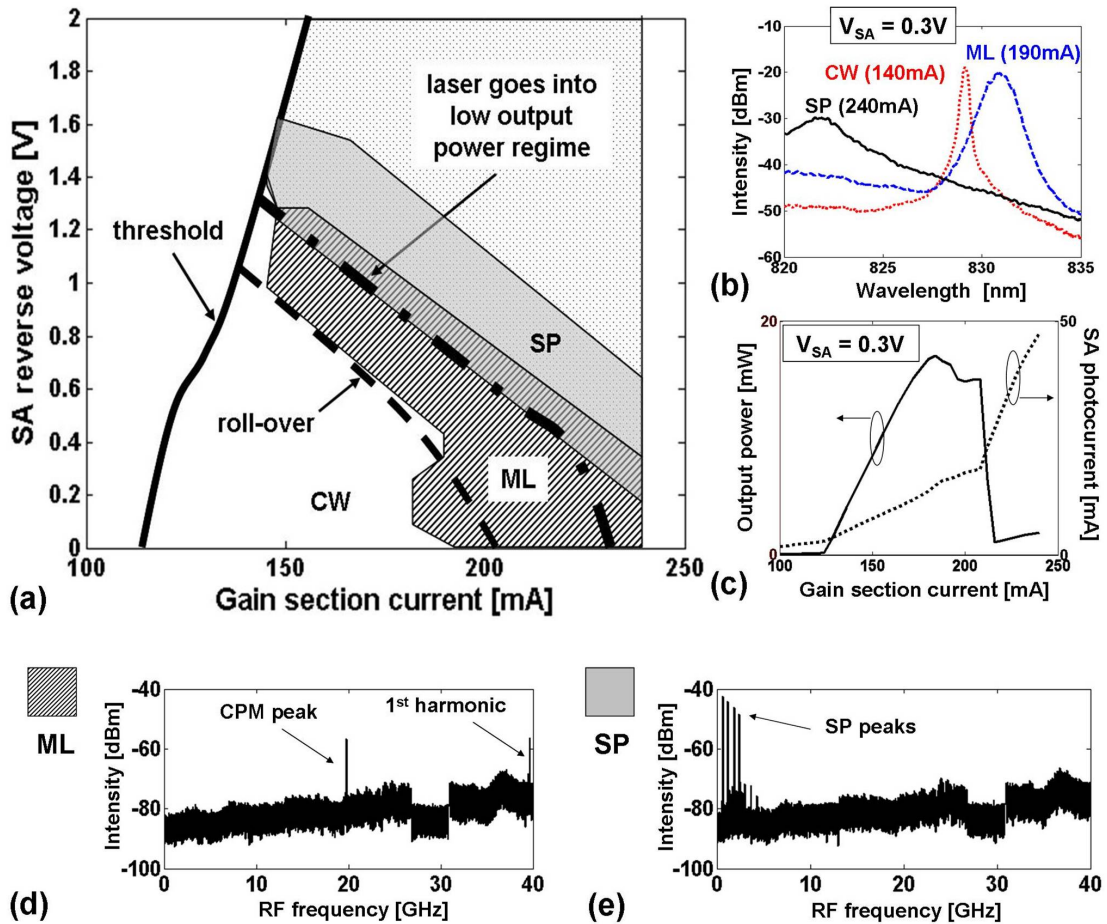


FIGURE 5.9: (a) Map of regimes of operation of the device. Above threshold the laser operates in CW regime, while at around twice threshold switches into ML operation. The upper boundary of the ML range is imposed by the occurrence of SP regime. (b) Examples of the optical spectra in the CW, ML and SP regimes for $V_{SA} = 0.3$ V. An abrupt decrease in peak wavelength is observed when the laser switches from ML (831 nm) to SP (822 nm) operation. In (c), output power and SA photocurrent are plotted as function of the gain section current for $V_{SA} = 0.3$ V. It can be seen that the ML regime is associated to the roll-over in the LI curve. Above this point the output power decreases abruptly due to the high current photo-generated in the SA. Catastrophic damage of the SA occurs for SA currents higher than 50 mA (around 10 kA/cm²). In (d) and (e) the RF spectra under strongest ML and SP operation are reported, respectively. All the plots (a)-(e) refer to the device with NAMs.

In Figure 5.9(b), examples of the recorded optical spectra in the CW, ML and SP regimes are reported for $V_{SA} = 0.3$ V. Output power and SA photocurrent are plotted as function

of the gain section current, for $V_{SA} = 0.3$ V, in Figure 5.9(c). The roll-over in the LI curve of Figure 5.9(c) corresponds to the ML regime. Above this point the output power decreases abruptly due to the high current photo-generated in the SA. Figures 5.9(d) and (e) report the RF spectra under strongest ML and SP operation, respectively.

As seen in Figure 5.9(c), the SA photocurrent increases linearly with increasing gain section current (and thus with increasing optical power in the cavity). This remains true until a certain value of output power is reached, above which the SA photocurrent starts to increase more rapidly with power, forcing the laser to switch regime of operation. One possible explanation is that, when high optical powers are absorbed by the SA, the high SA photocurrent density heats the SA itself, reducing its bandgap. The red-shifted SA will thus absorb more at the lasing wavelength, with a consequent decrease in the laser output power and further increases in the SA bandgap red-shift and temperature. This mechanism, apart from producing the output power roll-over, caused the catastrophic damage of several devices, when the SA photocurrent was not kept below a certain limit (in this case around 50 mA - 9.4 kA/cm²). The effect of the SA red-shift is illustrated in Figure 5.10, where the spectra of laser gain and total cavity losses are plotted. The spectrum of the product $g(\lambda, I_g)L_g$ is indicated in red in Figure 5.10, while the total cavity loss (the sum $\alpha_{MIRR} + \alpha_i L + \alpha_{SA} L_{SA}$) is indicated in blue. These spectra represent the total gain or loss encountered in the laser cavity in one pass by the optical beam and correspond to the data obtained from the multisection measurements discussed in Chapter 4. All the blue curves refer to the absorption spectrum in the case of $V_{SA} = 0.3$ V, but with different wavelength shifts. Three different situations are considered. The first is when the laser is at threshold (I_{th}) and the SA is not particularly heated, thus referred to as 'cold'. In this situation, the gain spectrum clamps as the carrier density clamps at its threshold value. The point where the gain spectrum crosses the loss spectrum corresponds to the threshold wavelength $\lambda_{th} = 830$ nm. As soon as the gain current is increased, the power within the cavity increases, producing a red-shift in the SA bandgap. As an example for the second situation, a shift of 3 nm is considered in Figure 5.10. This shift forces the gain spectrum to red-shift in order to compensate for the increased loss. Therefore, the optical spectrum peak wavelength increases accordingly (as confirmed by the data reported in Figure 5.8). When the optical power in the laser is enough to produce an SA shift of around 6-7 nm, its effect becomes significant. In this condition, as shown in Figure 5.10, the threshold wavelength moves to around 822 nm, where the SA absorption is significantly high. The increased SA absorption makes the SA itself more difficult to bleach, giving rise to relaxation oscillation SP regimes [173], as confirmed by the data in Figure 5.7.

The SA bandgap shrinkage can lead to a thermal run-away and thus to the catastrophic

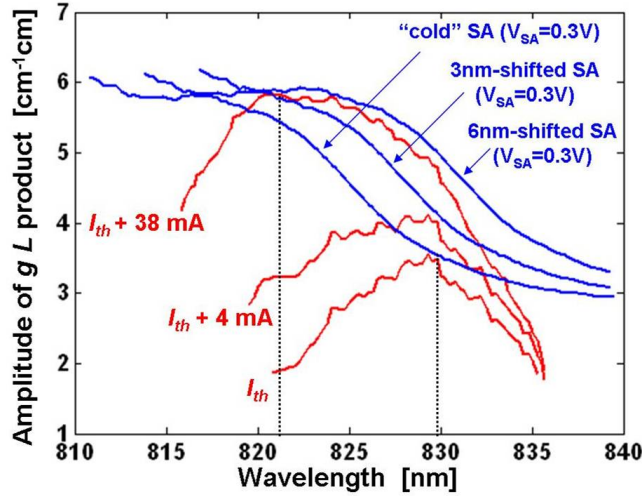


FIGURE 5.10: Plot of the spectrum of the product $g(\lambda, I_g)L_g$ (red curves) and of the total cavity loss (blue curves), given by the sum $\alpha_{MIRR} + \alpha_i L + \alpha_{SA} L_{SA}$. Both gain and absorption data are taken from multisection measurements results described in Chapter 4. All the blue curves refer to the SA absorption spectrum for $V_{SA} = 0.3$ V, but with different wavelength shifts, related to the power in the laser cavity. At threshold (gain curve indicated with current I_{th}), the SA is referred to as "cold" because the power in the cavity is relatively low and the SA is not particularly heated (low SA current photogenerated). The gain and the absorption curves cross each other at $\lambda_{th} = 830$ nm. When the gain current is increased, also the optical power and the SA photocurrent increase. The heated SA red-shifts and the gain curve red-shifts accordingly, in order to compensate for the larger loss. The threshold current thus increases and the slope decreases accordingly. A 3 nm SA red-shift produces a threshold current increase of 4 mA and forces an operating wavelength of 831 nm, while a 6 nm SA red-shift produces a threshold current increase of 38 mA and forces an operating wavelength of 822 nm.

damage of the SA itself. As this mechanism is similar to COMD, it is reasonable to believe that the maximum optical power up to which a laser with an SA can be operated is not far from the COMD limit, around 50 mW in our case. This is in good agreement with what observed from the devices damaged during the test due to COMD. For these devices, the failure occurred at gain currents higher than 250 mA, where the optical power for a fully forward biased device is close to 50 mW. Finally, an indicative estimation of the SA temperature can also be made. From the gain and absorption spectra analysis illustrated in Figure 5.10, an SA red-shift of at least 6-7 nm was estimated in the case of the laser switching from ML to SP. Considering a bandgap wavelength temperature dependence of 0.3 nm/K [174], a temperature increase of 20-23 K can be associated to the 6-7 nm SA red-shift. With this SA shift, as shown in 5.9(c), an SA photocurrent of 20 mA is produced. In this condition, the SA photocurrent increases very quickly with increasing optical power. Moreover, as the SA temperature rise is proportional to the power dissipated in the SA itself, which is in turn proportional to I_{SA}^2 , it is reasonable to expect at least a quadratic dependence of the temperature as function of SA photocurrent (also confirmed in [175] for facet temperature increases due to optical absorption).

Considering destructive SA currents higher than 50 mA, one may expect SA temperatures increases of around 130 K. This value is in reasonable agreement with reported facet temperature increases leading to COMD in GaAs/AlGaAs lasers [70]. However, these estimations should be verified experimentally by measuring the temperature in various device regions, using one of the techniques proposed in literature [175].

5.2 Sub-picosecond colliding pulse mode locking at 126 GHz

Shorter cavity lengths were also considered, in order to produce higher repetition rates. For these devices no NAMs were added. Simple 0.6 mm long CPM devices were fabricated and tested, with a fundamental cavity round-trip frequency of 63 GHz, thus a CPM repetition rate of 126 GHz. SA lengths ranging from 2 to 6% of the cavity length were used and are here compared. The ridge waveguide was again $2.5 \mu\text{m}$ wide and $1.8 \mu\text{m}$ deep, as for the devices described in the previous section. LI curves were measured for several values of the SA voltage and are shown in Figures 5.11(a), (b), (c) and (d) for devices with SA lengths of 2, 3, 4 and 6% of the cavity length, respectively.

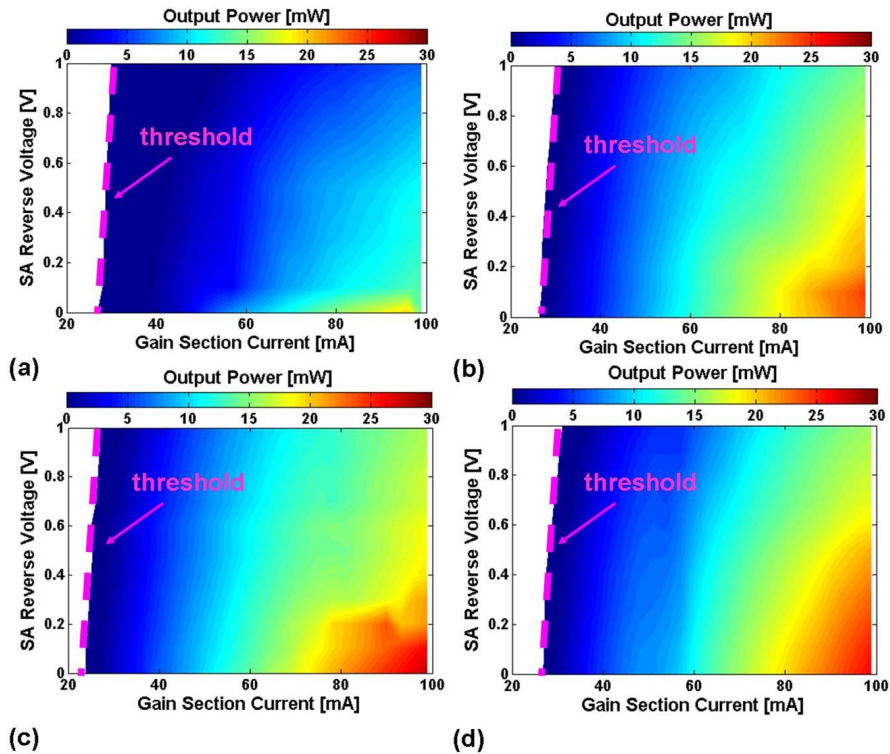


FIGURE 5.11: Map of the output power as function of gain current and SA reverse bias of 0.6 mm long CPM devices with SA lengths of (a) 2, (b) 3, (c) 4 and (d) 6% of the cavity length. The gain current step is 3 mA while the SA voltage step is 0.1 V.

Surprisingly, the maps reported in Figures 5.11 show that devices with longer SAs have higher output powers, within the biasing range considered. The maximum measured powers are 19.84 mW ($I_g = 96$ mA, $V_{SA} = 0$ V), 24.72 mW ($I_g = 99$ mA, $V_{SA} = 0.1$ V), 27.72 mW ($I_g = 99$ mA, $V_{SA} = 0$ V) and 26.3 mW ($I_g = 99$ mA, $V_{SA} = 0$ V) for 2, 3, 4 and 6% long SAs, respectively. This is unexpected, considering that longer SAs introduce higher losses in the cavity and reduce the gain section length, affecting both slope efficiency and threshold current. However, this behavior can be explained considering again the SA heating due to the high optical power absorbed. Longer SAs absorb more due to their higher absorption length, generating more photocurrent for a given optical power in the cavity. However, for a given current density, shorter SAs dissipate heat less efficiently, due to their higher thermal impedance (which depends on $1/L_{SA}$ [53], where L_{SA} is the SA length). The larger heat thus increases the SA absorption (due to bandgap narrowing), reducing the output power. Therefore, a trade-off in the SA performance can be expected due to the combined effects of absorption length and thermal impedance.

The optical spectra were also measured for these devices. The peak wavelength is mapped as function of gain current and SA bias in Figures 5.12(a), (b), (c) and (d).

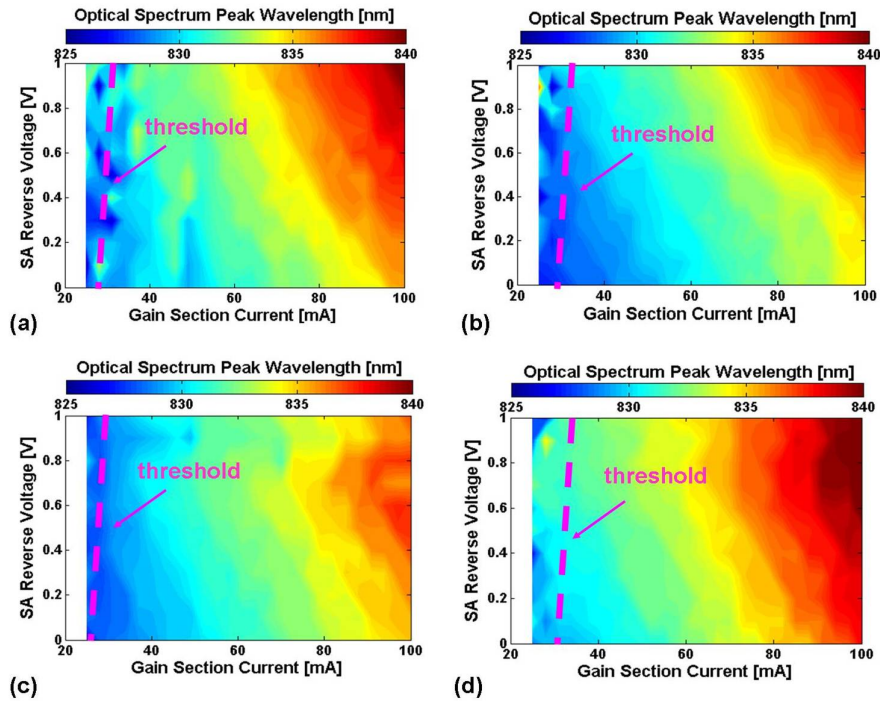


FIGURE 5.12: Map of the optical spectrum peak wavelength as function of the gain section current and of the SA reverse bias of 0.6 mm long CPM devices with SA lengths of (a) 2, (b) 3, (c) 4 and (d) 6% of the cavity length. The gain current step is 3 mA while the SA voltage step is 0.1 V.

Here, one can see that devices with 3 and 4 % SAs operate at slightly lower wavelengths, suggesting that for them the SA red-shift and absorption are lower. This also agrees with their higher optical power. The optical bandwidths are reported in Figures 5.13(a), (b), (c) and (d).

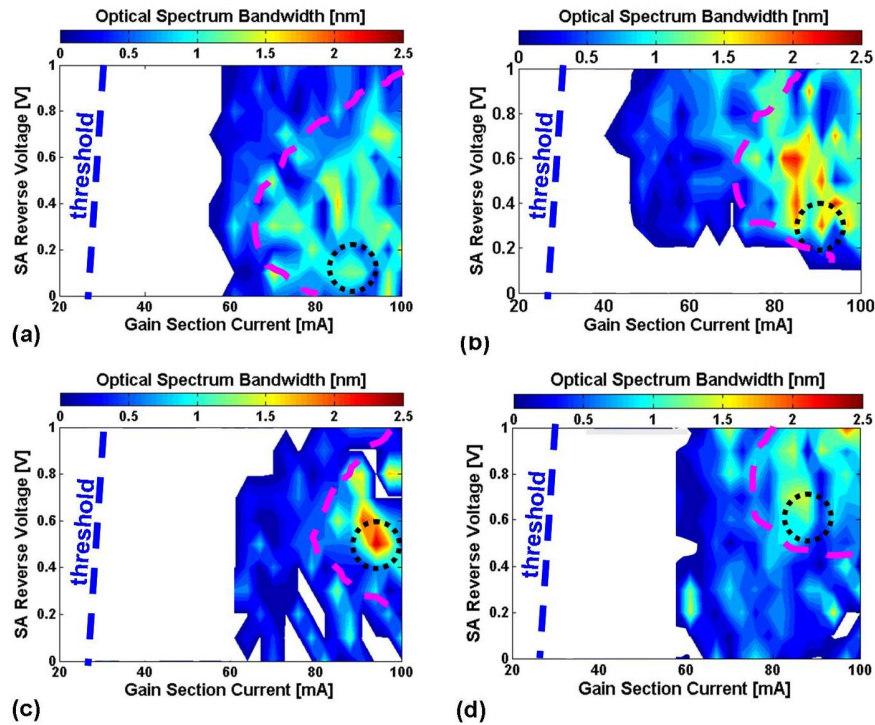


FIGURE 5.13: Map of the optical spectrum bandwidth as function of the gain section current and of the SA reverse bias of 0.6 mm long CPM devices with SA lengths of (a) 2, (b) 3, (c) 4 and (d) 6% of the cavity length. The gain current step is 3 mA while the SA voltage step is 0.1 V. In each subfigure, the blue dashed line indicates the laser threshold, the pink dashed line indicates the ML regime lower boundary and the black dotted circle indicate the region of best mode locking operation (shorter pulses and higher peak-to-background ratio measured in the autocorrelation).

For all the devices a clear region where the bandwidth broadens is visible in the maps in Figures 5.13(right). It was verified by autocorrelation measurements and by the doubling of the cavity mode-spacing, that this region also corresponds to the mode locking operation range, where multiple modes contribute to the laser emission. The region of optical spectrum broadening occurs at progressively higher gain currents and SA reverse voltages when increasing the SA length. This is reasonable because longer SAs are less easily saturated, requiring higher optical powers (thus gain currents). The larger SA reverse voltages can be instead explained in terms of optimal SA absorption required for ML operation. Both SA temperature and reverse bias produce a bandgap red-shift that tunes the SA absorption. Shorter SAs thus require a lower reverse bias as this is accompanied by a temperature-induced increase in absorption.

In the region of larger bandwidth, when CPM operation occurs, the doubling of the mode spacing is visible. In Figures 5.13, the dashed pink lines indicate the ML regime lower boundary, while the black dotted circles indicate the region of best mode locking operation (shorter pulses and higher peak-to-background ratio measured in the autocorrelation). The optical spectrum is reported for each SA length, under best mode locking conditions, in Figures 5.14.

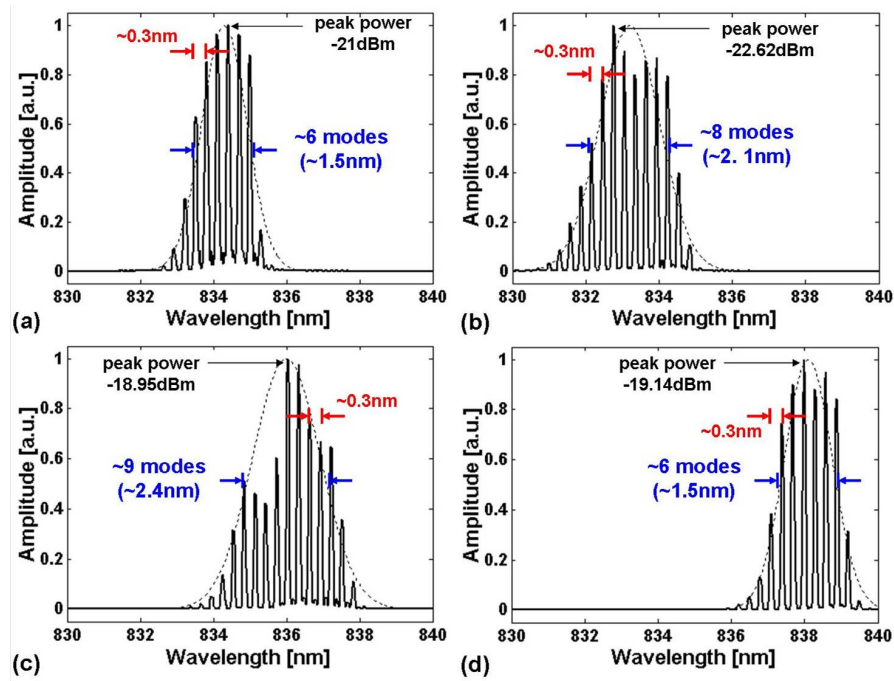


FIGURE 5.14: Optical spectra under best mode locking conditions of 0.6 mm long CPM devices with SA lengths of (a) 2, (b) 3, (c) 4 and (d) 6% of the cavity length. The FWHM values are indicated in blue, while the dashed lines are the best fitting Gaussian envelopes. The gain current and the SA voltage to which each spectrum refers are 88 mA and 0.1 V for the 2%-SA, 88 mA and 0.3 V for the 3%-SA, 94 mA and 0.5 V for the 4%-SA and 88 mA and 0.6 V for the 6%-SA.

The optimal I_g is around 90 mA for all the devices, while the optimal SA reverse bias increases with longer SAs. However, it should be noted that the optical power is not the same in the four cases and is 11.6, 17.4, 17.41 and 16.5 mW for SA lengths of 2, 3, 4 and 6% of the cavity length, respectively. A comparison at the same gain current density or optical power was not possible as the autocorrelation trace peak-to-background ratio and width degraded rapidly when moving from the region of best mode locking. As a result, under best mode locking conditions, the gain current density is higher with longer SAs and the bandwidth larger.

Autocorrelation traces were recorded under best mode locking conditions in the four cases and are reported in Figures 5.15(a), (b), (c) and (d). In the four cases, nearly transform limited pulses were obtained (extracted using a Gaussian shape for the data

fitting) with pulse-widths of around 0.71, 0.5, 0.43 and 0.7 ps for SA lengths of 2, 3, 4 and 6% of the cavity length, respectively. The 4% SA shows the smallest width and highest peak-to-background ratio of the autocorrelation trace, together with the highest average power in ML regime, resulting in the highest peak power of 325 mW. For this device the autocorrelation trace with multiple pulses is reported in Figure 5.16. The peak powers are 136, 287 and 192 mW for for SA lengths of 2, 3 and 6% of the cavity length, respectively.

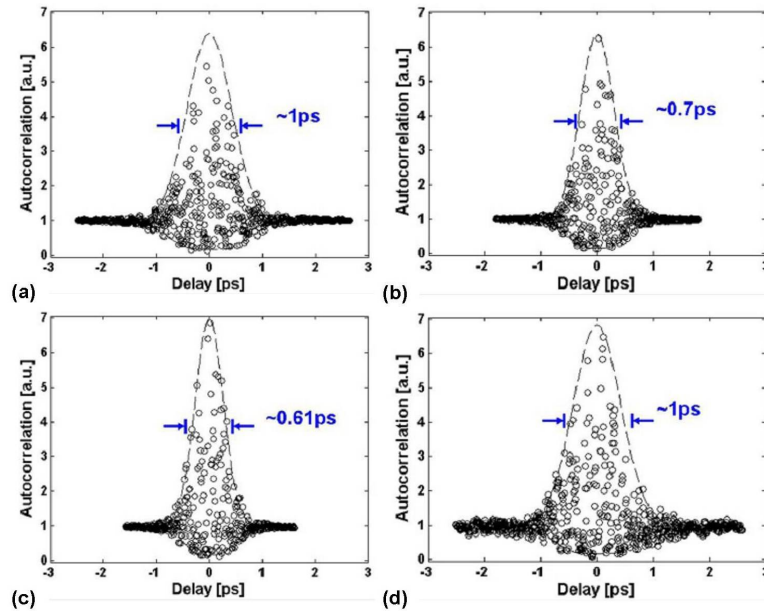


FIGURE 5.15: TPA autocorrelation traces under best mode locking conditions of 0.6 mm long CPM devices with SA lengths of (a) 2, (b) 3, (c) 4 and (d) 6% of the cavity length. The gain current and the SA voltage to which each trace refers are 88 mA and 0.1 V for the 2%-SA, 88 mA and 0.3 V for the 3%-SA, 94 mA and 0.5 V for the 4%-SA and 88 mA and 0.6 V for the 6%-SA.

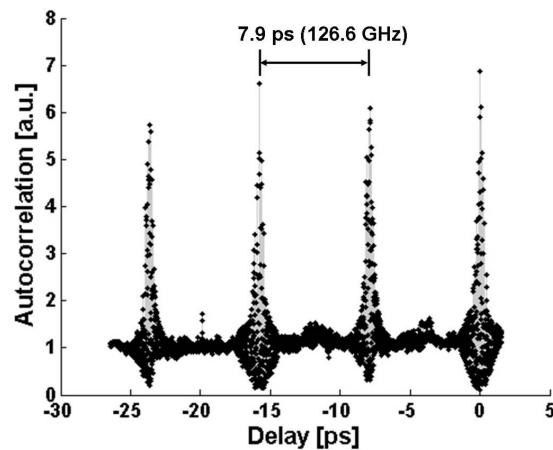


FIGURE 5.16: TPA autocorrelation trace under best mode locking conditions of a 0.6 mm long CPM device with SA length 4% of the cavity length. The gain current and the SA voltage are 94 mA and 0.5 V, respectively.

5.3 Improved mode locked output power in a higher d/Γ laser material

As observed in Section 5.1.2, high power mode locking operation was limited in our devices by the occurrence of SP operation of the laser, associated to high absorption regimes of the SA. COMD occurs at around 50 mW, but mode locking operation was limited at lower power levels (17-27 mW). This was due to the catastrophic damage of the SA produced by the high current densities (destructive when higher than 10 kA/cm²) induced by the absorption of high optical powers (of the same order of the COMD power). As already explained in Section 2.2, higher COMD powers can be obtained with higher d/Γ epistuctures, as in these laser materials the low confinement reduces the modal gain, which can consequently be distributed over longer cavities. The increased mode size also reduces the power density and thus the large absorption induced by the high carrier density at the laser facets. This approach can be used in high power ML lasers, not only to improve the COMD power limit, but also to improve the power limit at which the damage of the SA occurs. Reducing the optical confinement by increasing the mode size can also increase the saturation energy in both the gain and SA sections, thus shifting the mode locking operation towards higher power levels. For these reasons, a different laser material was considered in the last months of this work, with the epilayer structure reported in Table 5.1.

$\text{Al}_x\text{Ga}_{1-x}\text{As}$ layer	mole fraction x (ini.val.-end val.)	thickness [μm]	Doping type and concentration [10^{17}cm^{-3}]	Dopant
cap layer	0	0.2	P ($>3*10^2$)	Carbon
matching layer	0.65-0.1	0.05	P ($3*10^1$)	Carbon
p-cladding	0.65	0.5	P ($1*10^1$)	Carbon
p-cladding	0.65	0.5	P (0.5 - 5)	Carbon
graded index	0.35-0.65	0.09	P (0.5)	Carbon
barrier	0.35	0.007	UD	none
quantum well	~ 0.1	0.007	UD	none
barrier	0.35	0.007	UD	none
graded index	0.55-0.35	0.06	N (0.5)	Silicon
n-cladding	0.55	0.49	N (0.5)	Silicon
F.F.R. graded layer	0.52-0.55	0.02	N (0.5)	Silicon
F.F.R. graded layer	0.52	0.33	N (0.5)	Silicon
F.F.R. graded layer	0.55-0.52	0.02	N (0.5)	Silicon
n-cladding	0.55	1	N ($1*10^1$ -0.5)	Silicon
n-cladding	0.55	1.7	N ($1*10^1$)	Silicon
matching layer	0-0.55	0.02	N ($2*10^1$)	Silicon
buffer	0	0.8	N ($2*10^1$)	Silicon

TABLE 5.1: Epilayer structure of the 793 nm high d/Γ material designed by Intense Ltd.

Similarly to the 830 nm epistucture, this material has a GRIN-SCH waveguide and

contains a FRL in the lower cladding, which extends the mode vertical size. The main difference between the two materials is that, here, only a single QW is inserted in the core and asymmetric cladding layers are used. A ridge waveguide design similar to the one presented in Section 2.2.1 was made also in this case and an optimal ridge geometry for single transverse mode operation was found, with a waveguide width of $3 \mu\text{m}$ and depth of $1.1 \mu\text{m}$. Figures 5.17(a) and (b) show the computed TE mode profile for the designed ridge waveguide and the vertical and horizontal cuts of the computed mode profile. For this ridge structure, an optical confinement of 0.0093 and a d/Γ ratio of 0.753

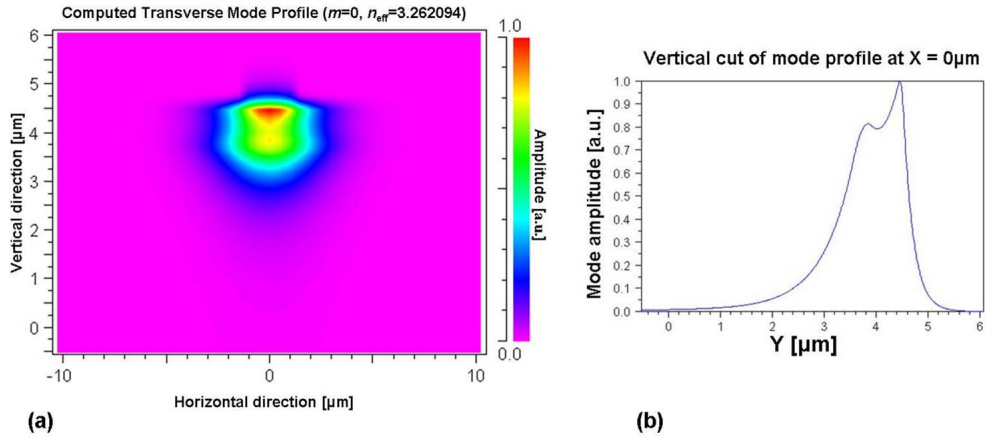


FIGURE 5.17: (a) Computed TE mode profile for a $3 \mu\text{m}$ wide and $1.1 \mu\text{m}$ deep ridge waveguide. (b) Vertical cut of the computed mode profile.

μm were calculated, corresponding to a mode area of $d\omega/\Gamma=2.26 \mu\text{m}^2$. The nearly 70% increase in the mode size compared to the 830 nm material reduces the power density by the same amount and increases, as will be seen later in this chapter, also the power level where ML operation occurs.

5.3.1 Semiconductor passive mode locked lasers for coherent population trapping in ^{87}Rb vapor cells

The material structure in Table 5.1 was designed by Intense Ltd to operate at 793 nm. The reason for the different wavelength is that a particular spectroscopy application was considered at this stage of the project, in collaboration with Professor A. Luiten of the University of Western Australia. At 795 nm, coherent population trapping (CPT) experiments can be performed in ^{87}Rb vapors [176].

CPT is one of the methods commonly used for interrogating some well-defined electron transitions in atomic vapors (such as Cs or Rb) or molecular gases (such as C_2H_2), in alternative to other classical approaches like magnetic spatial deflection or optical pumping [177]. In the implementation of CPT, the atomic ensemble is illuminated with

two optical beams of frequencies ω_1 and ω_2 , respectively. The energy of the beam of frequency ω_1 matches exactly the energy transition, in the atoms of vapor, associated to one of the hyperfine levels of the $S_{1/2}$ ground state and one of the hyperfine levels of the P -state. At the same time, the beam of frequency ω_2 is tuned to an energy close to the energy transition associated to a different hyperfine level of the $S_{1/2}$ ground state and the same hyperfine level of P -state interrogated by ω_1 , as illustrated in Figure 5.18(left) [177].

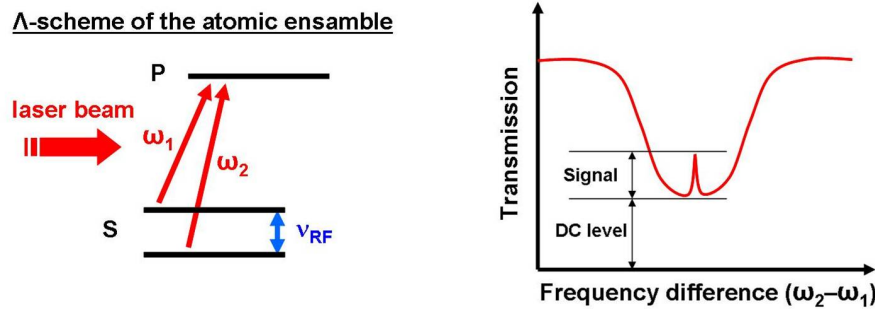


FIGURE 5.18: (left) Illustration of the CPT experiment. The atomic ensemble, in the so-called Λ scheme, is illuminated with two optical beams of frequencies resonant with two specific hyperfine atomic transitions, involving the P and S states. (right) Characteristic transmission spectrum recorded in a CPT experiment [177]. The FWHM of the notch (bright line) is usually of around 0.5-1 kHz

The beam at frequency ω_1 is absorbed by the atoms until the frequency ω_2 is tuned in resonance with the transition between the second hyperfine level of the $S_{1/2}$ ground state and the P -state hyperfine level, forming the so-called Λ scheme. Due to inherent physical quantum properties, interference appears in the excitation process. Once coherence is created in the ground state, the ensemble is placed in a non-absorbing state called a dark state. This phenomenon has been observed in Na, Cs and Rb vapors [177] and it may be observed in several ways. Since in CPT no atoms are excited to the P state at exact resonance, a narrow black line in the fluorescence spectrum of the optically pumped ensemble is observed. Furthermore, since the system does not absorb energy at resonance, it becomes transparent. Consequently, the phenomenon can be observed either on the fluorescence as a black line (generally called a dark line) or on the transmitted radiation as an increase in transmission at resonance (often called a bright line). The characteristic transmission spectrum observable in a CPT experiment is reported in Figure 5.18(right).

Several applications have been proposed for the CPT phenomenon since its early proposals, such as magnetometry, induced transparency, atom cooling, and precision spectroscopy [177]. Furthermore, as the resonance phenomenon reflects all the properties of

the hyperfine resonance in the ground state of the alkali atoms, it can be used to implement an atomic frequency standard [177]. The typical experimental implementation of CPT, as well as of a passive frequency standard, is illustrated in Figure 5.19.

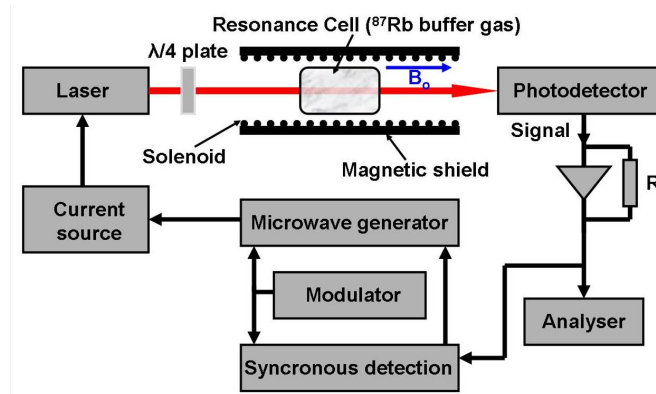


FIGURE 5.19: Experimental arrangement used either to observe the CPT phenomenon in transmission or to implement a passive frequency standard [177].

In Figure 5.19, it can be seen that a sealed cell is used for containing the atomic gas. The miniaturization of the cell is a first aspect to consider for making portable chip-scale atomic clocks and magnetometers based on CPT. To this end, the use of hollow core fibers has also been proposed, particularly advantageous for investigating non-linear optical phenomena requiring long interaction lengths, low linear transmission losses, small mode diameters and diffraction-free propagation of light [178]. Other aspects affecting size, complexity and power consumption of CPT implementations are the laser source and the RF circuit. System designs based on picosecond mode locked lasers have been previously reported for generating the CPT effect, using Ti:Sapphire lasers passively mode locked at a submultiple ($1/57$) of the hyperfine splitting ^{87}Rb levels [176], or laser diodes modulated electrically [179, 180] or with an external electro-optic modulator [181] at half (around 3.41 GHz) of the ^{87}Rb splitting frequency.

In this work, we have investigated a novel approach for achieving CPT in ^{87}Rb vapour cells, based on a 795 nm semiconductor laser passively mode locked at the ^{87}Rb standard frequency (around 6.834 GHz). This approach eliminates the need for any RF driving circuit, allowing for a more compact, integrable and easy to drive implementation of CPT in ^{87}Rb . After some preliminary characterization of the designed and fabricated devices, these have been sent to Professor A. Luiten's group of the University of Western Australia for CPT experiments. The device structure and the results obtained from the preliminary characterization performed in our department are presented in the next section.

5.3.2 Design, fabrication and test of 795 nm passive mode locked lasers with pulse repetition rate of 6.8 GHz

CPT experiments in ^{87}Rb require an operating wavelength of 795 nm. In the choice of the laser material structure, it was considered that, in mode locked lasers, the presence of the SA introduces a small red-shift in the emission wavelength, being the minimum of the SA absorption red-shifted compared to the gain peak. Thus, the laser material shown in Table 5.1 was chosen as it operates at 793 nm. In the design of these passively mode locked lasers, apart from the ridge waveguide optimization, the only critical parameter was the cavity length, while SA lengths of 2, 3 and 4% were considered. A first batch of ML lasers was fabricated using the JWNC clean room facilities and in collaboration with the author's colleague Dr Kris Seunarine, in order to assess the material quality, the emission wavelength and, most importantly, to measure the group refractive index of such devices (found to be around 3.8). The group index was essential in order to establish the exact cavity length required for obtaining a repetition rate as close as possible to the ^{87}Rb hyperfine levels splitting frequency (around 6.8346 GHz). After few attempts, an optimal cavity length of 5.69 mm was determined and an SA length of 227 μm (4% of the cavity length) was found to be optimal for mode locking operation. Smaller SAs were found to fail very quickly when reverse biased. A second batch of lasers was fabricated by the company Compound Semiconductor Technologies (CST) Ltd, following the aforementioned optimized design. These devices were singulated and wire-bonded using appropriate submounts, as shown in Figure 5.20(left). The submount was then fixed on a brass bar where a PCB board was previously fixed. The three contact pads (gain section, SA section and n -contact) on the submount were then wire-bonded to the pads defined on a PCB board, to allow the external control of the devices without the need of probes.

The COMD power limit was not determined, as the few devices fabricated had to be sent to Professor Luiten's group for CPT experiments. However, no COMD was observed at powers up to 93 mW, thus nearly double than in the 830 nm material. One of the recorded LIs is shown in Figure 5.20(right) and is relative to the devices fabricated by CST. The lasers fabricated in the JWNC had similar performance but were operated at powers not higher than 50 mW, to avoid any COMD or SA damage.

An improvement in the output power, compared to the 3.7 mm long devices in the 830 nm material, was observed also when reverse biasing the SA, as shown in the $I_g - V_{SA}$ map in Figure 5.21(left). A maximum power of 60 mW was measured in the biasing range considered. Despite of the increased output power, the SA photocurrent remained relatively small (maximum 25 mA - 3.67 kA/cm²), compared to the 830 nm CPM

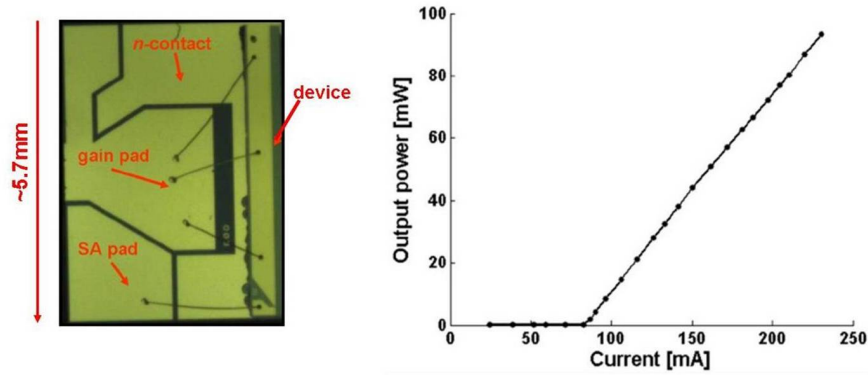


FIGURE 5.20: (Left) Optical microscope picture of a 5.69 mm long mode locked laser fixed on a patterned sub-mount and wire-bonded. (Right) LI curve of a 793 nm mode locked laser with the SA forward biased.

devices (3 times higher with approximately the same SA length) described in Section 5.1, as shown in Figure 5.21(right).

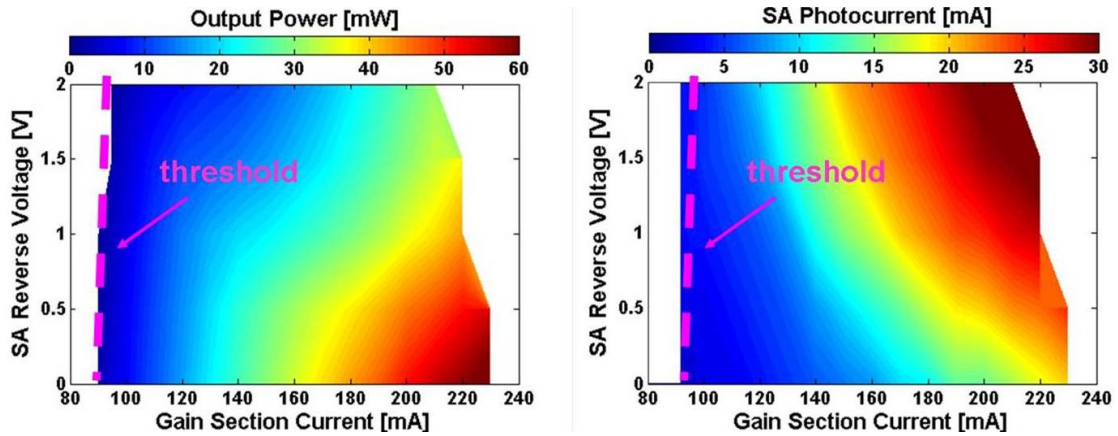


FIGURE 5.21: Map of output power (left) and SA photocurrent (right), as function of gain section current and SA reverse voltage for the 795 nm mode locked laser with a 227 μm long SA at one facet. The gain current step is 10 mA while the SA voltage step is 0.5 V.

The ML operation range in terms of gain current and SA voltage was assessed also in this case by measuring the RF spectrum. From these measurements, RF peak power and frequency were extracted and are plotted in Figures 5.22(left) and (right), respectively. As shown, the highest (25 dB over the noise floor) RF peak occurs for $I_g = 210$ mA and $V_{SA} = 0.5$ V at a frequency of around 6.837 GHz, thus in the range of the ^{87}Rb hyperfine standard frequency.

Figure 5.23(left) reports the optical bandwidth in the ML operation range, which is about 1.5 nm at $I_g = 210$ mA and $V_{SA} = 0.5$ V, where the highest RF peak occurs. The improved SA response to optical power in this material may also be responsible for the improved optical spectrum stability. The peak wavelength remains relatively unchanged when varying the gain current, while it decreases when increasing the SA

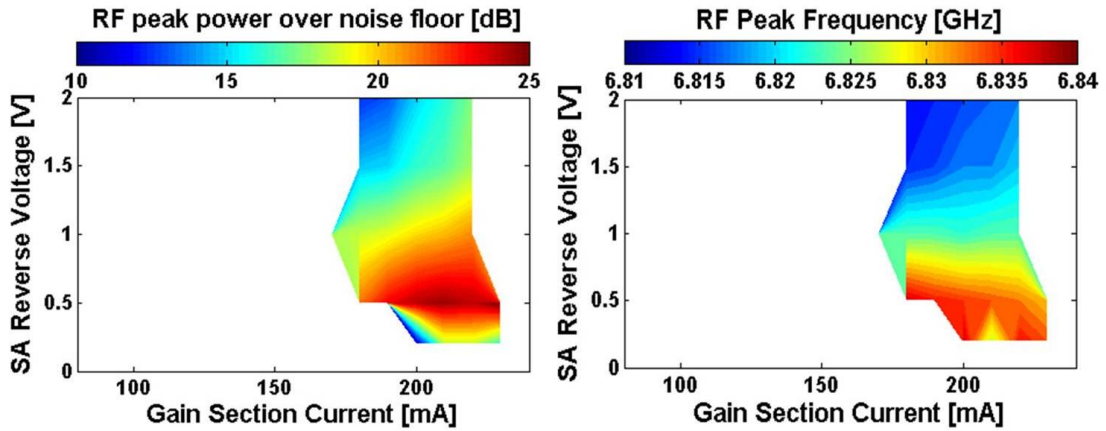


FIGURE 5.22: Map of RF peak power (left) and RF peak frequency (right), as function of gain section current and SA reverse voltage for the 795 nm mode locked laser with a $227 \mu\text{m}$ long SA at one facet.

reverse bias. The peak wavelength is plotted as function of SA bias and for I_g in the range 200-220 mA, in Figure 5.23(right). Multisection measurements may allow for the evaluation of the wavelength detuning between SA band-edge and gain peak and thus a better understanding of the improved device performance, compared to the 830 nm material.

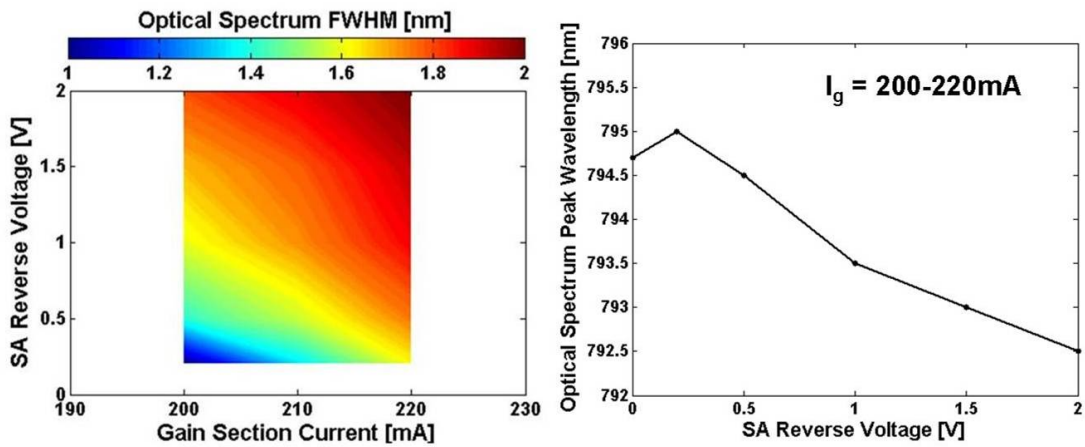


FIGURE 5.23: Map of optical spectrum peak wavelength (left) and bandwidth (right), as function of gain section current and SA reverse voltage for the 795 nm mode locked laser with a $227 \mu\text{m}$ long SA at one facet.

In Figures 5.24(left) and (right), the RF and optical spectra of the device under best ML conditions ($I_g = 210 \text{ mA}$ and $V_{SA} = -0.5 \text{ V}$) are reported.

Under best ML conditions, the autocorrelation was also recorded, confirming the emission of sub-picosecond pulses (0.71 ps) at 6.86 GHz (around 146 ps), as shown in Figures 5.25(left) and (right). The small duty-cycle, given by the ultrashort pulse-width and the

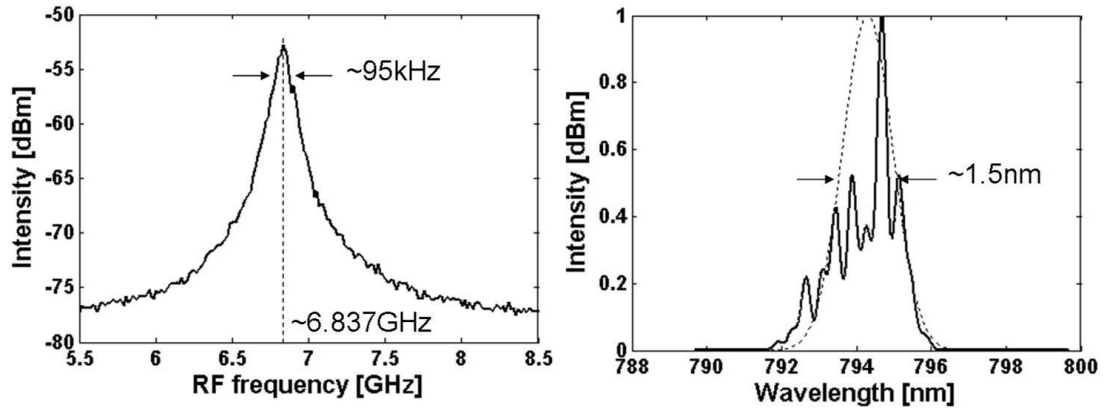


FIGURE 5.24: RF (left) and optical (right) spectra for the laser under best ML conditions ($I_g = 210$ mA and $V_{SA} = 0.5$ V).

relatively low repetition rate, allowed for a very high peak power (around 9.8 W, for an average power of 48 mW) to be achieved.

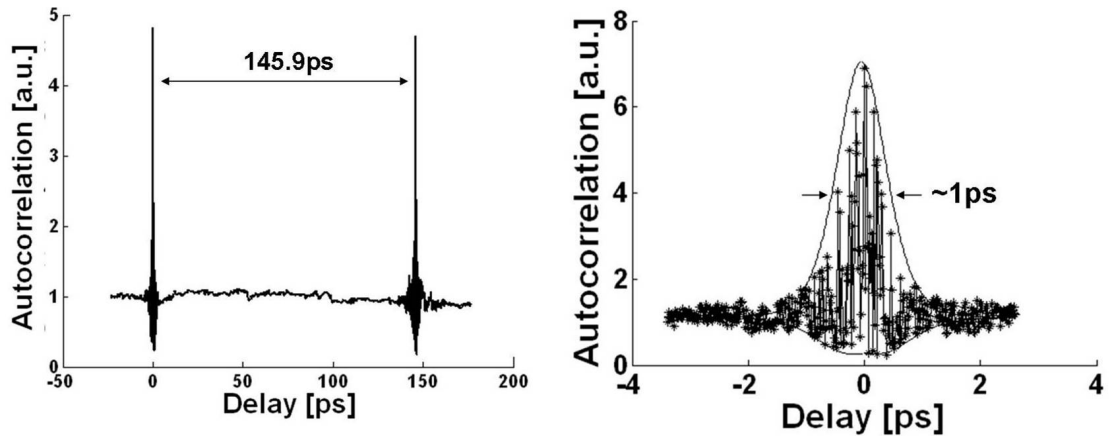


FIGURE 5.25: TPA autocorrelation trace showing (left) the period of pulses and (right) the width of the pulses in the time domain.

The reported results refer to a heat-sink temperature of 20°C. The temperature tuning of the laser was also investigated using the TEC module of the laser driver. It was assessed a wavelength tuning rate of about 0.3 nm/K (in a ± 2 nm range) and an RF frequency tuning rate of about 333 kHz/K (in a ± 2 MHz range), without any significant effect on the power performance of the laser (± 2 mW with ± 5 K).

5.4 Chapter summary

In this chapter, the main results from the fabricated ML lasers were reported and discussed. Different cavity designs and laser materials were investigated. Colliding pulse mode locking was demonstrated in a 830 nm wafer structure. Laser cavity lengths of 3.7

and 0.6 mm were considered, for achieving high power and high frequency mode locking operation, respectively. Fundamental mode locking was instead achieved in a 793 nm laser material with superior performance.

The 3.7 mm long devices allowed for CPM repetition rates of around 20 GHz to be demonstrated. For this geometry, the effect of 150 μm long NAMs was also investigated. It was found a 40% improvement in the COMD power (70 mW) in devices with NAMs, but with a degraded slope efficiency. Under mode locking operation, the output power was limited by the damage of the SA, due to the high photocurrent produced in the SA itself. This resulted in a lower ML average power in NAM lasers (17 mW compared to 27 mW without NAMs). However, it was found that NAMs improved ML operation, forcing an increase in saturated gain and gain bandwidth in the forward biased section. As a result, shorter pulses were produced with NAMs (1.8 ps compared to 2 ps pulses without NAMs), with a higher and narrower RF peak.

The 0.6 mm long devices allowed for sub-picosecond pulses to be generated at CPM repetition rates of around 126 GHz. Devices with SA lengths of 2, 3, 4 and 6% of the cavity length were compared. The device with a 24 μm (4%) long SA was found to be superior in terms of highest peak power (325 mW) and shortest pulse-width (0.43 ps).

In both 3.7 and 0.6 mm long lasers, the SA heating due to the absorption of high optical power affected significantly the device performance. The thermally induced SA bandgap shift caused the reduction of the output power and facilitated the occurrence of SP regimes, due to the increased cavity loss, in the 3.7 mm long CPM devices.

Finally, 5.69 mm long ML devices were fabricated in a different material structure, designed to operate at 793 nm. The laser material and the cavity length were chosen for producing pulses at 795 nm and with repetition rates of 6.834 GHz, of interest for CPT experiments in ^{87}Rb vapor cells. COMD-free output power of 93 mW were measured with all contacts forward biased. The improved COMD performance was obtained thanks to the 50% higher d/Γ ratio of this material (and a 70% larger mode area), compared to the 830 nm epistructure. This also allowed for improved SA performance in ML regime. Under best ML conditions, pulses as short as 0.71 ps with peak powers of around 9.8 W were generated.

Chapter 6

Summary and conclusions

In this research work, the high power operation of monolithic passively mode locked semiconductor lasers was investigated. The GaAs/AlGaAs material system was considered as it allows for wavelengths in the range of 700-850 nm to be generated, of particular interest for down-conversion in LTG GaAs photomixers. In this wavelength range, devices with high peak power may also be employed in non-linear optics applications, such as two-photon microscopy, while devices with high repetition rate can be used for the generation of microwave and millimetrewave signals, as sources of pulses in high speed short-haul communications and in radio-over-fibre high-speed data communication systems, as explained in Chapter 1.

The overall approach for increasing the output power in our devices consisted in the use of epilayer structures with higher d/Γ , aimed to overcome the issues typically encountered in high power semiconductor ridge waveguide lasers. A double QW GRINSCH material operating at 830 nm with d/Γ ratio of 0.5 μm and a single QW GRINSCH material operating at 795 nm with a d/Γ ratio of 0.753 μm were used. Such structures were designed by Intense Ltd for high power applications such as laser printing or laser pumping of solid-state lasers or EDFAs. The high d/Γ ratio of these laser materials is designed to give a better suppression of higher order transversal modes, with an increase of the kink-free output power, to reduce the modal gain per unit length, which can be thus distributed over longer cavities, and to reduce the power density at the facets, with improved COMD power levels. In this work, the mode locking operation in such material structures was investigated for the first time, using different cavity configurations, and the generation of pulses as short as 0.43 ps and peak powers as high as 9.8 W was demonstrated.

In Chapter 2, a brief introduction of the basic background theory and design considerations relative to semiconductor lasers were given. After a short review of the main

progress made with laser diodes, the peculiarities of our 830 nm material were described to justify its use for producing high power ML lasers. An optimal ridge waveguide 2.5 μm wide and 1.8 μm deep was found for single transverse mode operation. A general description of the COMD, the main issue in high power RWLs, was given, with an overview of the two most effective facet passivation techniques: non-absorbing mirrors and protective coatings. In the second part of the chapter, the mechanisms beyond the ML operation of semiconductor lasers were described, with an overview of the main conditions and approaches for generating high peak power ultrashort pulses and high repetition rates. State-of-art performance of monolithic semiconductor ML lasers were reviewed in terms of pulse-width, ML output power and repetition rate. Colliding pulse mode locking was described as simple approach for increasing the pulse repetition rate and was chosen for most of the fabricated ML devices considered in this work.

Chapter 3 described in detail the steps required for the fabrication of monolithic passively mode locked lasers in the GaAs/AlGaAs material system. Significant efforts were required for optimizing the SID QWI technique, chosen in this work for the definition of NAMs in some of our devices. A maximum bandgap shift of 63 nm was assessed in the intermixed samples with PL measurements. Purpose-fabricated lasers allowed for the evaluation of the lateral grading of the QWI process, inside and outside the QWI regions. It was found a spatial resolution of around 125 μm .

In Chapter 4, the results relative to some preliminary work required in this project were presented. In the first part of the chapter, results from several kind of devices were reported. OSLs and RWLs were fabricated and tested in order to evaluate some material parameters from the measured LI curves, like the infinity current density J_∞ , the cavity parameter L_0 , the optimum gain point g_0 , the intrinsic loss α_i and the injection efficiency η_{inj} , which demonstrated the good quality of the 830 nm material in use. Reasonable agreement was obtained from the two set of measurements. Multisection devices were also fabricated and tested for measuring TE and TM gain and absorption spectra, under several forward and reverse biasing conditions. From these measurements, the values of the saturation parameters g_0 and J_0 measured from RWLs were confirmed. These important material parameters were then used for evaluating the performance of more complex devices. In particular, a fairly accurate prediction of threshold current and slope efficiency of RWLs with non-absorbing mirrors was made. Devices with different NAM lengths were also fabricated and tested, in order to assess the quality of the QWI technique described in Chapter 3 and to evaluate their effect on the COMD power limit. Without NAMs, a COMD power limit of 40-50 mW was found. An optimal NAM length of 150 μm was found as best compromise of COMD suppression and reduced degradation of threshold current and slope efficiency due to QWI. COMD-free output powers up to 124 mW were achieved in CW regime, but with degraded LI

curve linearity. Similar power levels (with a COMD power of 115 mW) were achieved by using protective facet coatings. In these devices, no degradation of threshold current, slope efficiency or LI linearity was observed. This result demonstrated that facet coatings can help against COMD but should be used in combination with NAMs, for COMD-free powers higher than 100 mW. In the second part of the chapter, a detailed description of the main approaches used for the characterization of ML lasers was given, with particular attention to the time-domain characterization of the laser output, as this required significant efforts during this research work. A dedicated set-up was built for recording TPA interferometric autocorrelation traces and two different TPA detectors were compared for the purpose. A commercial red-laser operating at 651 nm showed a good non-linear response, but in a limited power range, due to a significant linear contribution or to photocurrent saturation. A bulk material was designed and grown for fabricating TPA detectors with stronger non-linear behavior. Thanks to the optimized material and device design adopted, no photocurrent saturation was observed in these devices, although a nearly twice non-linearity factor γ was measured. Both detectors allowed for the measurement of the non-linear autocorrelation of ML laser outputs and thus pulse-width measurements.

Chapter 5 reported the main results from the fabricated ML lasers. Different cavity designs and laser materials were investigated. CPM lasers were considered for the 830 nm material and with cavity lengths of 3.7 and 0.6 mm, for achieving high power and high frequency ML operation, respectively. The 3.7 mm long cavity allowed for CPM repetition rates of around 20 GHz to be demonstrated. For this geometry, the effect of 150 μm long NAMs was also investigated. It was found a 40% improvement in the COMD power (70 mW) in devices with NAMs, but with a degraded slope efficiency. Under ML operation, the output power was limited by the damage of the SA, due to the high photocurrent produced in the SA itself. This resulted in a lower ML power in the devices with NAMs. However, it was found that NAMs also affect the ML operation, forcing an increase in steady-state gain and gain bandwidth in the forward biased section. As a result, shorter pulses were achieved with NAMs (1.8 ps compared to 2 ps pulses without NAMs), with a higher and narrower RF peak. The 0.6 mm long cavity allowed for sub-picosecond pulses to be generated at CPM repetition rates of around 126 GHz. Devices with SA lengths of 2, 3, 4 and 6% of the cavity length were compared. The 4%-SA was found to be the optimal value in terms of highest peak power (325 mW) and shortest pulse-width (0.43 ps). The smallest measured transform-limited pulse-width of 0.43 ps at 126 GHz is close to the record value of 0.36 ps reported at 1.28 μm in a tapered waveguide GaAs/InGaAs QD ML laser operating at 17 GHz [104]. Finally, 5.69 mm long ML devices were fabricated in a different material structure, designed to operate at 793 nm. The laser material and the cavity length were chosen for producing pulses

at 795 nm and with repetition rates of 6.834 GHz, of interest for CPT experiments in ^{87}Rb vapor cells. A COMD-free output power of 93 mW was measured with all contacts forward biased. Because in the 830 nm material the active mode area was found to be $1.33 \mu\text{m}^2$, while in the 793 nm one this was around 1.7 times higher, an improved COMD performance was obtained at 793 nm, consistently with the reduced power density at the facet. This also allowed for improved performance in ML regime, where the highest average power under ML regime was 48 mW, around 1.7 times higher than the one measured in 3.7 mm long devices in the 830 nm material. Under best ML conditions, pulses as short as 0.71 ps with peak powers of around 9.8 W were generated. This peak power is, to the best of our knowledge, the highest value achieved in monolithic GaAs/AlGaAs QW passively mode locked lasers.

6.1 Future work

Suggestions for future work as a follow up to this project are as follows:

- Modeling and experimental validation of thermal behavior and failure mechanisms of monolithically integrated SAs in high power GaAs/AlGaAs ML lasers. SA design optimization for improving ML output powers, for example, by modifying the ratios of the SA and gain contact lengths and cross sections.
- Improvement of QWI reliability. Investigation of the effect of QWI (with small bandgap shifts - i.e. not higher than 10 nm) for blue-shifting the SA absorption spectrum and evaluating its effect on the SA failure mechanisms limiting the laser ML output power.
- Improvement of heat management for the ML devices. Ceramic sub-mounts or die-bonding may be used for *p*-side up mounting or patterned sub-mounts for *p*-side down mounting. The former one is believed to produce the highest benefits, particularly for the SA section.
- Design and investigation of optimized GaAs/AlGaAs epistructures with higher d/Γ ratio and improved beam profile circularity, for increasing peak power and intensity. Slab coupled waveguides may also be investigated, in combination with monolithically integrated amplifiers.
- Combined use of protective facet coatings and NAMs in ML lasers for improved COMD-free output power operation.
- Modeling of mode locking in high power GaAs/AlGaAs lasers including a comparison with experimental results. Some studies with good agreement between theory

and experiments have been undertaken in the group in the 1.55 μm InGaAsP/InP material system and may be adapted to the GaAs/AlGaAs system investigated in this work.

- Investigation of compound cavity designs for ML operation at higher repetition rates.

Appendix A

Refractive index calculation for $\text{Al}_x\text{Ga}_{1-x}\text{As}$ compounds

The refractive index of $\text{Al}_x\text{Ga}_{1-x}\text{As}$ compounds, for photon energies below the bandgap, can be calculated as [65]:

$$n(\omega) = \sqrt{\frac{\epsilon_1(\omega)}{\epsilon_0}}, \quad (\text{A.1})$$

where ϵ_1 and ϵ_0 are the real part of the permittivity function and the vacuum permittivity, respectively. The imaginary part of the permittivity ϵ_2 can be neglected for optical energies below the bandgap [65]. The ratio ϵ_1/ϵ_0 can be calculated as [65]:

$$n(\omega) = A(x) \left\{ f(y) + \frac{1}{2} \left[\frac{E_g(x)}{E_g(x) + \Delta(x)} \right]^{3/2} f(y_{SO}) \right\} + B(x), \quad (\text{A.2})$$

with

$$f(y) = \frac{1}{y^2} \left[2 - (1+y)^{1/2} - (1-y)^{1/2} \right], \quad (\text{A.3})$$

$$y = \frac{h\nu}{E_g(x)}, \quad (\text{A.4})$$

$$y_{SO} = \frac{h\nu}{E_g(x) + \Delta(x)}. \quad (\text{A.5})$$

In the above equations, $E_g(x)$ and $\Delta(x)$ are the bandgap and spin-orbit splitting energies, respectively. For $\text{Al}_x\text{Ga}_{1-x}\text{As}$ ternaries below the bandgap, the material parameters are:

$$E_g(x) = 1.424 + 1.247x, \quad \Delta(x) = 0.34 - 0.5x \quad (\text{A.6})$$

$$A(x) = 6.64 + 16.92x, \quad B(x) = 9.2 + 9.22x. \quad (\text{A.7})$$

Appendix B

Confined states in GaAs/Al_xGa_{1-x}As quantum wells

The quantized states in a quantum well can be calculated considering the Schrödinger equation, which describes the motion of a particle of mass m and energy E , moving with velocity v in a potential V [58, 65]:

$$\left[-\frac{d}{dz} \frac{1}{m} \frac{d}{dz} + V(z) \right] \Phi(z) = E\Phi(z) \quad (\text{B.1})$$

where $\Phi(z)$ is the envelope function which describes the probability of the particle of being in the position z , with z indicating the direction of material growth and thus of quantization of the energy levels, as shown in Figure B.1. The envelope function is expressed only in the variable z , as the potential energy $V(z)$ is discontinuous only in the z direction, while in the x and y directions both wave vectors k_x and k_y and potential energy are continuous. Equation B.1 has to be solved for both electrons in the conduction band and the holes in the valence band. For electrons, the energy is measured from the bottom of the conduction band in the well (thus positive) and for the holes is measured from the top of the valence band (thus positive). Therefore, the barrier energy V_0 indicated in Figure B.1 is equal to ΔE_c for electrons and ΔE_v for holes. In Figure B.1, the coefficient n is an integer number which represents the quantized energy state in the z direction. Odd values of n produce even solutions to the Schrödinger equation, with even symmetry with respect to the center of the well, while even values of n produce odd solutions, with odd symmetry with respect to the center of the well. The general solution to Equation B.1 takes the form, in each barrier and in the well, takes the form of the superposition of forward and backward propagating waves along z :

$$\Phi(z) = C_1 \exp(jk_z z) + C_2 \exp(-jk_z z), \quad (\text{B.2})$$

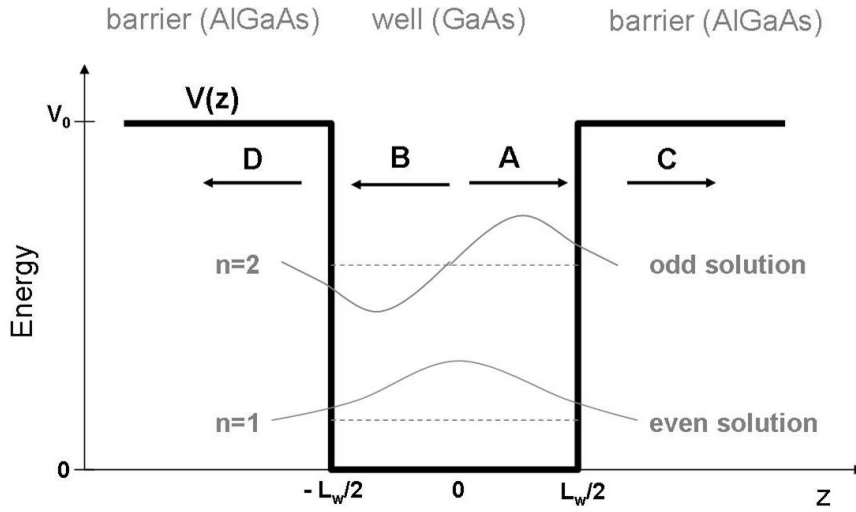


FIGURE B.1: Illustration of the potential $V(z)$ in a quantum well (of width L_w) along the direction of material growth z . Two quantized states $n = 1$ and $n = 2$ in the z direction are shown as an example. Odd values of n produce even solutions to the Schrödinger equation, with even symmetry with respect to the center of the well, while even values of n produce odd solutions, with odd symmetry with respect to the center of the well. The coefficients A and B represent the amplitude coefficients of the periodic wave components propagating back and forward, respectively, along z in the well, while the coefficients C and D represent the amplitude coefficients of the wave components exponentially decaying in the barriers, respectively, along z in the well.

where C_1 and C_2 are amplitude coefficients and k_z is the momentum of the particle along z . Considering that in the barriers the envelope function has to be exponentially decaying (as the probability to find the particle in these regions decreases when the distance from the well increases), while it is oscillatory in the well (as the electron is confined), one obtains that k_z is real in the well and imaginary in the barriers (thus defined as α) and can be expressed as:

$$k_z = \frac{\sqrt{2m_w E}}{\hbar} \quad (\text{B.3})$$

and

$$\alpha = \frac{\sqrt{2m_b(V_0 - E)}}{\hbar}, \quad (\text{B.4})$$

where \hbar is the reduced Planck constant, while m_w and m_b are the particle effective masses in the well and the barrier, respectively. The effective masses for electron and holes are different and also depend on the Al fraction x . Moreover, due to the degeneracy of the valence band energy levels, light-holes and heavy-holes have to be considered with different masses [58, 65]. These are for GaAs/Al_xGa_{1-x}As:

$$m_e = (0.0665 + 0.035x)m_0 \quad (\text{B.5})$$

for the electrons in the conduction band and

$$m_{hh} = (0.34 + 0.42x)m_0 \quad \text{and} \quad m_{lh} = (0.094 + 0.043x)m_0, \quad (\text{B.6})$$

for the holes in the valence band, with m_0 the free electron mass. One may thus express the set of solutions as follows:

$$\Phi(z) = \begin{cases} D_n \exp[\alpha_{zn}(z+L_w/2)] & \text{left barrier} \\ A_n \exp(jk_{zn}z) + B_n \exp(-jk_{zn}z) = \\ (A_n + B_n) \cos(k_{zn}z) + j(A_n - B_n) \sin(k_{zn}z) & \text{well} \\ C_n \exp[-\alpha_{zn}(z-L_w/2)] & \text{right barrier} \end{cases}$$

where the amplitude coefficients A_n, B_n, C_n and D_n can be determined by imposing at each well-barrier interface the continuity of $\Phi(z)$ and $(1/m)(d\Phi(z)/dz)$ as set of two boundary conditions. From the first condition, the amplitudes $B_n = \pm A_n$ and $D_n = \pm C_n$ are found. Even solutions (odd n) will have $B_n = A_n$ and $D_n = C_n$, with an envelope profile with even symmetry with respect to the center of the well, while odd solutions (even n) will have $B_n = -A_n$ and $D_n = -C_n$, with an envelope profile with odd symmetry with respect to the center of the well, as shown in Figure B.1. The second condition then allows for the determination of the eigenvalues k_z and α , which satisfy the following equation:

$$\frac{m_b}{m_w} k_z \tan(k_z \frac{L_w}{2}) = \sqrt{\frac{2m_b(V_0 - E)}{\hbar^2}} \quad (\text{B.7})$$

for odd solutions and the equation:

$$\frac{m_b}{m_w} k_z \cot(k_z \frac{L_w}{2}) = \sqrt{\frac{2m_b(V_0 - E)}{\hbar^2}} \quad (\text{B.8})$$

for even solutions, with

$$k_z = \sqrt{\frac{2m_w E}{\hbar^2}}. \quad (\text{B.9})$$

The roots of Equations B.7 and B.8 are the discrete energy levels of the electrons in the conduction band and heavy-holes and light-holes in the valence band. The roots are found numerically by plotting separately the left-hand and right-hand side functions of Equations B.7 and B.8 and by reading the values of energy where the two functions intersect each other. These functions are plotted in Figures B.2(a), (b) and (c), respectively for the electrons in the conduction band, heavy-holes and light-holes in the valence band, for 4.4 nm wide GaAs/Al_{0.2}Ga_{0.8}As quantum wells. The dashed curves represent

the left-hand side function of Equation B.7, while continuous curves represent the right-hand side function of Equations B.7. The dotted line in Figure B.2(b) represents the odd solution ($n = 2$) for the heavy-holes in the valence band (right-hand side of Equation B.8). From Figures B.2(a), (b) and (c) one can see that there is only one bound state for

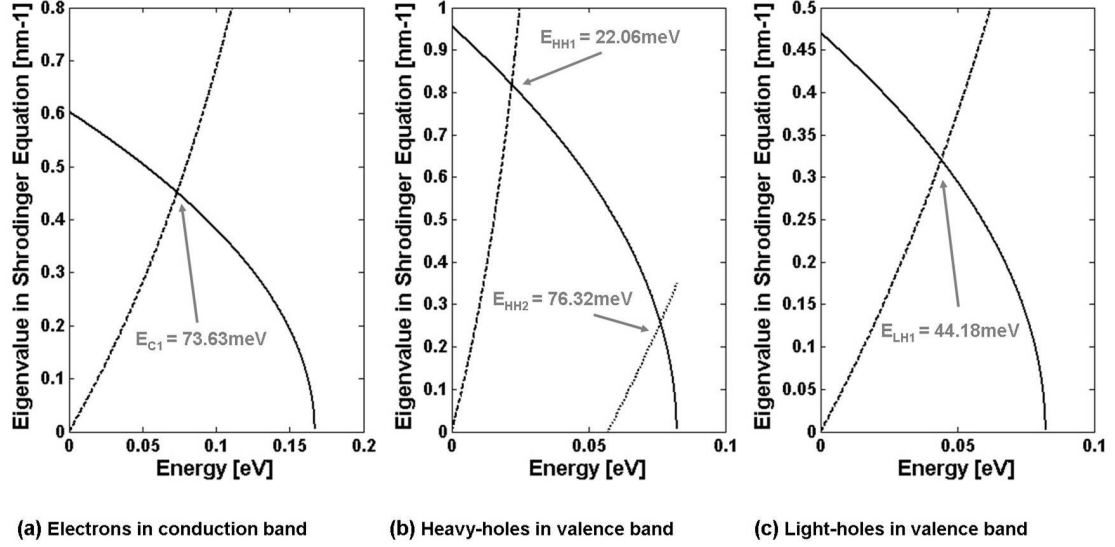


FIGURE B.2: Plot of the functions $(m_b/m_w)k_z \tan(k_z L_w/2)$ (dashed line), $\sqrt{2m_b(V_0 - E)/\hbar^2}$ (continuous line) and $-(m_b/m_w)k_z \cot(k_z L_w/2)$ (dotted line) for the (a) electrons in the conduction band, (b) heavy-holes in the in the valence band and (c) light-holes in the in the valence band, for 4.4 nm wide GaAs/Al_{0.2}Ga_{0.8}As quantum wells. The crossing points between the different plotted functions, give the four eigen-energies $E_{C1} = 73.63$ meV, $E_{HH1} = 22.06$ meV, $E_{HH2} = 76.32$ meV and $E_{LH1} = 44.18$ meV

the electrons in the conduction band, with energy $E_{C1} = 73.63$ meV from the bottom energy of the conduction band in the well. Moreover, in the valence band, one bound state is found for the light-holes at an energy $E_{LH1} = 44.18$ meV below the top of the valence band in the well, while for the heavy-holes two states are obtained with energies of $E_{HH1} = 22.06$ meV and $E_{HH2} = 76.32$ meV below the top of the valence band in the well. Therefore, three electron-hole transitions are available in this structure, with energies calculated as follows:

$$E_{C1-HH1} = E_g(\text{well}) + E_{C1} + E_{HH1} = 1.424 + 0.07363 + 0.02206 = 1.5197\text{eV} \quad (\text{B.10})$$

$$E_{C1-LH1} = E_g(\text{well}) + E_{C1} + E_{LH1} = 1.424 + 0.07363 + 0.04418 = 1.5418\text{eV} \quad (\text{B.11})$$

$$E_{C1-HH2} = E_g(\text{well}) + E_{C1} + E_{HH2} = 1.424 + 0.07363 + 0.07632 = 1.5740\text{eV} \quad (\text{B.12})$$

These transitions, in the wavelength domain, correspond to 816.1, 804.4 and 787.9 nm, respectively. The plot of the energy bands with the quantized energy levels of the GaAs/Al_{0.2}Ga_{0.8}As double QW material structure considered in this work is in Section 2.2.2.

Appendix C

Summary of fabrication steps

The steps used for the fabrication of passively mode locked lasers with non-absorbing mirrors in the GaAs/AlGaAs laser material considered in this work have been explained in Chapter 3. These are reported in summary in Figure C.1.

Initial cleaning

- 5min Opticlear in ultrasonics bath
- 5min Warm Acetone in ultrasonics bath
- 5min IPA in ultrasonics bath
- blow dry

Etched VB6 alignment markers

- 200nm SiO₂ PECVD deposition
- Spin PMMA 4% 2041 at 5000rpm for 60s, bake at 180°C for 30min
- Spin PMMA 4% 2041 at 5000rpm for 60s, bake at 180°C for 120min
- VB6 (e-beam) writing
- Development in 1 MIBK : 1 IPA at 23°C for 35s, IPA 30s, IPA 30s
- BP80+ dry etch for 12min with CHF₃+Ar
- PMMA removing in acetone at 50°C for 15min
- S100 etching (for around 12min) using SiCl₄
- Wet etch in HF for 60s, 30s in RO water, 30s RO water

Definition of non-absorbing mirrors

- 200nm SiO₂ PECVD deposition
- Spin PMMA 15% 2010 at 5000rpm for 60s, bake at 180°C for 30 min
- Spin PMMA 4% 2041 at 5000rpm for 60s, bake at 180°C for 120 min
- VB6 (e-beam) writing
- Development in 1 MIBK : 1 IPA at 23°C for 35s, IPA 30s, IPA 30s
- BP80+ dry etch for 12min with CHF₃+Ar etching
- Sputtering of SID layer
- Lift-off of SID layer in Acetone at 50°C for 5hours – 5min ultrasonics bath
- O₂ plasma ash for 10min at 100W
- 200nm SiO₂ PECVD deposition
- RTA annealing at 800°C for 65s
- Wet etch in HF for 5min, 30s in RO water, 30s RO water
- Sample cleaning using HCl (or digital etching)
- O₂ plasma ash for 10min at 100W

Ridge waveguides

- 200nm SiO₂ PECVD deposition
- Spin PMMA 4% 2041 at 5000rpm for 60s, bake at 180°C for 30min
- Spin PMMA 4% 2041 at 5000rpm for 60s, bake at 180°C for 120min
- VB6 (e-beam) writing
- Development in 1 MIBK : 1 IPA at 23°C for 35s, IPA 30s, IPA 30s
- BP80+ dry etch for 12 min with CHF₃+Ar
- PMMA removing in Acetone at 50°C for 15min
- S100 etching (for around 12min) using SiCl₄

Inter-contact gap definition

- Cleaning in warm acetone and IPA with no ultrasonic
- O₂ ash 10min max power
- Spin PMMA 15% 2010 at 5000rpm for 60s, bake at 180°C for 30min
- Spin PMMA 4% 2041 at 5000rpm for 60s, bake at 180°C for 120min
- VB6 (e-beam) writing
- Development in 1 MIBK : 1 IPA at 23°C for 35s, IPA 30s, IPA 30s
- BP80+ dry etch for 12min with CHF₃+Ar
- S100 etching (for around 1.5min) using SiCl₄ or selective citric acid etch
- Wet etch in HF for 60s, 30s in RO water, 30s RO water

Contact windows definition

- 200nm SiO₂ PECVD deposition
- Spin neat HSQ at 5000 RPM for 60s, bake at 180°C for 60min
- 100nm SiO₂ PECVD deposition
- Spin PMMA 15% 2010 at 5000rpm for 60s, bake at 180°C for 30min
- Spin PMMA 4% 2041 at 5000rpm for 60s, bake at 180°C for 120min
- VB6 (e-beam) writing
- Development in 1 MIBK : 1 IPA at 23°C for 35s, IPA 30s, IPA 30s
- BP80+ dry etch for 25min with CHF₃+Ar
- PMMA cleaning in acetone at 50°C for 30min
- O₂ plasma ash for 10min at 100W

P-contact pads definition

- Spin PMMA 15% 2010 at 5000rpm for 60s, bake at 180°C for 30min
- Spin PMMA 4% 2041 at 5000rpm for 60s, bake at 180°C for 120min
- VB6 (e-beam) writing
- Development in 1 MIBK : 1 IPA at 23°C for 35s, IPA 30s, IPA 30s
- O₂ plasma ash for 60s at 100W
- Deoxidation in 1 HCl : 4 H₂O solution for 30s
- P-Metal deposition using:
 - Plassis II evaporator (Ti_30nm_Pt_50nm_Au_100nm)
 - Sputtering of 300nm of Au)
- Lift-off in acetone at 50°C for one night

Final steps

- Sample mounted face down on a glass slide
(slide pre-spinned with photo-resist at 5000rpm for 7s)
- Glass+sample baked at 90°C for 30min
- Mechanical polishing of the sample substrate using Al oxide powder
(final thickness 100-200µm)
- P-metal deposition using Plassys I evaporator
(14nmAu-14nmGe-14nmAu-11nmNi-240nmAu)
- Sample un-mounted from slide in Acetone at 50°C for 5 hours
- RTA Annealing at 380°C
- Sample cleaving and mounting on brass bars for testing

FIGURE C.1: Summary of steps for the fabrication of mode-locked lasers with non-absorbing mirrors in the GaAs/AlGaAs system.

Bibliography

- [1] Catrina A. Bryce. Epsrc grant. URL <http://gow.epsrc.ac.uk/ViewGrant.aspx?GrantRef=EP/E065112/1>.
- [2] S. McMaster. *Monolithically Integrated Mode-Locked Ring Lasers and Mach-Zehnder Interferometers in AlGaInAs*. Ph.D. dissertation, Department of Electronics and Electrical Engineering, University of Glasgow, UK, 2010.
- [3] P. H. Siegel. THz applications for outer and inner space. In *17th International Zurich Symposium on Electromagnetic Compatibility, EMC-Zurich*, pages 1–4, 2006.
- [4] P. H. Siegel. Terahertz technology. *IEEE Transactions on Microwave Theory and Techniques*, 50(3):910–928, March 2002.
- [5] A. G. Davies, E. H. Linfield, and M. B. Johnston. The development of terahertz sources and their applications. *Physics in Medicine and Biology*, 47(21):3679, 2002.
- [6] E. R. Mueller. Terahertz Radiation: Applications and Sources. *The Industrial Physicist*, pages 27–29, Aug./Sep 2003.
- [7] J. F. Federici, B. Schulkin, F. Huang, D. Gary, R. Barat, F. Oliveira, and D. Zimdars. THz imaging and sensing for security applications explosives, weapons and drugs. *Semiconductor Science and Technology*, 20(7):S266, 2005.
- [8] M. J. Fitch and R. Osiander. Terahertz waves for communications and sensing. *Johns Hopkins APL technical digest*, 25(4):348–355, 2004.
- [9] S. L. Baldochi R. E.l Samad, L. C. Courrol and N. D. Vieira Junior. Ultra-short Laser Pulses Applications. URL http://info.tuwien.ac.at/tubiomed/de/aktuell/Wintner_Laser_Lecture_5p153.pdf.
- [10] S. Kawanishi. High Bit Rate Transmission over 1 Tbit/s. *IEICE Transactions on Electronics*, E84-C(5):509–515, July 2001.

-
- [11] S. Kawanishi. Ultrahigh-speed optical time-division-multiplexed transmission technology based on optical signal processing. *IEEE Journal of Quantum Electronics*, 34(11):2064–2079, November 1998.
- [12] S. Kawanishi and O. Kamatani. All-optical time division multiplexing using four-wave mixing. *Electronics Letters*, 30(20):1697–1698, September 1994.
- [13] R. Ludwig, A. Ehrhardt, W. Pieper, E. Jahn, N. Agrawal, H. J. Ehrke, L. Kuller, and H. G. Weber. 40 Gbit/s demultiplexing experiment with 10 GHz all-optical clock recovery using a modelocked semiconductor laser. *Electronics Letters*, 32(4):327–329, February 1996.
- [14] I. M. White. *A new architecture and technologies for high-capacity next generation metropolitan networks*. Ph.D. dissertation, Stanford University, 2002.
- [15] H. Yasaka, Y. Yoshikuni, K. Sato, H. Ishii, and H. Sanjoh. Multiwavelength light source with precise frequency spacing using mode-locked semiconductor laser and arrayed waveguide grating filter. In *Optical Fiber Communications*, 1996.
- [16] M. Attygalle, H. F. Liu, and A. Nirmalathas. Robust all-optical harmonic clock signal generation through optical injection into passively mode-locked semiconductor lasers. *Photonics Technology Letters, IEEE*, 13(9):1017–1019, September 2001.
- [17] O. Solgaard and K. Y. Lau. Optical feedback stabilization of the intensity oscillations in ultrahigh-frequency passively modelocked monolithic quantum-well lasers. *Photonics Technology Letters, IEEE*, 5(11):1264–1267, November 1993.
- [18] S. Arahira, S. Kutsuzawa, and Y. Ogawa. Extreme timing jitter reduction of a passively mode-locked laser diode by optical pulse injection. *IEEE Journal of Quantum Electronics*, 1999.
- [19] S. Arahira and Y. Ogawa. 480-GHz subharmonic synchronous mode locking in a short-cavity colliding-pulse mode-locked laser diode. *Photonics Technology Letters, IEEE*, 14(4):537–539, April 2002.
- [20] E. Hashimoto, A. Takada, and Y. Katagiri. High-frequency synchronized signal generation using semiconductor lasers. *IEEE Transactions on Microwave Theory and Techniques*, 47(7):1206–1218, July 1999.
- [21] U. Gliese. THz Signal Generation by Laser Mixing. *LO Technology Assessment Report, European Space Agency Contract No. 11653/95/NL/PB, Technical University of Denmark*, 1996.

- [22] E. Hashimoto, A. Takada, and Y. Katagiri. Synchronisation of subterahertz optical pulse train from PLL-controlled colliding pulse modelocked semiconductor laser. *Electronics Letters*, 34(6):580–582, March 1998.
- [23] B.K. Mathason and P.J. Delfyett. Pulsed injection locking dynamics of passively mode-locked external-cavity semiconductor laser systems for all-optical clock recovery. *Journal of Lightwave Technology*, 18(8):1111–1120, August 2000.
- [24] J. W. Waters. Submillimeter-wavelength heterodyne spectroscopy and remote sensing of the upper atmosphere. *Proceedings of the IEEE*, 80(11):1679–1701, November 1992.
- [25] JC Attard and Mitchell. Fibre supported millimetre wave systems. *International Conference on Telecommunications ICT 2002, Beijing, China*, 23 1992.
- [26] D. Wakel. Microwave and millimeter photonics for telecommunications. *Interactions Between Microwaves and Optics, Aufrans, France*, 1999.
- [27] D. Novak, Z. Ahmed, R.B. Waterhouse, and R.S. Tucker. Signal generation using pulsed semiconductor lasers for application in millimeter-wave wireless links. *IEEE Transactions on Microwave Theory and Techniques*, 43(9):2257–2262, September 1995.
- [28] S. Fukushima, C.F.C. Silva, Y. Muramoto, and A.J. Seeds. Optoelectronic synthesis of milliwatt-level multi-octave millimeter-wave signals using an optical frequency comb generator and a unitraveling-carrier photodiode. *Photonics Technology Letters, IEEE*, 13(7):720–722, July 2001.
- [29] U. Brinkmann. Frequency comb spans the spectrum. *Laser Focus World*, 7:38–42, July 2001.
- [30] D. A. Yanson. *Generation of Terahertz-Modulated Optical Signals*. Ph.D. dissertation, Department of Electronics and Electrical Engineering, University of Glasgow, UK, 2003.
- [31] J. R. Morris and Y. R. Shen. Theory of far-infrared generation by optical mixing. *Physics Review A*, 15:1143–1156, March 1977.
- [32] K. A. McIntosh, K. B. Nichols, S. Verghese, and E. R. Brown. Investigation of ultrashort photocarrier relaxation times in low-temperature-grown GaAs. *Applied Physics Letters*, 70(3):354–356, January 1997.
- [33] E. R. Brown, K. A. McIntosh, K. B. Nichols, and C. L. Dennis. Photomixing up to 3.8 THz in low-temperature-grown GaAs. *Applied Physics Letters*, 66(3):285–287, 1995.

- [34] S. Matsuura, M. Tani, and K. Sakai. Generation of coherent terahertz radiation by photomixing in dipole photoconductive antennas. *Applied Physics Letters*, 70(5):559–561, 1997.
- [35] O. Acef, F. Nez, and G. D. Rovera. Optical heterodyning with a frequency difference of 1 THz in the 850-nm range. *Optics Letters*, 19(17):1275–1277, September 1994.
- [36] K. A. McIntosh, E. R. Brown, K. B. Nichols, O. B. McMahon, W. F. Dinatale, and T. M. Lyszczarz. Terahertz photomixing with diode lasers in low-temperature-grown GaAs. *Applied Physics Letters*, 67:3844–3846, December 1995.
- [37] E. L. Portnoi, V. B. Gorfinkel, E. A. Avrutin, I. G. Thayne, D. A. Barrow, J. H. Marsh, and S. Luryi. Optoelectronic microwave-range frequency mixing in semiconductor lasers. *IEEE Journal of Selected Topics in Quantum Electronics*, 1(2):451–460, June 1995.
- [38] M. R. Stone, M. Naftaly, R. E. Miles, I. C. Mayorga, A. i Malcoci, and M. Mikulics. Generation of continuous-wave terahertz radiation using a two-mode titanium sapphire laser containing an intracavity Fabry-Perot etalon. *Journal of Applied Physics*, 97(10):103108–103108–4, May 2005.
- [39] J. Zhang, Y. Hong, S. L. Braunstein, and K. A. Shore. Terahertz pulse generation and detection with LTG - GaAs photoconductive antenna. *Optoelectronics, IEEE Proceedings*, 151(2):98–101, 2004.
- [40] R. Paschotta. Titanium Sapphire Lasers, . URL http://www.rp-photonics.com/titanium_sapphire_lasers.html.
- [41] P.G. May and M. Bierbaum. Monolithic mode locking of long cavity GaAs-AlGaAs semiconductor lasers. *Photonics Technology Letters, IEEE*, 3(4):296–298, April 1991.
- [42] J. F. Martins-Filho, C. N. Ironside, and J. S. Roberts. Quantum well AlGaAs/-GaAs monolithic colliding pulse modelocked laser. *Electronics Letters*, 29(12):1135–1136, June 1993.
- [43] D. A. Yanson, M. W. Street, S. D. McDougall, I. G. Thayne, J. H. Marsh, and E. A. Avrutin. Terahertz repetition frequencies from harmonic mode-locked monolithic compound-cavity laser diodes. *Applied Physics Letters*, 78(23):3571–3573, June 2001.
- [44] P. J. Laybourn G. Giuliani S. Donati M. Passerini, M. Sorel. Fabrication, optimization, and characterization of monolithic semiconductor mode-locked lasers

- and colliding, pulse mode-locked lasers at millimeter-wave frequencies. *Microwave and Terahertz Photonics*, 5466:116–122, 2004.
- [45] M. Passerini, M. Sorel, and P. J. R. Laybourn. Optimisation and regime characterisation of monolithic semiconductor mode-locked lasers and colliding-pulse mode-locked lasers at microwave and millimetre-wave frequencies. *Optoelectronics, IEEE Proceedings*, 151(6):508–512, December 2004.
- [46] C. C. Figura. Second order nonlinear optics in ionically self-assembled thin films. URL <http://scholar.lib.vt.edu/theses/available/etd-061899-103951/unrestricted/cain1.pdf>.
- [47] R. Paschotta. Frequency doubling, . URL http://www.rp-photonics.com/frequency_doubling.html.
- [48] V. Krylov, A. Rebane, A. G. Kalintsev, H. Schwoerer, and U. P. Wild. Second-harmonic generation of amplified femtosecond Ti:sapphire laser pulses. *Optics Letters*, 20(2):198–200, January 1995.
- [49] T. Yoda, H. Yokoyama, K. Sato, H. Taniguchi, and H. Ito. High-peak-power picosecond optical-pulse generation with a gain-switched semiconductor laser, and high-efficiency wavelength conversion. In *Conference on Lasers and Electro-Optics, CLEO/Pacific Rim*, pages 1606–1607, August 2005.
- [50] M. Kuramoto, N. Kitajima, H. Guo, Y. Furushima, M. Ikeda, and H. Yokoyama. Two-photon fluorescence bioimaging with an all-semiconductor laser picosecond pulse source. *Optics Letters*, 32(18):2726–2728, September 2007.
- [51] T. Peter and C. So. Two Photon Excitation Fluorescence Microscopy. *Annual Review on Biomedical Engineering*, 02:399–429, 2000.
- [52] C. Weisbuch. *The Development of Concepts in Light Emitting Devices*. Brazilian Journal of Physics, vol. 26, pp. 21-42, 1996.
- [53] L. A. Coldren and S. W. Corzine. *Diode Lasers and Photonic Integrated Circuits*. New York: John Wiley and Sons, 1995.
- [54] A. Yariv. *Quantum Electronics*. New York: Wiley, 1989.
- [55] G. P. Agrawal and N. K. Dutta. *Semiconductor Lasers*. New York: Van Nostrand Rienhold, 1993.
- [56] J. Wilson and J. F. B. Hawkes. *Optoelectronics: An Introduction*. Prentice- Hall Int'l, 1983.

- [57] H. C. Casey and M. B. Panish. *Heterostructure Lasers*. Academic Press, New York, 1978.
- [58] Jr. Peter S. Zory. *Quantum Well Lasers*. Academic Press, 1993.
- [59] S. M. Sze. *Semiconductor Devices Physics and Technology*. New York, MA: John Wiley and Sons, 2002.
- [60] B. C. Qiu C. J. M. Smith O. Vassalli M. Toury S. D. McDougall C. J. Hamilton S. P. Najda, G. Bacchin and J. H. Marsh. Very large arrays of individually addressable, high power, single mode laser arrays in the 800-1000nm wavelength range obtained by quantum well intermixing techniques. *Proceedings of SPIE*, 5738:33–39, 2005.
- [61] C. S. Harder, L. Brovelli, H. P. Meier, and A. Oosenbrug. High reliability 980-nm pump lasers for Er amplifiers. In *Conference on Optical Fiber Communication*, page 350, February 1997.
- [62] B. Qiu, S. D. McDougall, X. Liu, G. Bacchin, and J. H. Marsh. Design and Fabrication of Low Beam Divergence and High Kink-Free Power Lasers. *IEEE Journal of Quantum Electronics*, 41(9):1124–1130, 2005.
- [63] I. B. Petrescu-Prahova, P. Modak, E. Goutain, D. Silan, D. Bambrick, J. Riordan, T. Moritz, S. D. McDougall, B. Qiu, and J. H. Marsh. High d/gamma values in diode laser structures for very high power. *High-Power Diode Laser Technology and Applications VII - Proceedings of the SPIE*, 7198:71981I–71981I–8, 2009.
- [64] M. Silver, O. P. Kowalski, I. Hutchinson, X. Liu, S. D. McDougall, and J. H. Marsh. Theoretical and experimental study of improved catastrophic optical damage performance in 830nm high power lasers with non-absorbing mirrors. In *Conference on Lasers and Electro-Optics (CLEO)*, volume 1, pages 414–416, May 2005.
- [65] S. L. Cuang. *Physics of optoelectronic devices*. Wiley Inter Science, 1995.
- [66] M. Luisier and S. Odermatt. *Simulation of Semiconductor Lasers*. Diploma Thesis at the Department of Information Technology and Electrical Engineering, Institute of Technology, Zurich, winter 2002/2003.
- [67] Crosslight Software. Many-body, exciton and inhomogeneous broadening effects in device simulation many-simulation. URL http://www.crosslight.com/applications/crosslight_manybody.pdf.
- [68] W. Both, G. Erbert, A. Klehr, R. Rimpler, G. Stadermann, and U. Zeimer. Catastrophic optical damage in GaAlAs/GaAs laser diodes. *Optoelectronics, IEEE Proceedings*, 134(2):135, 1987.

- [69] J. Jimenez. Laser diode reliability: crystal defects and degradation modes. *Comptes Rendus Physique*, 4(6):663 – 673, 2003.
- [70] C. H. Henry, P. M. Petroff, R. A. Logan, and F. R. Merritt. Catastrophic damage of $\text{Al}_x\text{Ga}_{1-x}\text{As}$ double-heterostructure laser material. *Journal of Applied Physics*, 50(5):3721–3732, 1979.
- [71] G. Chen and C. L. Tien. Facet heating of quantum well lasers. *Journal of Applied Physics*, 74(4):2167–2174, 1993.
- [72] W. C. Tang, H. J. Rosen, P. Vettiger, and D. J. Webb. Evidence for current-density-induced heating of AlGaAs single-quantum-well laser facets. *Applied Physics Letters*, 59(9):1005–1007, 1991.
- [73] F. U. Herrmann, S. Beeck, G. Abstreiter, C. Hanke, C. Hoyler, and L. Korte. Reduction of mirror temperature in GaAs/AlGaAs quantum well laser diodes with segmented contacts. *Applied Physics Letters*, 58(10):1007–1009, March 1991.
- [74] H. Horie, Y. Yamamoto, N. Arai, and H. Ohta. Thermal rollover characteristics up to 150°C of buried-stripe type 980-nm laser diodes with a current injection window delineated by a SiN_x layer. *Photonics Technology Letters, IEEE*, 12(1):13–15, January 2000.
- [75] C. L. Walker, A. C. Bryce, and J. H. Marsh. Improved catastrophic optical damage level from laser with nonabsorbing mirrors. *Photonics Technology Letters, IEEE*, 14(10):1394–1396, October 2002.
- [76] L. W. Tu, E. F. Schubert, M. Hong, and G. J. Zyzdik. In-vacuum cleaving and coating of semiconductor laser facets using thin silicon and a dielectric. *Journal of Applied Physics*, 80(11):6448–6451, December 1996.
- [77] H. A. Haus and Y. Silberberg. Theory of mode locking of a laser diode with a multiple-quantum-well structure. *Journal of Optical Society of America B*, 2(7):1237–1243, July 1985.
- [78] H. A. Haus. Theory of mode locking with a fast saturable absorber. *Journal of Applied Physics*, 46(7):3049–3058, 1975.
- [79] J. M. Arnold, E. A. Avrutin, J. H. Marsh, and E. L. Portnoi. Analysis of Nonlinear Optical-Electromagnetic Interactions in Ultrafast Mode-Locked Laser Diodes. In *Ultra-Wideband Short-Pulse Electromagnetics 4*, pages 229–236. Springer US, 2002.

- [80] E. A. Avrutin, J. H. Marsh, J. M. Arnold, T. F. Krauss, H. Pottinger, and R. M. De la Rue. Analysis of harmonic (sub) THz passive mode-locking in monolithic compound cavity Fabry-Perot and ring laser diodes. *Optoelectronics, IEEE Proceedings*, 146(1):55–61, August 1999.
- [81] T. Hoshida, Hai-Feng Liu, M. Tsuchiya, Y. Ogawa, and T. Kamiya. Subharmonic hybrid mode-locking of a monolithic semiconductor laser. *IEEE Journal of Selected Topics in Quantum Electronics*, 2(3), September 1996.
- [82] T. Ohno, H. Ishii, S. Matsuo, H. Okamoto, Y. Kawaguchi, Y. Kondo, I. Furuta, H. Ito, and Y. Yoshikuni. Hybrid modelocking of semiconductor ring lasers incorporating passive deep-ridge waveguides. *Electronics Letters*, 38(16):884–886, August 2002.
- [83] H. Kurita, T. Shimizu, and H. Yokoyama. Experimental investigations of harmonic synchronization conditions and mechanisms of mode-locked laser diodes induced by optical-pulse injection. *IEEE Journal of Selected Topics in Quantum Electronics*, 2(3):508–513, September 1996.
- [84] M. G. Thompson K. A. Williams and I. H. White. Long-wavelength monolithic mode-locked diode lasers. *New Journal of Physics*, 6:179, November 2004.
- [85] H. Haus. Theory of mode locking with a slow saturable absorber. *IEEE Journal of Quantum Electronics*, 11(9):736–746, September 1975.
- [86] H.A. Haus. Mode-locking of lasers. *IEEE Journal of Selected Topics in Quantum Electronics*, 6(6):1173–1185, 2000.
- [87] G. New. Pulse evolution in mode-locked quasi-continuous lasers. *IEEE Journal of Quantum Electronics*, 10(2):115–124, February 1974.
- [88] G.P. Agrawal and N.A. Olsson. Self-phase modulation and spectral broadening of optical pulses in semiconductor laser amplifiers. *IEEE Journal of Quantum Electronics*, 25(11):2297–2306, November 1989.
- [89] A. Kurobe, H. Furuyama, S. Naritsuka, N. Sugiyama, Y. Kokubun, and M. Nakamura. Effects of well number, cavity length, and facet reflectivity on the reduction of threshold current of GaAs/AlGaAs multi-quantum well lasers. *IEEE Journal of Quantum Electronics*, 24(4):635–640, April 1988.
- [90] P. M. Ilroy, A. Kurobe, and Y. Uematsu. Analysis and application of theoretical gain curves to the design of multi-quantum-well lasers. *IEEE Journal of Quantum Electronics*, 21(12):1958–1963, December 1985.

- [91] F. K. Reinhart, I. Hayashi, and M. B. Panish. Mode Reflectivity and Waveguide Properties of Double-Heterostructure Injection Lasers. *Journal of Applied Physics*, 42(11):4466–4479, 1971.
- [92] R. G. M. P. Koumans and R. Van Roijen. Theory for passive mode-locking in semiconductor laser structures including the effects of self-phase modulation, dispersion, and pulse collisions. *IEEE Journal of Quantum Electronics*, 32(3):478–492, mar 1996.
- [93] F. R. Ahmad and F. Rana. Fundamental and Subharmonic Hybrid Mode-Locking of a High-Power (220 mW) Monolithic Semiconductor Laser. *Photonics Technology Letters, IEEE*, 20(15):1308–1310, August 2008.
- [94] F. R. Ahmad and F. Rana. Passively Mode-Locked High-Power (210 mW) Semiconductor Lasers at 1.55- μm Wavelength. *Photonics Technology Letters, IEEE*, 20(3):190–192, February 2008.
- [95] F. R. Ahmad and F. Rana. High Power (150 mW) Electrically Pumped Semiconductor Modelocked Lasers at 1550 nm with Pulse Widths Approaching 6 ps. In *Digest of the IEEE/LEOS Summer Topical Meetings*, pages 163–164, 2007.
- [96] MASS. MIT's Lincoln Laboratory in Lexington. Mode-locked semiconductor laser sets power record, March 2006. URL <http://www.photonics.com/Article.aspx?AID=24588>.
- [97] Y. C. Xin, Y. Li, Vassilios Kovanis, A. L. Gray, L. Zhang, and L. F. Lester. Reconfigurable quantum dot monolithic multisectionpassive mode-locked lasers. *Optics Express*, 15(12):7623–7633, June 2007.
- [98] A. L. Gray H. Huang S. P. G. Kuty H. Li J. Nagyvary F. Nabulsi L. Olona E. Pease Q. Sun C. Wiggins J. C. Zilko Z. Zou P. M. Varangis L. Zhang, L.-S. Cheng. High-power low-jitter quantum-dot passively mode-locked lasers. volume 6115, pages 611502–611508, February 2006.
- [99] A. Gubenko, D. Livshits, I. Krestnikov, S. Mikhrin, A. Kozhukhov, A. Kovsh, N. Ledentsov, A. Zhukov, and E. Portnoi. High-power monolithic passively mod-locked quantum-dot laser. *Electronics Letters*, 41(20):1124–1125, 2005.
- [100] M. A. Cataluna E. U. Rafailov and W. Sibbett. Mode-locked quantum-dot lasers. *Nature Photonics*, 1:395–401, 2007.
- [101] M.G. Thompson, A.R. Rae, Mo Xia, R.V. Penty, and I.H. White. InGaAs Quantum-Dot Mode-Locked Laser Diodes. *IEEE Journal of Selected Topics in Quantum Electronics*, 15(3):661–672, 2009.

- [102] M. G. Thompson, A. Rae, R. L. Sellin, C. Marinelli, R. V. Penty, I. H. White, A. R. Kovsh, S. S. Mikhlin, D. A. Livshits, and I. L. Krestnikov. Subpicosecond high-power mode locking using flared waveguide monolithic quantum-dot lasers. *Applied Physics Letters*, 88(13), March 2006.
- [103] D. Nikitichev, Y. Ding, M. Ruiz, M. Calligaro, N. Michel, M. Krakowski, I. Krestnikov, D. Livshits, M. Cataluna, and E. Rafailov. High-power passively mode-locked tapered InAs/GaAs quantum-dot lasers. *Applied Physics B: Lasers and Optics*, pages 1–5, 2010.
- [104] I. H. White, M. Xia, and R. V. Penty. Ultra-short optical pulse generation by InGaAs quantum-dot diode emitters. In *22nd IEEE International Semiconductor Laser Conference (ISLC)*, pages 168–169, 2010.
- [105] A. Akrouf, K. Merghem, A. Martinez, J.-P. Turrenc, X. Lafosse, G. Aubin, A. Ramdane, F. Lelarge, O. Le Gouezigou, A. Accard, and G.-H. Duan. Ultra high repetition rate and very low noise mode locked lasers based on InAs/InP quantum dash active material. In *IEEE International Conference on Indium Phosphide Related Materials, IPRM*, pages 45–47, May 2009.
- [106] K. Merghem, A. Akrouf, A. Martinez, G. Aubin, A. Ramdane, F. Lelarge, and G.-H. Duan. Pulse generation at 346 GHz using a passively mode locked quantum-dash-based laser at 1.55 μm . *Applied Physics Letters*, 94(2):021107–021107–3, January 2009.
- [107] E. L. Portnoi and A. V. Chelnokov. Passive mode-locking in a short-cavity laser. *Digest of the 12th IEEE Semicond. Conf, Davos, Switzerland*, 1990.
- [108] A. G. Deryagin, D. V. Kuksenkov, V. I. Kuchinskii, E. L. Portnoi, and I. Yu. Khrushchev. Generation of 110 GHz train of subpicosecond pulses in 1.535 μm spectral region by passively modelocked InGaAsP/InP laser diodes. *Electronics Letters*, 30(4):309–311, February 1994.
- [109] A. J. Lowery and P. C. R. Gurney. Comparison of optical processing techniques for optical microwave signal generation. *IEEE Transactions on Microwave Theory and Techniques*, 46(2):142–150, February 1998.
- [110] A. Tanbun T. Ek R. A. Logan M. A. Chin Y. K. Chen, M. C. Wu. Subpicosecond monolithic colliding pulse mode locked multiple quantum well lasers. *Applied Physics Letters*, 58(12):1253–1255, March 1991.
- [111] J. F. Martins-Filho, E. A. Avrutin, C. N. Ironside, and J. S. Roberts. Monolithic multiple colliding pulse mode-locked quantum-well lasers, experiment and theory. *IEEE Journal of Selected Topics in Quantum Electronics*, 1(2):539–551, June 1995.

- [112] Y. Katagiri and A. Takada. A harmonic colliding-pulse mode-locked semiconductor laser for stable subterahertz pulse generation. *Photonics Technology Letters, IEEE*, 9(11):1442–1444, November 1997.
- [113] T. Shimizu, I. Ogura, and H. Yokoyama. 860 GHz rate asymmetric colliding pulse modelocked diode lasers. *Electronics Letters*, 33(22):1868–1869, October 1997.
- [114] S. Arahira and Y. Ogawa. In *Lasers and Electro-Optics Society Annual Meeting LEOS, IEEE*.
- [115] T. Kunii and Y. Matsui. Narrow spectral linewidth semiconductor lasers. *Optical and Quantum Electronics*, 24:719–735, 1992.
- [116] M. Adams and J. Buus. Two-segment cavity theory for mode selection in semiconductor lasers. *IEEE Journal of Quantum Electronics*, 20(2):99–103, 1984.
- [117] L. Coldren and T. Koch. Analysis and design of coupled-cavity lasers-part i: Threshold gain analysis and design guidelines. *IEEE Journal of Quantum Electronics*, 20(6):659–670, June 1984.
- [118] C. Henry and R. Kazarinov. Stabilization of single frequency operation of coupled-cavity lasers. *IEEE Journal of Quantum Electronics*, 20(7):733–744, July 1984.
- [119] A. C. Bryce C. J. Hamilton D. Yanson J. M. Arnold E. A. Avrutin, F. Camacho and J. H. Marsh. Analysis of monolithic parallel-compound-cavity semiconductor lasers for high brightness, single frequency, and short-pulse operation. *presented at the Conference on Lasers and Electro-Optics (CLEO'99), Baltimore, May 1999.*
- [120] D. A. Yanson, M. W. Street, S. D. McDougall, L. G. Thayne, J. H. Marsh, and E. A. Avrutin. Ultrafast harmonic mode-locking of monolithic compound-cavity laser diodes incorporating photonic-bandgap reflectors. *IEEE Journal of Quantum Electronics*, 38(1):1–11, January 2002.
- [121] Intense Ltd. URL <http://www.intenseco.com/technology/default.asp>.
- [122] E-beam lithography course notes S. Thoms and documentation. URL <http://www.jwnc.gla.ac.uk/>.
- [123] Vistec website. URL <http://www.vistec-semi.com/products-applications/products/vistec-vb300/>.
- [124] A. Samarelli. *Micro Ring Resonators in Silicon-on-Insulator*. Ph.D. dissertation, Department of Electronics and Electrical Engineering, University of Glasgow, UK, 2011.

- [125] Surface technology systems Oxford instruments. URL <http://www.oxinst.com/products/etching-deposition-growth/processes-techniques/plasma-deposition/pecvd/Pages/pecvd.aspx>.
- [126] R. Williams. *Modern GaAs Processing Methods*. Nirwood, MA: Artech House, 1990.
- [127] G. C. DeSalvo, W. F. Tseng, and J. Comas. Etch Rates and Selectivities of Citric Acid/Hydrogen Peroxide on GaAs, $\text{Al}_{0.3}\text{Ga}_{0.7}\text{As}$, $\text{In}_{0.2}\text{Ga}_{0.8}\text{As}$, $\text{In}_{0.53}\text{Ga}_{0.47}\text{As}$, $\text{In}_{0.52}\text{Al}_{0.48}\text{As}$, and InP. *Journal of The Electrochemical Society*, 139(3):831–835, 1992.
- [128] G. C. DeSalvo, R. Kaspi, and C. A. Bozada. Citric Acid Etching of $\text{GaAs}_{1-x}\text{Sb}_x$, $\text{Al}_{0.5}\text{Ga}_{0.5}\text{Sb}$, and InAs for Heterostructure Device Fabrication. *Journal of The Electrochemical Society*, 141(12):3526–3531, 1994.
- [129] H. J. Lee, M. S. Tse, K. Radhakrishnan, K. Prasad, J. Weng, S. F. Yoon, X. Zhou, H. S. Tan, S. K. Ting, and Y. C. Leong. Selective wet etching of a GaAs/ $\text{Al}_x\text{Ga}_{1-x}\text{As}$ heterostructure with citric acid-hydrogen peroxide solutions for pseudomorphic GaAs/ $\text{Al}_x\text{Ga}_{1-x}\text{As}/\text{In}_y\text{Ga}_{1-y}\text{As}$ heterojunction field effect transistor fabrication. *Materials Science and Engineering B*, 35(1-3):230–233, 1995.
- [130] J.H. Marsh. Quantum Well Intermixing. *Semiconductor Science and Technology*, 8(6):1136–1155, 1993.
- [131] X. Liu. *Quantum well intermixing in 1.55 um InGaAs/AlInGaAs and InGaAs/InGaAsP structures and applications*. Ph.D. dissertation, Department of Electronics and Electrical Engineering, University of Glasgow, UK, 2002.
- [132] E. J. Skogen, J. S. Barton, S. P. Denbaars, and L. A. Coldren. A quantum-well-intermixing process for wavelength-agile photonic integrated circuits. *IEEE Journal of Selected Topics in Quantum Electronics*, 8(4):863 – 869, 2002.
- [133] Jr. Holonyak, N. Impurity-induced layer disordering of quantum-well heterostructures: discovery and prospects. *IEEE Journal of Selected Topics in Quantum Electronics*, 4(4):584 –594, 1998.
- [134] S. Kee Si, D. H. Yeo, H. H. Yoon, and S. J. Kim. Area selectivity of InGaAsP-InP multiquantum-well intermixing by impurity-free vacancy diffusion. *IEEE Journal of Selected Topics in Quantum Electronics*, 4(4):619 –623, 1998.
- [135] B. S. Ooi, C.J. Hamilton, K. McIlvaney, A. C. Bryce, R.M. De La Rue, J. H. Marsh, and J. S. Roberts. Quantum-well intermixing in GaAs-AlGaAs structures

- using pulsed laser irradiation. *Photonics Technology Letters, IEEE*, 9(5):587–589, May 1997.
- [136] C. J. McLean, J. H. Marsh, R. M. De La Rue, A. C. Bryce, B. Garrett, and R. W. Glew. Layer selective disordering by photoabsorption-induced thermal diffusion in InGaAs/InP based multiquantum well structures. *Electronics Letters*, 28(12):1117–1119, 1992.
- [137] S. Charbonneau, E. S. Koteles, P. J. Poole, J. J. He, G. C. Aers, J. Haysom, M. Buchanan, Y. Feng, A. Delage, F. Yang, M. Davies, R. D. Goldberg, P. G. Piva, and I.V. Mitchell. Photonic integrated circuits fabricated using ion implantation. *IEEE Journal of Selected Topics in Quantum Electronics*, 4(4):772–793, 1998.
- [138] O. P. Kowalski, C. J. Hamilton, S. D. McDougall, J. H. Marsh, A. C. Bryce, R. M. De La Rue, B. Vogele, C. R. Stanley, C. C. Button, and J. S. Roberts. A universal damage induced technique for quantum well intermixing. *Applied Physics Letters*, 72(5):581–583, February 1998.
- [139] M. A. Lieberman and A. J. Lichtenberg. *Principles of plasma discharges and materials processing*. Wiley, 1994.
- [140] J. H. Davies. *The Physics of Low-Dimensional Semiconductor. An Introduction*. Cambridge, UK: Cambridge University Press, 1998.
- [141] K. L. Chavez and D. W. Hess. A Novel Method of Etching Copper Oxide Using Acetic Acid. *Journal of The Electrochemical Society*, 148(11):G640–G643, 2001.
- [142] Malack L. Kdela R. kriniarov J. Greguov D., Eli P. Wet chemical MESA etching of InGaP and GaAs with solutions based on HCl, CH₃COOH, and H₂O₂. *physica status solidi*, 151(1):113–1183, 1995.
- [143] P. Bhattacharya. *Semiconductor optoelectronic devices (2nd ed.)*. Upper Saddle River, NJ, USA: Prentice-Hall, Inc., 1996.
- [144] T. C. Shen, G. B. Gao, and H. Morkoc. Recent developments in ohmic contacts for III – V compound semiconductors. *Journal of Vacuum Science Technology B: Microelectronics and Nanometer Structures*, 10(5):2113–2132, September 1992.
- [145] V. L. Rideout. A review of the theory and technology for ohmic contacts to group III-V compound semiconductors. *Solid-State Electronics*, 18(6):541–550, 1975.
- [146] M. N. Yoder. Ohmic contacts in GaAs. *Solid-State Electronics*, 23(2):117–119, 1980.

- [147] R. Williams. *Modern GaAs Processing Methods*. Brazilian Journal of Physics, vol. 26, pp. 21-42, 1996.
- [148] E.A. Avrutin, J.M. Arnold, and J.H. Marsh. Dynamic modal analysis of monolithic mode-locked semiconductor lasers. *Selected Topics in Quantum Electronics, IEEE Journal of*, 9(3):844–856, 2003.
- [149] J. D. Thomson, H. D. Summers, P. J. Hulyer, P. M. Snowton, and P. Blood. Determination of single-pass optical gain and internal loss using a multisection device. *Applied Physics Letters*, 75(17):2527–2529, October 1999.
- [150] M. Jain and C.N. Ironside. A multi-section technique for the electroabsorption measurements in waveguide semiconductor electroabsorption modulators. *Optoelectronics, IET*, 1(4):163–168, August 2007.
- [151] M. Yamada, S. Ogita, M. Yamagishi, and K. Tabata. Anisotropy and broadening of optical gain in a GaAs/AlGaAs multi-quantum-well laser. *IEEE Journal of Quantum Electronics*, 21(6):640–645, June 1985.
- [152] H. Kobayashi, H. Iwamura, T. Saku, and K. Otsuka. Polarisation-dependent gain-current relationship in GaAs-AlGaAs MQW laser diodes. *Electronics Letters*, 19(5):166–168, 3 1983.
- [153] T. Hayakawa, T. Suyama, K. Takahashi, M. Kondo, and S. Yamaoto. Polarization-dependent gain-current relationship in (111)-oriented GaAs/AlGaAs quantum-well lasers. *Journal of Applied Physics*, 64:297–302, July 1988.
- [154] E A Avrutin, I E Chebunina, I A Eliachevitch, S A Gurevich, M E Portnoi, and G E Shtengel. TE and TM optical gains in AlGaAs/GaAs single-quantum-well lasers. *Semiconductor Science and Technology*, 8(1):80, 1993.
- [155] M. Jain and C.N. Ironside. Internal optical loss measurements in InGaAs-InAlGaAs quantum-well lasers operating around 1550 nm. *Photonics Technology Letters, IEEE*, 15(5):631–633, May 2003.
- [156] L.D. Zhu, F.K. Xiong, C.M. Wang, C.M. Chen, Y.L. Hsie, G.A.B. Feak, and J.M. Ballantyne. GaAs/GaAlAs graded index separate confinement single quantum well single-mode waveguide electroabsorption light modulator. *Optoelectronics, IEEE Proceedings J*, 138(5):313–318, October 1991.
- [157] C.M. Wang Z.H. Chen Y.L. Hsie G.A.B. Feak J.M. Ballantyne L.D. Zhu, F.K. Xiong. Many-Body Effects in the Electron-Hole Plasma Confined in GaAs-(GaAl)As Quantum Wells. *Quantum Wells in Optoelectronics, IEEE Proceedings, Vol. 138, NO. 5,*, October 1991.

- [158] D. A. B. Miller, D. S. Chemla, T. C. Damen, A. C. Gossard, W. Wiegmann, T. H. Wood, and C. A. Burrus. Band-Edge Electroabsorption in Quantum Well Structures: The Quantum-Confined Stark Effect. *Physics Review Letters*, 53(22): 2173–2176, November 1984.
- [159] R.W. Lambert, T. Ayling, A.F. Hendry, J.M. Carson, D.A. Barrow, S. McHendry, C.J. Scott, A. McKee, and W. Meredith. Facet-passivation processes for the improvement of Al-containing semiconductor laser diodes. *Journal of Lightwave Technology*, 24(2):956–961, February 2006.
- [160] S. D. McDougall. *Monolithic colliding pulse mode-locking of AlGaAs/GaAs and InGaAs/InGaAsP quantum well lasers*. Ph.D. dissertation, Department of Electronics and Electrical Engineering, University of Glasgow, UK, 1997.
- [161] Yanong Ning, K. T. V. Grattan, B. T. Meggitt, and A. W. Palmer. Characteristics of laser diodes for interferometric use. *Applied Optics*, 28(17):3657–3661, September 1989.
- [162] A. Reisinger, C. David, K. Lawley, and A. Yariv. Coherence of a room-temperature CW GaAs/GaAlAs injection laser. *IEEE Journal of Quantum Electronics*, 15(12): 1382–1387, December 1979.
- [163] K. Sala, G. Kenney-Wallace, and G. Hall. CW autocorrelation measurements of picosecond laser pulses. *IEEE Journal of Quantum Electronics*, 16(9):990–996, September 1980.
- [164] J. C. Diels and W. Rudolph. Characteristics of fs light pulses. *Ultrashort pulse phenomena, San Diego: Acad. Press*, pages 1–12, 1996.
- [165] D. A. Yanson, M. W. Street, S. D. McDougall, L. G. Thyne, J. H. Marsh, and E. A. Avrutin. Ultrafast harmonic mode-locking of monolithic compound-cavity laser diodes incorporating photonic-bandgap reflectors. *IEEE Journal of Quantum Electronics*, 38(1):1–11, January 2002.
- [166] A. Shimizu, T. Ogawa, and H. Sakaki. Two-photon absorption spectra of quasi-low-dimensional exciton systems. *Physics Review B*, 45(19):11338–11341, May 1992.
- [167] M. M. Karwlanehchi, D. A. Barrow, A. C. Bryce, C. J. Hamilton, and J. H. Marsh. The influence of single-photon absorption on the performance of the two-photon waveguide autocorrelator. *IEEE Journal of Quantum Electronics*, 33(6):933–937, June 1997.

- [168] C. T. A. Brown, M. A. Cataluna, A. A. Lagatsky, E. U. Rafailov, M. B. Agate, C. G. Leburn, and W. Sibbett. Compact laser-diode-based femtosecond sources. *New Journal of Physics*, 6(1):175, 2004.
- [169] F. Camacho, E.A. Avrutin, P. Cusumano, A. Saher Helmy, A.C. Bryce, and J. H. Marsh. Improvements in mode-locked semiconductor diode lasers using monolithically integrated passive waveguides made by quantum-well intermixing. *Photonics Technology Letters, IEEE*, 9(9):1208–1210, 1997.
- [170] K. Y. and J. Paslaski. Condition for short pulse generation in ultrahigh frequency mode-locking of semiconductor lasers. *Photonics Technology Letters, IEEE*, 3(11): 974–976, November 1991.
- [171] J. Palaski and K. Y. Lau. Parameter ranges for ultrahigh frequency mode locking of semiconductor lasers. *Applied Physics Letters*, 59(1):7–9, July 1991.
- [172] F. Kefelian, S. O’Donoghue, M. T. Todaro, J. G. McInerney, and G. Huyet. RF Linewidth in Monolithic Passively Mode-Locked Semiconductor Laser. *Photonics Technology Letters, IEEE*, 20(16):1405–1407, August 2008.
- [173] J. Javaloyes and S. Balle. Mode-Locking in Semiconductor Fabry-Perot Lasers. *IEEE Journal of Quantum Electronics*, 46(7):1023–1030, 2010.
- [174] URL <http://www.iue.tuwien.ac.at/phd/palankovski/node37.html>.
- [175] URL <http://www.ist-brighter.eu/tuto3/CONF03/CONF03.pdf>.
- [176] L. Arissian and J. C. Diels. Repetition rate spectroscopy of the dark line resonance in rubidium. *Optics Communications*, 264(1):169–173, 2006.
- [177] J. Vanier. Atomic clocks based on coherent population trapping: a review. *Applied Physics B: Lasers and Optics*, 81:421–442, 2005.
- [178] Benabid F. Hollow-core photonic bandgap fibre: new light guidance for new science and technology. *Philos Transact A Math Phys Eng Sci.*, 364:3439–62, 2006.
- [179] N. Belcher, E. E. Mikhailov, and I. Novikova. Atomic clocks and coherent population trapping: Experiments for undergraduate laboratories. *American Journal of Physics*, 77(11):988–998, 2009.
- [180] S. Knappe, J. Kitching, L. Hollberg, and R. Wynands. Temperature dependence of coherent population trapping resonances. *Applied Physics B: Lasers and Optics*, 74:217–222, 2002.
- [181] Deng J. L., Hu Z. F., He H. J., and Wang Y. Z. Temperature Dependence of Dark Lines in Coherent Population Trapping. *Chinese Physics Letters*, 23(7):1745, 2006.